Temporal Order of Interaction Directs Native Assembly of the Mammalian Signal Recognition Particle

Tuhin Subhra Maity

A dissertation submitted to the faculty of the University of North Carolina at Chapel Hill in partial fulfillment of the requirements for the degree of Doctor of Philosophy in the Department of Chemistry.

Chapel Hill
2007

Approved by,

Kevin M. Weeks

Linda L. Spremulli

Howard M. Fried

Marcey L. Waters

Gary J. Pielak

Abstract

Tuhin Subhra Maity

Temporal Order of Interaction Directs Native Assembly of the Mammalian Signal Recognition Particle
(Under the direction of Prof. Kevin M. Weeks)

Assembly of most ribonucleoproteins (RNPs) proceeds via multi-step structural reorganization in both protein and RNA components. To date, essentially all assembly models for RNP have tacitly assumed that structural interaction between any two given components during an RNP formation either facilitates later steps in the assembly or has no effect on continued assembly. In contrast to this implicit hypothesis, this work reveals that untimely interaction between components may, in fact, disrupt native formation of an RNP. In the assembly of the mammalian signal recognition particle (SRP), SRP54 interacts with the preformed SRP19-SRP RNA complex to form the native SRP ternary complex. In contrast, if SRP54 interacts with the RNA prior to formation of the native SRP19-SRP RNA complex, these three components interact to form an alternate ternary complex. In this complex, two extended loops in SRP19 cannot natively interact with the RNA. It has been shown that the premature RNA binding by SRP54 alters the SRP19-RNA assembly energy landscape in such a way that an alternate SRP19-RNA folding pathway leading to non-native complex formation becomes kinetically prevalent. In a different instance, it has been found that prior RNA binding by SRP68/72 negatively

affects assembly of SRP19 with the SRP RNA, and vice versa. Experimental results support a model in which *structural tension* between two similar but slightly distinct RNA structures induced by SRP19 and SRP68/72 binding is the origin of such anti-cooperativity. Overall, this work suggests that the order by which each constituent in an RNP interacts with others during assembly may have a decisive role in formation of the native complex. It has been inferred in this work that idiosyncratic assembly mechanisms, such as cellular compartmentalization and preferred early and late assembly phases, may play critical regulatory roles in preventing order-of-interaction driven misassembly for many multi-component RNPs in the cell.

“Extraordinary claims require extraordinary evidence.”

− Carl Sagan (1934-1996)

ACKNOWLEDGEMENT

I appreciate my family members back in *Kolkata* for their enormous trust on me. *Ma*, I know you were always worried that your younger son would be a high school dropout. I know how glad you must be seeing me writing my doctoral dissertation. *Baba*, you wanted me to get a university degree. I am certainly going to get one. To my brother and sister-in-law, thank you for being so supportive. To my nephew *Babu* and niece *Rona*, you have always been my *little*, but the most profound inspiration.

To Kevin Weeks, thank you for introducing me to the RNP world. The *timely interactions* always directed me to the next energy minimum in my graduate school landscape. To Howard Fried, thank you for your patience and support during all my unforeseeable visits to your office. To past and present members of the Weeks lab, it was a completely strange country to me. But, working in the lab was never felt like that. This would not have been possible without your camaraderie. To my friends in NC, the Saturday night *addas* were always followed by productive workweeks. Can't you guys move with me?

To my best friend and wife *Saswati*, you came halfway around the globe to this foreign land accompanying me, without knowing anyone else. You always stood by me in times of success and difficulty. I do not think I have words enough to acknowledge your support.

TABLE OF CONTENTS

LIST OF FIGURES

LIST OF ABBREVIATIONS

A	adenine/alanine
ATP	adenosine triphosphate
BABE	bromoacettamidobenzyl-EDTA
BSA	bovine serum albumin
C	cytosine/cysteine
CTP	cytidine triphosphate
°C	degree celsius
DNA	deoxyribonucleic acid
DTT	dithiotreitol
E	glutamine
EDTA	ethylenediaminetetraacetic acid
EtOH	ethanol
Fe	iron
$[Fe(II)(NH_4)_2]SO_4$	ferrous ammonium sulfate
G	guanosine/glycine
h	hour
HEPES	N-2-hydroxyethylpiperazine-N′-2-ethanesulfonic acid
HCl	hydrochloric acid
I_2	iodine
IPTG	Isopropyl β-D-1-thiogalactopyranoside
kDa	kilodalton
KOAc	potassium acetate

KOH	potassium hydroxide
L	leucine
l	liter
LS RNA	large subunit RNA
Mg^{2+}	magnesium ion
$MgCl_2$	magnesium chloride
mg	milligram
min	minute
μl	microliter
μM	micromolar
mm	millimolar
NaCl	sodium chloride
NaOH	sodium hydroxide
Ni^{2+}	nickel ion
NMR	nuclear magnetic resonance
nt	nucleotides
nM	nanomolar
NTP	nucleotide triphosphate
PAGE	polyacrylamide gel electrophoresis
PCR	polymerase chain reaction
PDB	protein dilution buffer
pmol	picomole
RNA	ribonucleic acid
rRNA	ribosomal RNA

S	serine
SDS	sodium dodecyl sulfate
SRP	signal recognition particle
T	thymidine
TBE	90 mM Tris-borate, 2 mM EDTA
TE	10 mM Tris (pH 7.5), 1 mM EDTA
Tris	tris(hydroxymethyl)aminomethane
tRNA	transfer RNA
U	uracil
UV	ultraviolet
V	volt
v	volume
vol	volume
W	watt/tryptophan
w	weight
Y	tyrosine

Chapter 1

Temporal Order of Interaction May Play a Decisive Role in Native Assembly of Ribonucleoproteins

1.1 Assembly of ribonucleoproteins

With the advancement of recent crystallographic, NMR and electron microscopic techniques, the structures of many ribonucleoprotein (RNP) complexes are now known. Unlike earlier days of RNP structure determination, this domain of knowledge is no longer restricted to simpler RNPs, but has been extended to extremely large, multi-component RNPs. For example, the crystal structure of the bacterial ribosome complexed with mRNA and tRNA has recently been solved at 2.8 Å resolution (*1*). Such high quality data provides an enormous amount of insights into the structural and functional details of the bacterial ribosome. In contrast, despite this wealth of information, very little can be known or inferred about the mechanism via which this complex is assembled in the cell. Understanding the molecular assembly mechanism of an RNP is of extreme importance because the final structure is dependent on the correct assembly of the complex. Misassembly leading to non-native structures may potentially lead to loss of function and eventually to serious cellular disorders.

Assembly of an RNP is a multi-dimensional problem. However, there are two major aspects that are associated with the biogenesis of any RNP. First, colocalization of components is necessary. In a eukaryotic cell this requires transport of protein or RNA components across the nuclear membrane. Second, assembly of most RNPs is more complex than a simple ‘lock and key’ docking mechanism. As a rule of thumb, at least one component undergoes structural changes during assembly of an RNP. In the next two sub-sections these aspects are discussed in detail.

1.1.1 Intra-cellular transports during biogenesis of RNPs

RNAs and proteins are synthesized in different compartments of a eukaryotic cell. DNAs are transcribed into RNAs in the nucleus; whereas, proteins are synthesized in the cytoplasm. Therefore, assembly of an RNP requires either protein or RNA components to transit through the nuclear membrane. For an RNP that functions in the cytoplasm, the simplest case would be transporting the RNA components into the cytoplasm to assemble with the proteins. Alternatively, for an RNP that functions in the nucleus, the simplest pathway would be transporting the protein components into the nucleus followed by assembly with the RNAs. However, multiple transport steps have been found to be associated with biogenesis of RNP complexes (*2, 3*). For example, the yeast ribosome functions in the cytoplasm. However, assembly of the yeast ribosome proceeds via multiple transport steps where some assembly components transit to the nucleolus (Figure 1.1) (*4*). All yeast ribosomal proteins are first imported to the nucleolus after being translated in the cytoplasm. In the nucleolus, they bind to the ribosomal RNAs to form the pre-ribosomal complex. Subsequently, the pre-ribosome undergoes various molecular reorganizations, and finally arrives at the cytoplasm as the functional ribosome. One reason for such nucleolar assembly steps is the presence of various trans-acting factors that are required for maturation of the yeast ribosome (see Figure 1.1).

However, there are other examples of multi-directional transport steps associated with RNP assembly where idiosyncratic assembly related movements of protein and RNA components are obscure. The assembly of the mammalian signal recognition particle (SRP) is such an example. Cellular biogenesis of the mammalian SRP consists of a nucleolar assembly step although the SRP functions in the cytoplasm (*5-7*). However, no nucleolar

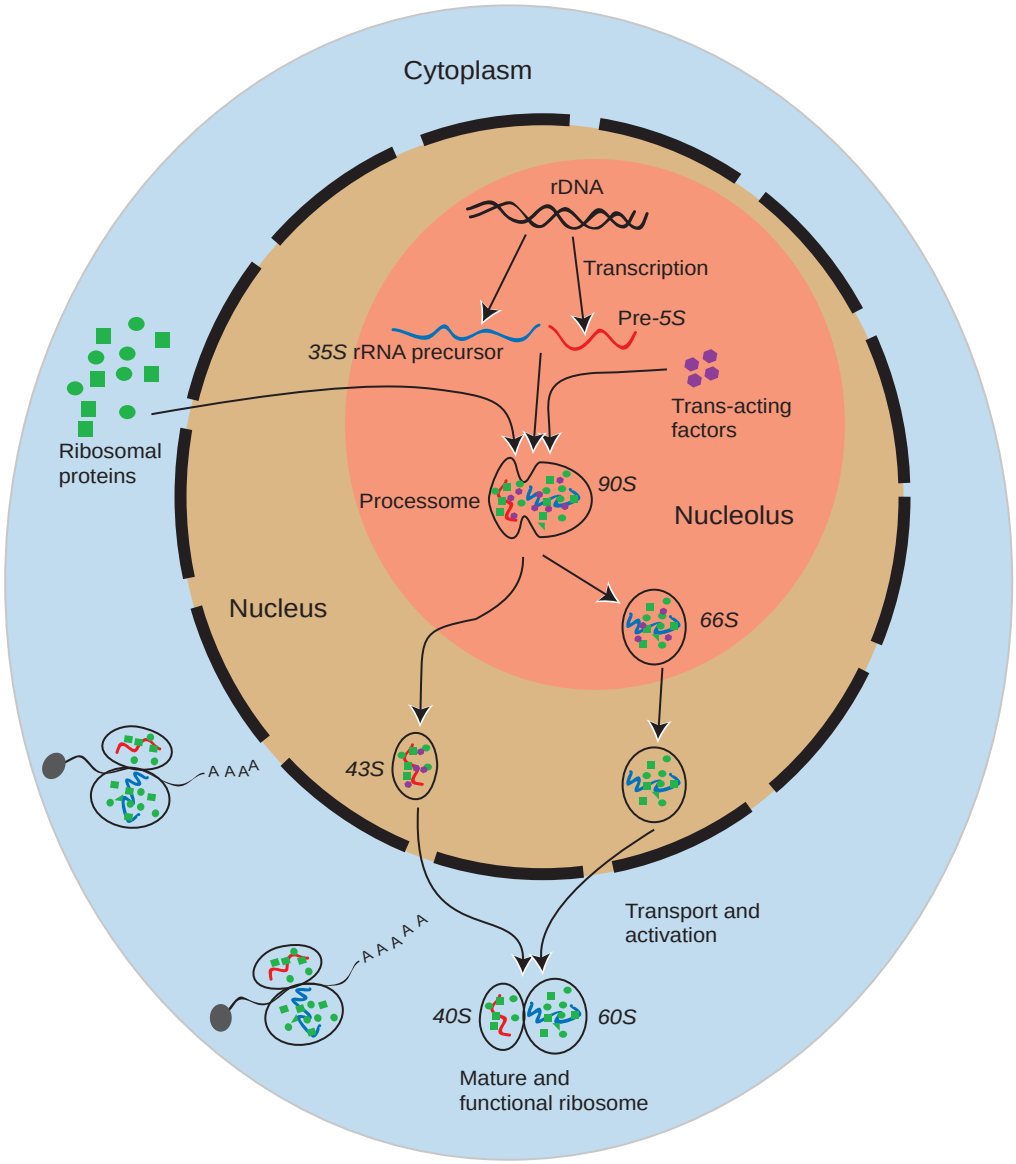

Figure 1.1. Multi-compartment biogenesis of the yeast ribosome *(4)*. First, ribosomal proteins are exported to the nucleolus. In the nucleolus, they bind to rRNAs to form the pre-ribosomal complex. The pre-ribosome matures into the functional ribosome as the complex transits from nucleolus to the cytoplasm. Numerous trans-acting factors participate at various stages during the maturation process.

cofactor has been found to date that is required for formation of the native SRP. Therefore, the purpose of the nucleolar assembly step in the SRP biogenesis is still unclear.

1.1.2 Structural reorganization during an RNP formation

It is more of a rule than an exception that formation of a protein-RNA complex is accompanied by structural changes in at least one participating component (*8*). In many cases, the structural changes are mutually induced between two components. In fact, during assembly of many multi-subunit RNPs, early structural changes have been found to facilitate later steps in the assembly.

Figure 1.2 illustrates an example for such a case during assembly of a hypothetical RNP complex comprised of three proteins and one RNA. The assembly starts with Protein A (green) binding to the RNA (yellow). Upon binding, both Protein A and the RNA undergo assembly-induced conformational changes – the *mutually induced fit* mechanism. The RNA-induced structural changes in Protein A now specifically facilitate the next step in the assembly process: interaction between Protein A and Protein B (orange). This interaction eventually leads to the assembly of Protein B with the RNA, followed by Protein B-induced RNA conformational changes. This structural reorganization in the RNA promotes subsequent RNA binding by Protein C (purple) to form the complete four-component RNP complex. This illustration is an example of a complex network of intermolecular interactions that, in effect, controls the hierarchical assembly of a multi-component RNP.

There are numerous real-life examples of assembly-induced conformational changes during formation of RNP complexes. Ribosomal protein S15 binds to 16S RNA at a three-way helical junction in the RNA (Figure 1.3A) (*8*). Before binding to the protein, the angles between the three helices are quite similar and approximately 120° (Figure 1.3A, left panel).

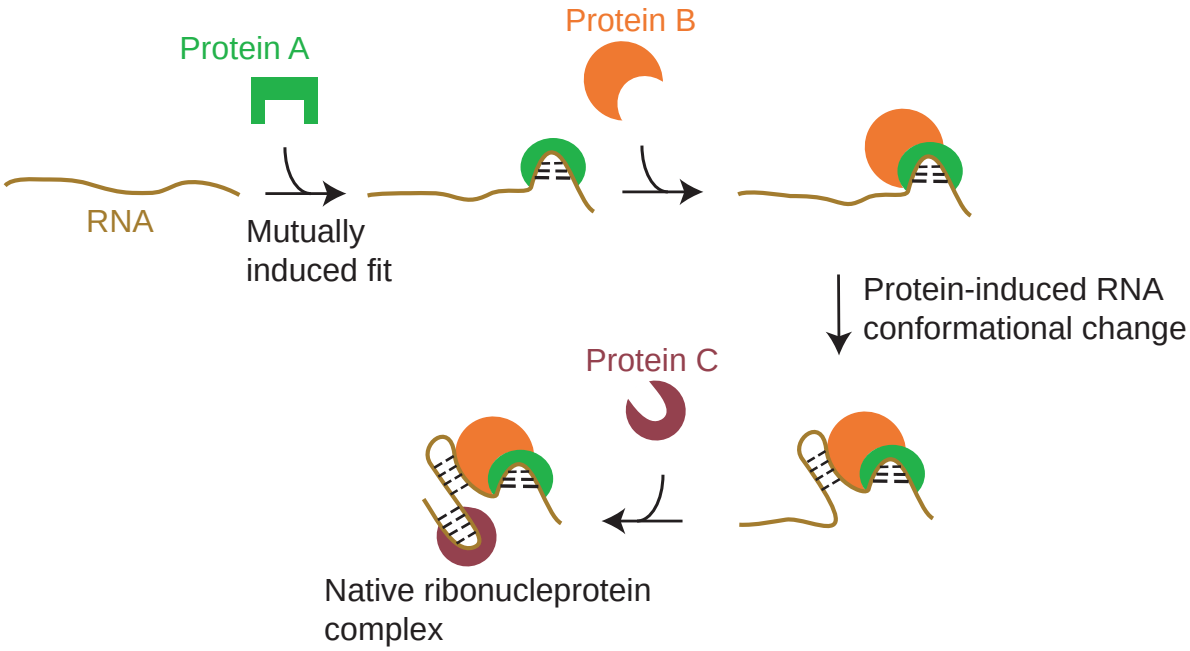

Figure 1.2. Induced conformational changes during assembly of a hypothetical four-component ribonucleoprotein complex.

Upon binding by the protein, two of the three helices coaxially stack with each other and the third one makes an acute angle with the main protein binding site (Figure 1.3A, right panel). S15 is a primary binding ribosomal protein and required for nucleating the assembly of the central domain of the bacterial small ribosomal subunit. Such protein-induced RNA structural changes may, thus, have a leading role in facilitating further assembly steps in the central domain of the ribosome. A classic example of the mutually induced fit mechanism is the formation of U1A-UTR complex (Figure 1.3B) (*8*). In this case, a C-terminal helix in the protein (U1A) undergoes a conformational change that allows intimate interaction between U1A and the RNA, and induces a structural reorganization in the RNA (compare the left and right panels in Figure 1.3B).

1.2 Misassembly during RNP formation

Efficient folding of many newly synthesized proteins does not occur spontaneously. Misfolding leading to aggregation is a common phenomenon that numerous large proteins have to overcome to retain their biological functions. Such aggregation is one of the leading causes for various serious human disorders such as Alzheimer's and Parkinson's diseases (*9*). Cofactors and molecular chaperones are often required to direct or, at least to facilitate, the native folding of several protein molecules. The bacterial chaperone GroEL is one such example. It recognizes unfolded or misfolded proteins and facilitates their native folding via a confinement mechanism (*10*).

Similarly, folding of almost all large RNAs, at least *in vitro*, is often slow and seldom complete. Stable kinetically trapped intermediates that are not obligatory structural scaffolds in the native folding pathway often accompany natively folded RNAs. For example, the *in*

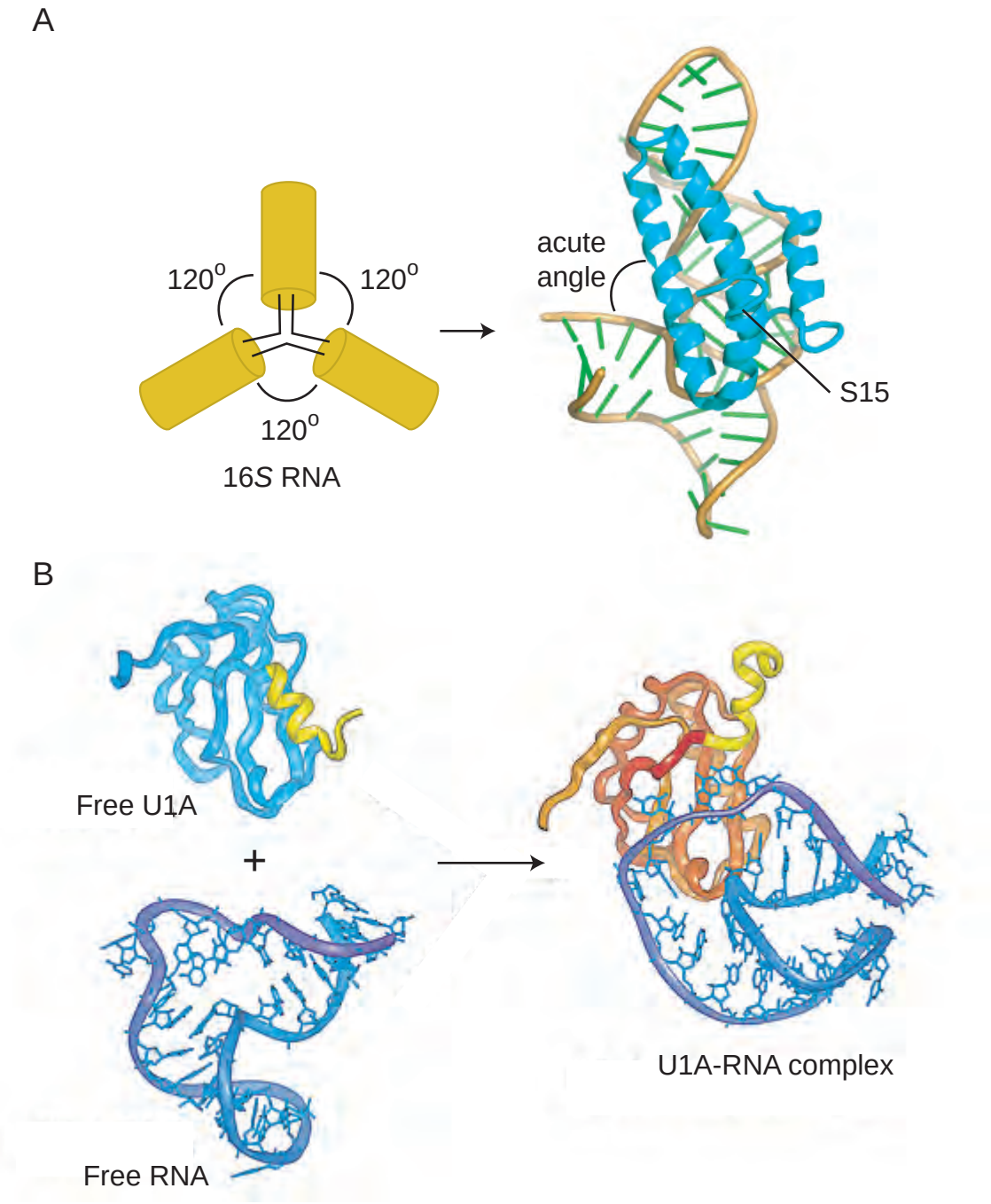

Figure 1.3. Assembly-induced conformational changes during RNP formation *(8)* (A) Protein binding-induced RNA conformational change. The angels between three RNA helices in 16S RNA before protein binding are approximately 120°. S15 binding causes coaxial stacking of two helices; whereas, the third helix makes an acute angle with the main protein binding site. (B) The *mutually induced fit* mechanism. Assembly of U1A protein with the UTR RNA induces conformational changes in both the protein and RNA components.

vitro self-splicing reaction of group I introns seldom proceeds to completion because of the presence of kinetically trapped alternate conformations (*11*). Several RNA chaperones and cofactors have been discovered that facilitate native/functional folding of many RNAs (*12*). UP1, a fragment derived from hnRNP A1 protein, can facilitate native folding of tRNAs and 5*S* RNA that are kinetically trapped in alternate conformations (*11*).

When an RNP complex forms, a new subset of interactions develops from inter-molecular contacts between the RNA and protein components (*13*). Such interactions may induce conformational changes in the RNA and protein components during the assembly of the RNP – the *induced fit* mechanism. Analogous to proteins and RNAs, RNPs may be misfolded or misassembled. Importantly, this may happen even if the assembly starts with a set of natively folded RNA and protein components. Cofactors and chaperones are, thus, expected to have a role in promoting native RNP formation. For example, *in vitro* reconstitution of the functional bacterial 30*S* ribosomal subunit from the protein and RNA components requires a heating step that rearranges the conformation of an intermediate that obligatorily forms during the assembly (Figure 1.4A) (*14*). However, it has been found that the DnaK chaperone system may circumvent the requirement for the heating step (Figure 1.4B) (*15*). Additionally, recent experiments have shown that DExH/D box proteins can also perform ATP-dependent remodeling of RNP complexes (*16*).

1.3 Native assembly of an RNP may require a preferred temporal order of interaction among the protein and RNA components

The phenomenon of RNP misfolding/misassembly is quite different from that of protein and RNA misfolding. Intercomponent interactions play a crucial role in directing

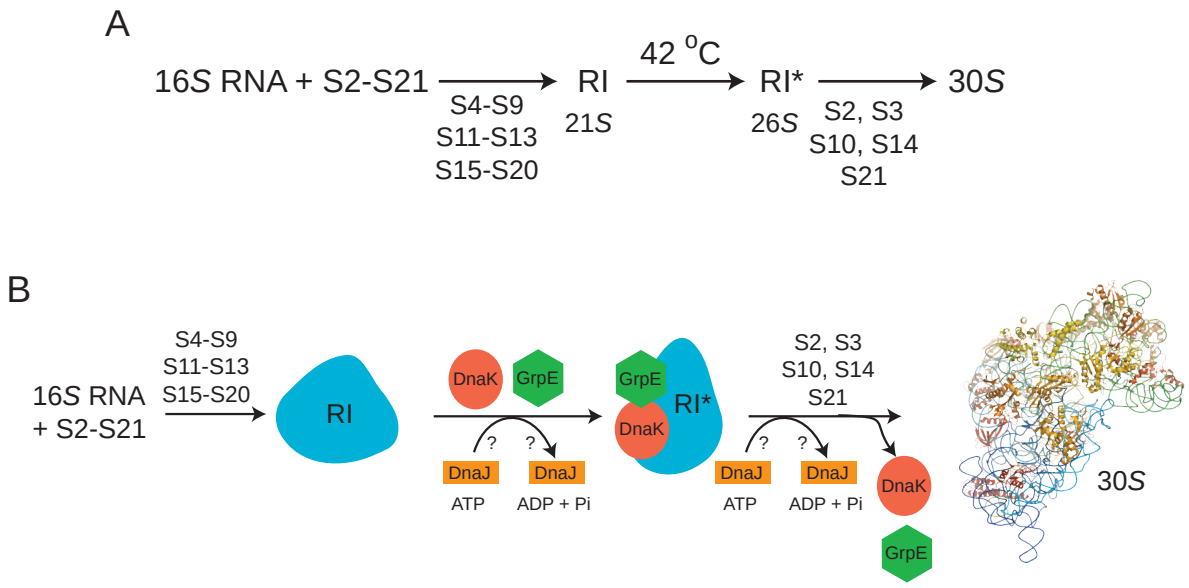

Figure 1.4. Chaperone assisted remodeling of a RNP complex. (A) A heating step is required for maturation of an intermiate complex (RI to RI*) that forms during *in vitro* reconstitution of 30S ribosomal subunit *(14)*. (B) The DnaK chaperone system circumvents the requirement for heating *(15)*.

assembly and folding of an RNP. As illustrated in Figure 1.2, assembly and folding of many RNPs occur in hierarchical fashion. Conformational rearrangements associated with binding of two specific components lead to binding by a third component and so on. This indicates that multi-component RNP formation may be required to follow a temporal order where each component binds only at the right time during the assembly. Therefore, it is not quite unreasonable to infer that any deviation from that preferred temporal order of binding/interaction may lead to formation of misassembled, non-functional RNPs. Apart from cofactors and chaperones, there are other regulatory mechanisms that cells use to facilitate native assembly of many RNPs.

Co-transcriptional assembly is one of the mechanisms that cells use to regulate biogenesis of many RNPs. In this case, the assembly events take place in the direction identical to that of the transcription process: from the 5'-end to the 3'-end along the RNA. In other words, the 5'-end of the RNA folds and assembles with the cognate proteins prior to the 3'-end. Such implicit control over folding and binding events during RNP formation may help the assembly mechanism bypass any kinetic traps that exist in the assembly energy landscape. For example, formation of the pre-mRNP complex in the cell is thought to occur co-transcriptionally (*17*). It has been hypothesized that the co-transcriptional nature of the assembly process plays a critical role in facilitating the correct splicing and export of mRNAs (*18*).

Another possible way to control the directionality of an RNP assembly is achieving a perfect balance in timing for each individual step. In this case, each participating component assembles only at the right time with the right rate. Distinct kinetic behaviors among the *E. coli* small subunit ribosomal proteins have been known for a long time. The ribosomal

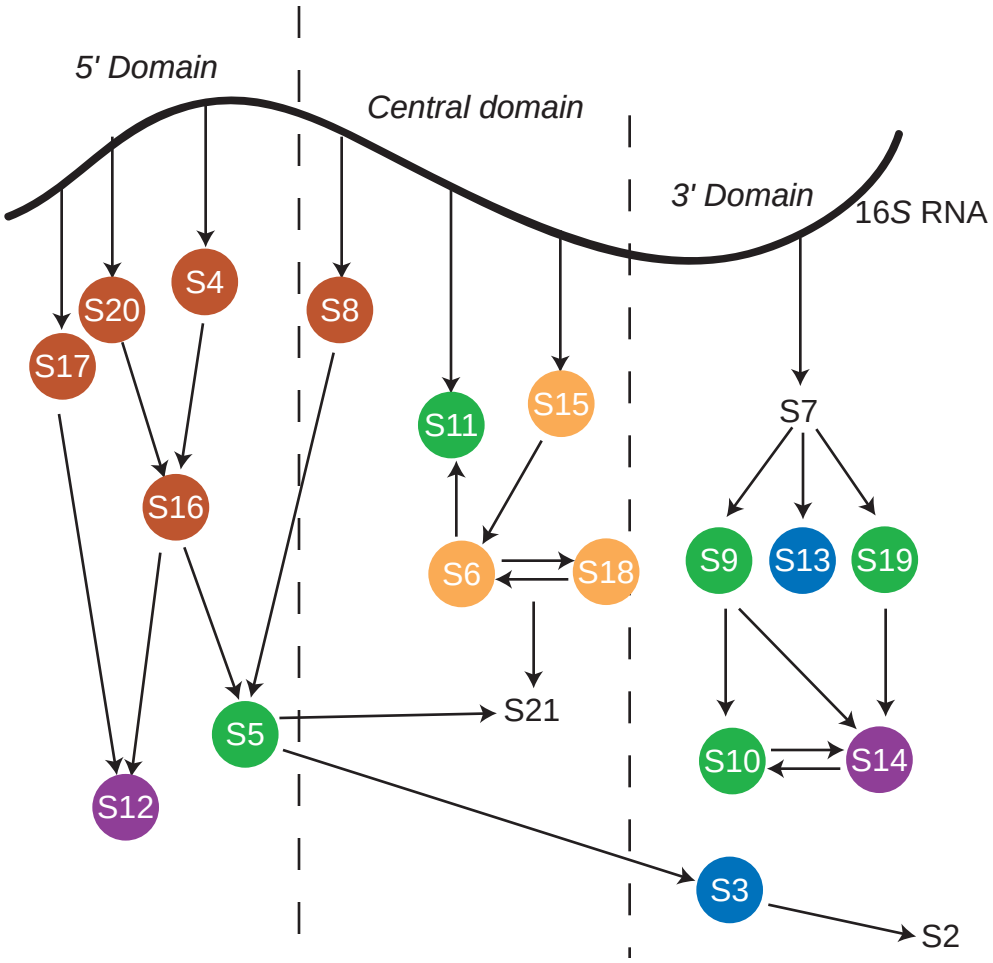

Figure 1.5. Assembly map for the *E.coli* 30*S* ribosomal subunit *(19)*. 16*S* RNA is shown as black line. The ribosomal proteins are colored according to their RNA binding rates. Red, 20-30 min^{-1}; orange, 8.1-15 min^{-1}; green, 1.2-2.2 min^{-1}; blue, 0.38-0.73 min^{-1}; purple, 0.18-0.26 min^{-1}.

proteins that associate with the 5'-domain of 16S RNA are found to bind the RNA about three orders of magnitude faster than those that associate with the 3'-domain of the RNA (Figure 1.5) (*19*). So, if all small subunit ribosomal proteins are added simultaneously to 16S RNA, the 5'-domain binding proteins will assemble with the RNA prior to the 3'-domain binding proteins due to their faster RNA-binding rate. Such distinctive kinetic behavior among the small subunit ribosomal proteins provides an implicit control over the temporal order of interaction/binding during assembly of the 30S ribosomal subunit. However, it is yet to be critically evaluated whether such an intrinsically preferred order has any role in avoiding incorrect formation of the complex.

1.4 Cellular compartmentalization and RNP assembly

An unexplored way to achieve the correct temporal order of binding during RNP formation is sub-cellular compartmentalization of assembly constituents. Referring back to the hypothetical four-component RNP system illustrated in Figure 1.2, it might be possible that any interaction between Protein B and the RNA prior to Protein A binding to the RNA disrupts the native assembly of the complex and results in an alternate conformation in the RNP. For a kinetically auto-regulated assembly, RNA binding by Protein A would be significantly faster than that by Protein B. In this case, practically no Protein B interacts with the RNA prior to Protein A. In the absence of such kinetic control, an alternate solution is sequestering Protein B in a distinct cellular compartment until formation of the Protein A-RNA complex is complete. However, no experimental data is present to date to support the hypothesis that cellular compartmentalization may play a critical role in directing native assembly of RNP complexes.

1.5 The present study

The observed temporal order of interaction in biogenesis of RNPs has primarily been viewed as an inherent idiosyncratic behavior of the assembly process. However, as described above, this phenomenon can, in principle, play a regulatory role in RNP biogenesis. Cellular multi-compartment assemblies of many RNPs have only been evaluated from the perspective of distinctive localization of trans-acting factors, but not from the perspective of a control mechanism that ensures correct temporal order of interaction among the components during assembly.

In this study, the mammalian signal recognition particle (SRP) was used as a model system to test above hypothesis that the chronology of intermolecular interactions plays a crucial role in formation of the native SRP complex. In Chapter 2, the structures of the SRP ternary complexes formed by adding SRP19 and SRP54 to the SRP RNA in different chronological orders are evaluated and compared using biochemical techniques. Surprisingly, it was found that the native folding of SRP19 is critically dependent on the timing of SRP54-RNA interaction. If SRP54 interacts with the RNA prior to formation of the native SRP19-RNA complex, SRP19 cannot fold to its native structure – two RNA binding loops in SRP19 become misfolded. In Chapter 3, detailed molecular mechanisms for the order-of-interaction driven native and non-native SRP54-SRP19-RNA ternary complex formations are described. It is shown that a three-fold interface formed by SRP19, SRP54 and the SRP RNA gates native formation of the SRP ternary complex. In Chapter 4, RNA binding properties of SRP68/72 are evaluated. Experimental results support a model where binding by SRP19 and SRP68/72 proteins induce two slightly different SRP RNA conformations. Such preferences

for slightly different RNA structures may explain the observed anti-cooperativity of SRP19 and SRP68/72 in RNA binding.

The outcomes of this study not only improve our understanding of the assembly of mammalian SRP, but also provide some unexplored insights into assembly of many RNPs in general.

1.6 References

1. Selmer, M., Dunham, C. M., Murphy, F. V., Weixlbaumer, A., Petry, S., Kelley, A. C., Weir, J. R., and Ramakrishnan, V. (2006) Structure of the 70S ribosome complexed with mRNA and tRNA. *Science 313*, 1935-42.

2. Pederson, T., and Politz, J. C. (2000) The nucleolus and the four ribonucleoproteins of translation. *J. Cell Biol. 148*, 1091-1095.

3. Filipowicz, W., and Pogacic, V. (2002) Biogenesis of small nucleolar ribonucleoproteins. *Curr. Opin. Cell Biol. 14*, 319-327.

4. Fromont-Racine, M., Senger, B., Saveanu, C., and Fasiolo, F. (2003) Ribosome assembly in eukaryotes. *Gene 313*, 17-42.

5. Jacobson, M. R., and Pederson, T. (1998) Localization of signal recognition particle RNA in the nucleolus of mammalian cells. *Proc. Natl. Acad. Sci. USA 95*, 7981-7986.

6. Politz, J. C., Yarovoi, S., Kilroy, S. M., Gowda, K., Zwieb, C., and Pederson, T. (2000) Signal recognition particle components in the nucleolus. *Proc. Natl. Acad. Sci. USA 97*, 55-60.

7. Alavian, C. N., Politz, J. C. R., Lewandowski, L. B., Powers, C. M., and Pederson, T. (2004) Nuclear export of signal recognition particle RNA in mammalian cells. *Biochem. Biophys. Res. Commun. 313*, 351-355.

8. Williamson, J. R. (2000) Induced fit in RNA-protein recognition. *Nat. Struct. Biol. 10*, 834-837.

9. Selkoe, D. J. (2003) Folding proteins in fatal ways. *Nature 426*, 900-904.

10. Frydman, J., Nimmesgern, E., Ohtsuka, K., and Hartl, F. U. (1994) Folding of nascent polypeptide chains in a high molecular mass assembly with molecular chaperones. *Nature 370*, 111-117.

11. Herschlag, D. (1995) RNA chaperones and the RNA folding problem. *J. Biol. Chem. 270*, 20871-20874.

12. Weeks, K. M. (1997) Protein-facilitated RNA folding. *Curr. Opin. Struct. Biol. 7*, 336-342.

13. Draper, D. E. (1995) Protein-RNA recognition. *Annu. Rev. Biochem. 64*, 593-620.

14. Traub, P., and Nomura, M. (1968) Structure and function of E. coli ribosomes, V. Reconstitution of functionally active 30S ribosomal particles from RNA and proteins. *Proc. Natl. Acad. Sci. USA 59*, 777-784.

15. Maki, J. A., Schnobrich, D. J., and Culver, G. M. (2002) The DnaK chaperone system facilitates 30*S* ribosomal subunit assembly. *Mol. Cell 10*, 129-138.

16. Jankowsky, E., and Bowers, H. (2006) Remodeling of ribonucleoprotein complexes with DExH/D RNA helicases. *Nucleic Acids Res. 34*, 4181–4188.

17. Daneholt, B. (2001) Assembly and transport of a premessenger RNP particle. *Proc. Natl. Acad. Sci. USA 98*, 7012-7017.

18. Aguilera, A. (2005) Cotranscriptional mRNP assembly: from the DNA to the nuclear pore. *Curr. Opin. Cell Biol. 17*, 242-250.

19. Talkington, M. W., Siuzdak, G., and Williamson, J. R. (2005) An assembly landscape for the 30S ribosomal subunit. *Nature 438*, 628-632.

Chapter 2

Compartmentalization Directs Assembly of the Mammalian Signal Recognition Particle

2.1 The signal recognition particle (SRP)

2.1.1 Function of the SRP

Cells are divided into multiple compartments each filled with some unique sets of proteins that have distinct structural and functional roles. However, all proteins are made in the cytoplasm by the ribosomes. Cells, thus, have evolved molecular machineries that carry out the delivery of a specific class of proteins to a specific location in the cell. The signal recognition particle (SRP) and its receptor (SR) are responsible for targeting nascent membrane or secretory proteins and delivering them to the endoplasmic reticulum in eukaryotes or to the plasma membrane in prokaryotes (*1-3*). Both the SRP and the SR are conserved in all forms of life (*4*). Protein targeting by the SRP is a combination of multiple synchronized steps (Figure 2.1). First, the SRP recognizes the N-terminal signal sequence of a nascent membrane or secretory protein emerging from a translating ribosome. A typical signal sequence is a stretch of 9-12 consecutive large hydrophobic amino acids that may or may not be a permanent part of the targeted protein (*5*). In eukaryotes, upon signal sequence recognition the SRP blocks the elongation factor (eEF2) binding site in the ribosome (*6*). This causes a halt in the translation elongation process. The SRP then directs the ribosome-nascent chain complex to the endoplasmic reticulum or to the plasma membrane where the SRP interacts with the SR. Both the SRP and the SR have a homologous GTPase domain (*7*). Upon interacting, they undergo GTP hydrolysis. GTP hydrolysis is the key that coordinates the delivery of the ribosome-nascent chain complex to the translocon and the dissociation of the SRP from the SR. At this point, the ribosome resumes its elongation activity and the targeted protein is eventually dispatched to its subsequent destination.

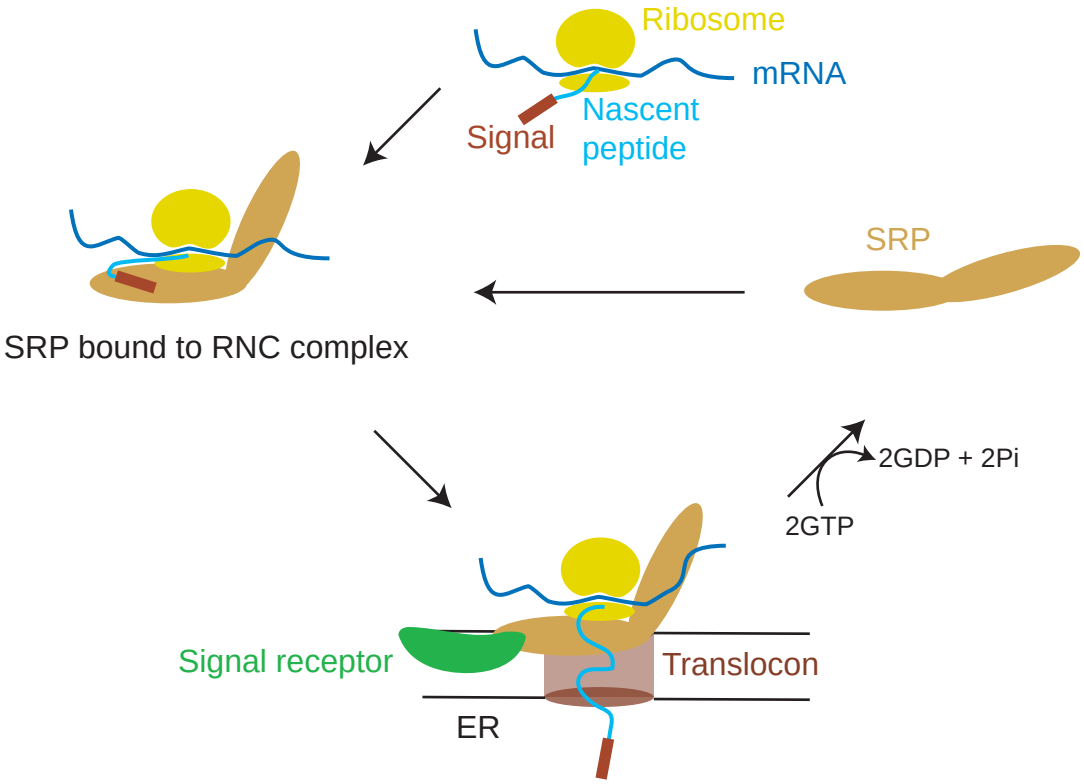

Figure 2.1. Protein targeting by the SRP. The SRP recognizes the N-terminal signal of a nascent membrane or secretory protein emerging from a translating ribosome. The SRP then brings the ribosome-nascent chain (RNC) complex to the endoplasmic reticulum (ER), where the SRP interacts with the signal receptor (SR). GTP hydrolysis is the key that releases the SRP from both the ribosome and the SR.

2.1.2 Architecture of the SRP

The SRP components are phylogenetically well conserved. Metazoan SRPs consist of six proteins (SRP19, SRP54, SRP68, SRP72, SRP9 and SRP14) and a ~ 300 nt RNA (SRP RNA) (Figure 2.2) (*1*-*3*). The SRP can be divided into two functionally and structurally independent domains (*6*, *8*). About half of the RNA and SRP19, SRP54, SRP68/72 heterodimer form the S-domain; whereas, the second half of the RNA and SRP9/14 heterodimer form the *Alu* domain. The *Alu* domain performs the elongation arrest activity of the SRP. On the other hand, the S-domain performs three universally conserved roles of the SRP: signal sequence recognition, GTP hydrolysis and interaction with the SR. All of these three functions are carried out by SRP54, the universally conserved SRP protein (*1*). SRP19 anchors two helices in the RNA that provides structural stability to the RNA – a prerequisite for SRP54 binding to the RNA (*9*-*13*). It is speculated that SRP68/72 facilitate the hinge movement between the two SRP subunits that coordinates the signal peptide recognition activity by the large subunit and the elongation arrest activity by the *Alu* subunit (*6*).

Likewise, the yeast SRP consists of a ~500 nt RNA (scR1) and six proteins (Srp72p, Srp68p, Srp54p, Sec65p, Srp21, and Srp14p) (*14*, *15*). All of these proteins are homologous to those of their vertebrate counterparts except that Srp21, which is yeast specific. Also, the yeast SRP does not have any protein homologous to SRP9.

The bacterial SRP is the simplest one. It is comprised of a ~ 110 nt RNA (4.5S RNA) and a homologue of SRP54 (*ffh*) (*16*). Importantly, the bacterial SRP does not posses the *Alu* domain. Thus, the bacterial SRP lacks the elongation arrest activity during protein targeting.

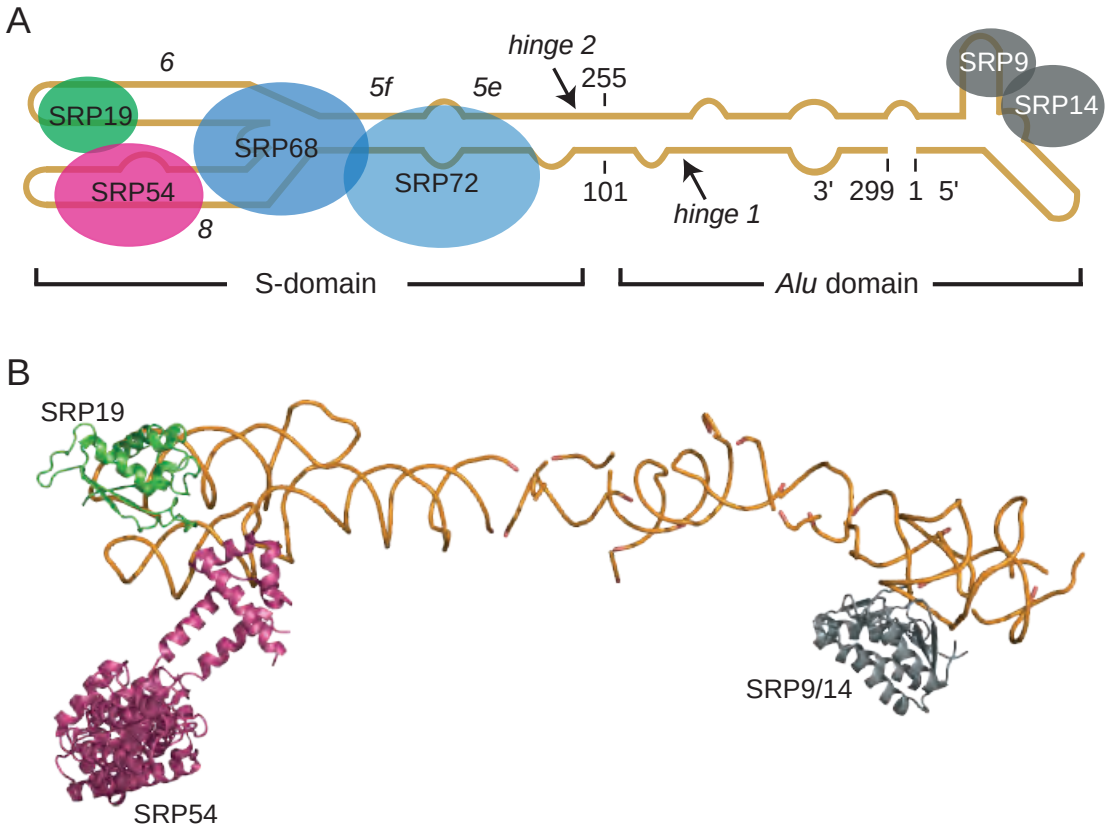

Figure 2.2. The mammalian SRP. (A) The mammalian SRP is comprised of a 300 nt RNA and six proteins. Proteins are shown as colored ovals; the RNA is represented as yellow line. Two SRP domains can assemble and function independent of each other. (B) Structure of the mammalian SRP derived by superimposing previously determined crystal structures of SRP components on the cryo-EM map of the SRP *(8)*. SRP68/72 are not shown due to lack of high resolution data.

2.1.3 Cellular biogenesis of the SRP

Although the SRP functions in the cytoplasm, experiments performed with both yeast (*17, 18*) and mammalian (*19-21*) cells support a model in which some SRP components transit initially through the nucleus and, perhaps, specifically through the nucleolus. For example, endogenous mammalian SRP RNA is readily detectable by in situ hybridization in the nucleolus of rat fibroblast cells. When exogenous SRP RNA is microinjected into the nuclei of these cells, it initially localizes in the nucleolus and subsequently appears in the cytoplasm (*19, 20*). Similarly, green fluorescent protein (GFP) fusions of SRP19, SRP68 and SRP72 are found in both nuclear and cytoplasmic compartments of mammalian cells (*20*). In contrast, both GFP-tagged and endogenous SRP54 are localized almost exclusively in the cytoplasm of mammalian cells. Comparable results are also obtained in yeast (*17, 18*). Five of the six yeast SRP proteins (Srp65p, Srp68p, Srp72p, Srp21 and Srp14p) and the yeast SRP RNA (scR1) are readily visualized in both the nucleolus and cytoplasm. In contrast, like its mammalian homologue, Srp54p is not detectable in the nucleus.

These experiments are consistent with a model (Figure 2.3) in which all SRP proteins, except SRP54, are imported to the nucleolus where they assemble with the SRP RNA. The partially assembled SRP is then exported back to the cytoplasm to assemble with SRP54 and form the SRP holocomplex. This ‘SRP54-late’ binding model is also consonant with biochemical studies showing that SRP54 does not bind tightly to the free SRP RNA and requires prior formation of the SRP19-RNA complex (*22*). Initial binding by SRP19 induces significant conformational changes in the SRP RNA and stabilizes an RNA structure specifically recognized by SRP54 (*10, 12*).

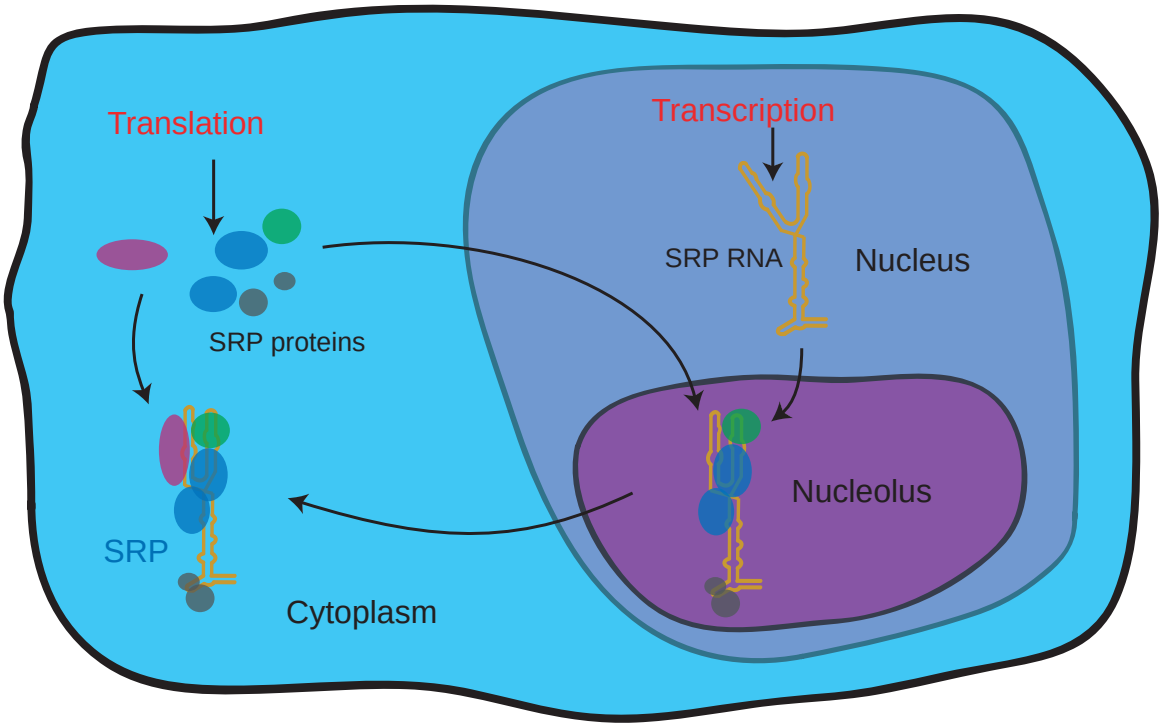

Figure 2.3. The cellular 'SRP54-late' assembly pathway. All SRP proteins, except SRP54 (purple), are imported to the nucleolus to bind the SRP RNA. SRP54 binds the partially formed SRP complex in the cytoplasm.

2.2 Evaluating the role of compartmentalization during SRP biogenesis

So far, the role of cellular compartmentalization during SRP biogenesis is completely unknown. SRP54 is the only protein that remains sequestered in the cytoplasm during the temporal interval while other SRP proteins assemble with the SRP RNA in the nucleolus. In order to evaluate the requirement for compartmentalization during SRP assembly, a three-component ribonucleoprotein comprised of SRP54, SRP19 and the S-domain part of the SRP RNA (LS RNA) was studied. First, the cooperativity between SRP19 and SRP54 in RNA binding was evaluated using phosphorothioate footprinting experiments. Next, cellular compartmentalized assembly was modeled *in vitro* as formation of SRP19-RNA complex followed by SRP54 binding to that complex. The hypothetical non-compartmentalized assembly was modeled as reverse addition of proteins to the RNA: SRP54 followed by SRP19. The structural consequence for the cellular compartmentalization was addressed by comparing structures of the ternary complexes formed via the two pathways mentioned above. Despite the fact that SRP54 does not stably associate with the free RNA, it has been found that the presence of SRP54 during assembly of SRP19 with the RNA adversely affects the assembly-induced folding of SRP19. If SRP54 binds the RNA while the SRP19-RNA complex is still forming, two RNA binding loops in SRP19 cannot fold to their native conformations. This requirement for absence of SRP54 during assembly of SRP19 with the RNA suggests that cellular compartmentalization has a critical role in directing native assembly of the SRP.

2.3 Materials and methods

2.3.1 Proteins, RNA, reaction conditions, and structure visualization

Native SRP19 (*10*) and SRP54 (*23*) were expressed and purified as described, except that SRP54 was purified by Ni^{2+}-agarose and Biorex columns. The final dialysis buffers contained 50% (v/v) glycerol. LS RNA (nts 101-255 of the human sequence) was transcribed from plasmid *phR* (*24*) and purified by denaturing gel electrophoresis. RNA was refolded by heating at 95 °C (1 min), incubating at 60 °C (10 min) in the presence of RNA refolding buffer [300 mM potassium acetate (pH 7.6), 5 mM $MgCl_2$, 20 mM Hepes (pH 7.6), 0.01% (v/v) Triton], followed by slow cooling to room temperature (~ 40 min). All protein binding reactions were performed at 25 °C in RNA refolding buffer supplemented with 1/5 vol of 300 mM NaCl, 50 mM sodium phosphate (pH 8.0) and 0.5 mg/ml BSA. SRP complexes were visualized using PyMOL (www.pymol.org).

2.3.2 Equilibrium binding measurements

These experiments were performed by Marsha A. Rose. 5′-[^{32}P]-end labeled guanosine phosphorothioate substituted LS RNA (0.3-0.5 nM) was incubated with SRP19, SRP54, or both at 25 °C in 20 μL. Bovine serum albumin (0.1 mg/mL, New England Biolab) was present in the solution to prevent non-specific protein binding. Complexes were incubated for 30 min and cleavage was initiated by adding 1/10 vol of 7 mM I_2. Reactions were quenched after 10 sec by addition of 1/10 vol of 70 mM 2-mercaptoethanol and an equal vol of formamide stop dye. For measurements of SRP19-facilitated binding by SRP54, the SRP19 concentration was 15 nM and was added 15 min prior to addition of SRP54. Reaction products were resolved by denaturing electrophoresis and band intensities (*I*) were quantified by phosphorimaging (Molecular Dynamics). Data were fit to $I/I_0 = K_d/(K_d +$

[SRP19]) + b, where K_d is the equilibrium dissociation constant and b is the cleavage intensity at saturating protein concentration.

2.3.3 Phosphorothioate footprinting analysis of native and non-compartmentalized complexes

These experiments were performed by Chris L. Leonard. All reactions (10 μL, 25 °C) contained identical buffer components (RNA refolding buffer supplemented with 1/5 vol of 50 mM sodium phosphate (ph 8.0) and 300 mM NaCl) and protein and RNA concentrations; final concentrations of SRP19, SRP54 and the LS RNA were 50 nM, 100 nM and 10 nM, respectively. Assembly of the ternary complexes was performed by ordered addition of each protein to the RNA (SRP19 first or SRP54 first) followed by a 20 min incubation period. Iodine cleavage products were resolved in a series of 8-20% (w/v) denaturing gels. Lane integration was performed by phosphorimaging.

2.3.4 Expression, purification and Fe(II)-BABE derivatization of SRP19 variants

Four existing cysteines in the native sequence (C4S, C17V, C53V and C94Y) were mutated to residues found in SRP19 proteins from other species using oligonucleotide directed mutagenesis (Quickchange® multi site-directed mutagenesis kit, Stratagene). This ΔCys parent construct was used to introduce unique cysteine residues at solvent accessible positions (E31C, W72C, L93C or L106C). SRP19 protein variants were expressed in *E. coli* strain BL21-CodonPlus(DE3)-RIL (Stratagene) and purified as described (*10*). To conjugate SRP19 with Fe(II)-BABE (Pierce), 20 μl of each SRP19 variant protein (~20 μM) was treated with an equal vol of 8.5 mM Fe(II)-BABE [in 900 mM NaCl, 50 sodium phosphate (pH 8.0); 37 °C for 45 min]. Unreacted Fe(II)-BABE was removed by dialysis against 1 L of 900 mM NaCl, 50 mM sodium phosphate (pH 8.0), 10 mM 2-mercaptoethanol and 25% (v/v)

glycerol. As a control, the ΔCys parent protein was mock treated with Fe(II)-BABE (Pierce) in parallel with the single cysteine mutants. Equilibrium dissociation constants for all SRP19 proteins were measured by filter partitioning (*10*) using 0.1 nM [^{32}P]-internally labeled LS RNA. Dissociation constants were (K_d, in nM; values for the Fe(II)-BABE derivatized protein are given in parentheses, errors are ±40% or less): wild type, 2.0; ΔCys, 1.0; 31Cys, 15 (8); 72Cys, 6.0 (1.0); 93Cys, 10 (10); 106Cys, 10 (9.0). The dialyzed protein could be stored at -20 °C for at least 7 days without loss of RNA binding or cleavage activity.

2.3.5 Site-directed cleavage experiments

Reactions (10 μL) contained 250 nM of each of SRP19, SRP54, and refolded 5′-[^{32}P]-end labeled LS RNA components, if present, in RNA refolding buffer supplemented with 1/5 vol of 50 mM sodium phosphate (ph 8.0) and 300 mM NaCl. Cleavage (3 min) was induced by addition of ascorbic acid and hydrogen peroxide to final concentrations of 10 mM and 0.3% (v/v), respectively and quenched by addition of 10 μl of a 1:4 1 M thiourea:formamide solution containing 1% SDS. Cleaved RNA fragments were resolved in 10% denaturing polyacrylamide gels. Individual band intensities were integrated using SAFA (*25*) and site-specific cleavages were quantified by subtracting the background obtained for the ΔCys construct from cleavage intensity measured for the Fe(II)-BABE conjugated SRP19 variants. For kinetic stability measurements, integrated bands intensities were normalized at positions 148 and 198.

2.4 Results

2.4.1 Cooperative RNA binding by SRP19 and SRP54

Marsha A. Rose determined the affinities of SRP protein-RNA complexes by phosphorothioate footprinting. All experiments were performed with an RNA spanning the SRP large subunit (termed LS RNA, nts 101-255, Figure 2.2A). The LS RNA, SRP19 and SRP54 assemble independently of other SRP components. Equilibrium protein dissociation constants (K_d) were monitored using an LS RNA carrying phosphorothioate substitutions at guanosine residues. For the free LS RNA, all phosphorothioate linkages were readily cleaved upon the addition of iodine (see 0 nM SRP19 lane, Figure 2.4A). Upon addition of SRP19, specific RNA positions became protected from cleavage (see G150, G152 and G197-198; Figure 2.4A). The equilibrium dissociation constant (K_d) for the SRP19-RNA complex was obtained by fitting the iodine-dependent cleavage intensity as a function of protein concentration to an equation for formation of a bimolecular complex. SRP19 binds the RNA with a Kd of 1.5 nM (Figure 2.4B), which agrees with previous values (2 nM) determined by conventional methods (*10*, *26*).

Similarly, phosphorothioate footprinting experiments were used to monitor binding of SRP54 to the free LS RNA (upper panel, Figure 2.5A). SRP54 binding was undetectable at protein concentrations up to 500 nM (open symbols, Figures 2.5A,B). In contrast, when SRP54 bound to the pre-formed SRP19-RNA complex, specific phosphorothioate-substituted guanosine nucleotides became additionally protected from cleavage (lower panel, Figure 2.5B). SRP54 bound to the pre-organized SRP19-RNA complex with an equilibrium K_d of 12 nM (solid symbols, Figure 2.5B).

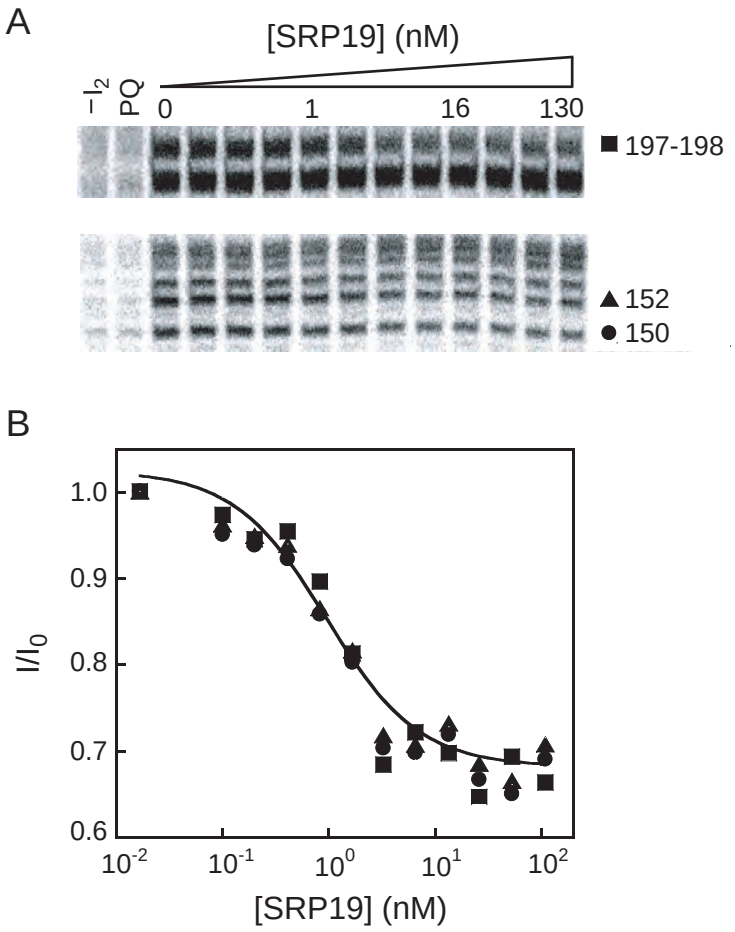

Figure 2.4. Equilibrium RNA binding by SRP19 using phosphorothioate footprinting. (A) Affinity of SRP19 for the RNA is measured by monitoring SRP19 binding-induced protections from iodine mediated cleavage at the phosphorothioate substituted positions in the RNA. (B) Quantitative analysis of SRP19 binding. Fraction of protection is plotted against SRP19 concentration.

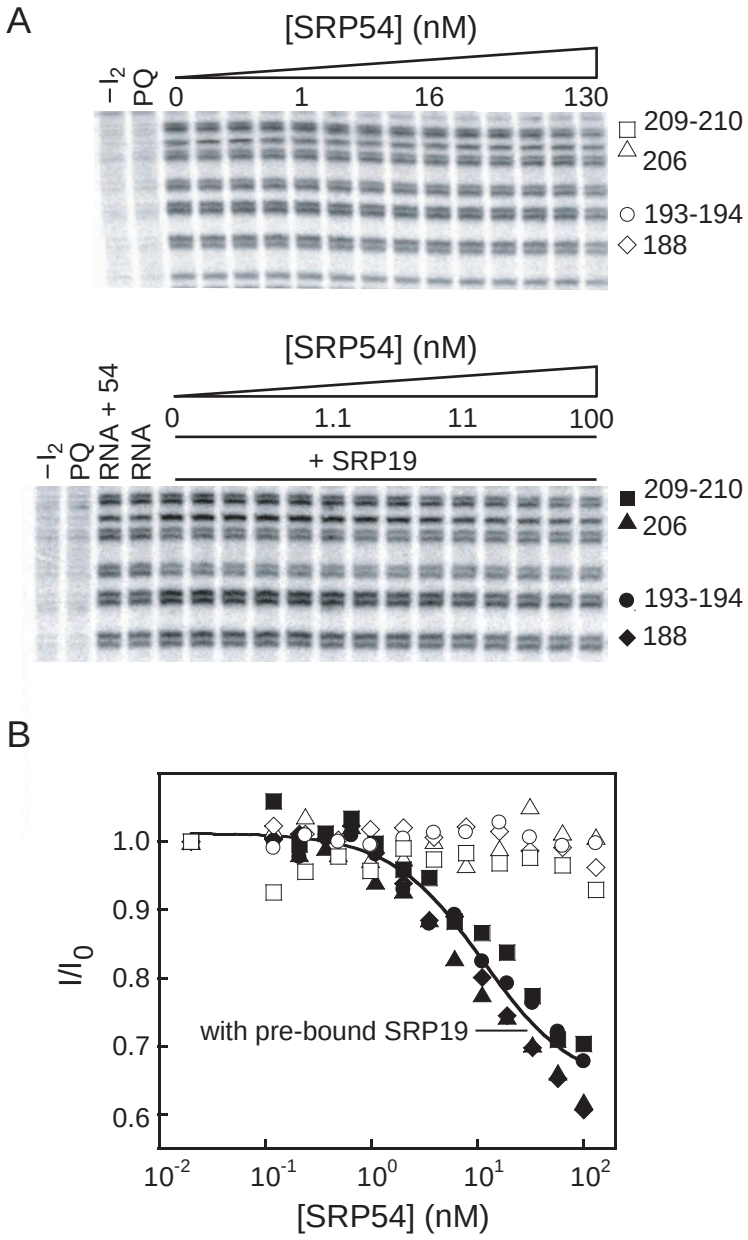

Figure 2.5. RNA binding by SRP54 requires prebinding by SRP19 (A) Affinitiy of SRP54 for the free RNA (top) and for the preformed SRP19-RNA (bottom) complex were determined by monitoring SRP54 binding-induced protections from iodine mediated cleavage at the phosphorothioate substituted positions in the RNA. (B) Quantitative analysis of SRP54 binding to the free RNA (open symbols) and to the preformed SRP19-RNA complex (solid symbols).

In summary, SRP54 does not form a stable complex with the SRP RNA at concentrations as high as 500 nM while prior binding by SRP19 enhances SRP54 binding affinity by at least 40-fold.

2.4.2 Strategy for evaluating role of compartmentalization in SRP assembly

In the cell, SRP54 appears to interact with the SRP RNA in the cytoplasm and only after the RNA has formed a complex with SRP19 (*17-20, 27*): the 'SRP54-late' assembly model. In this work, order-of-addition experiments were used to evaluate whether allowing SRP19 and SRP54 to assemble simultaneously with the SRP RNA affects the structure of the final SRP19-SRP54-RNA ternary complex.

In vitro assembly of the native ternary complex (the 'SRP54-late' pathway) was followed by first allowing formation of a stable SRP19-RNA complex and then adding SRP54 (left panel, Figure 2.6). To model the hypothetical situation in which SRP19, SRP54 and the SRP RNA are free to assemble in the same compartment and during the same time interval, the *in vitro* assembly was performed by adding SRP19 to a mixture of free LS RNA and free SRP54 (right panel, Figure 2.6). Recall that SRP54 does not form a stable complex with the free LS RNA (Figure 2.5B). Thus, formation of any complex containing SRP54 must be induced by a binding event involving SRP19. This pathway is termed 'SRP54-early' assembly and the ternary complex formed via this pathway is called 'non-compartmentalized' complex.

2.4.3 Structure of the native SRP19-SRP54-RNA ternary complex

In an approach similar to that used to measure protein dissociation constants above, Chris L. Leonard performed phosphorothioate footprinting to quantify the accessibility of every nucleotide in SRP complexes. Protection from iodine-mediated cleavage reflects both

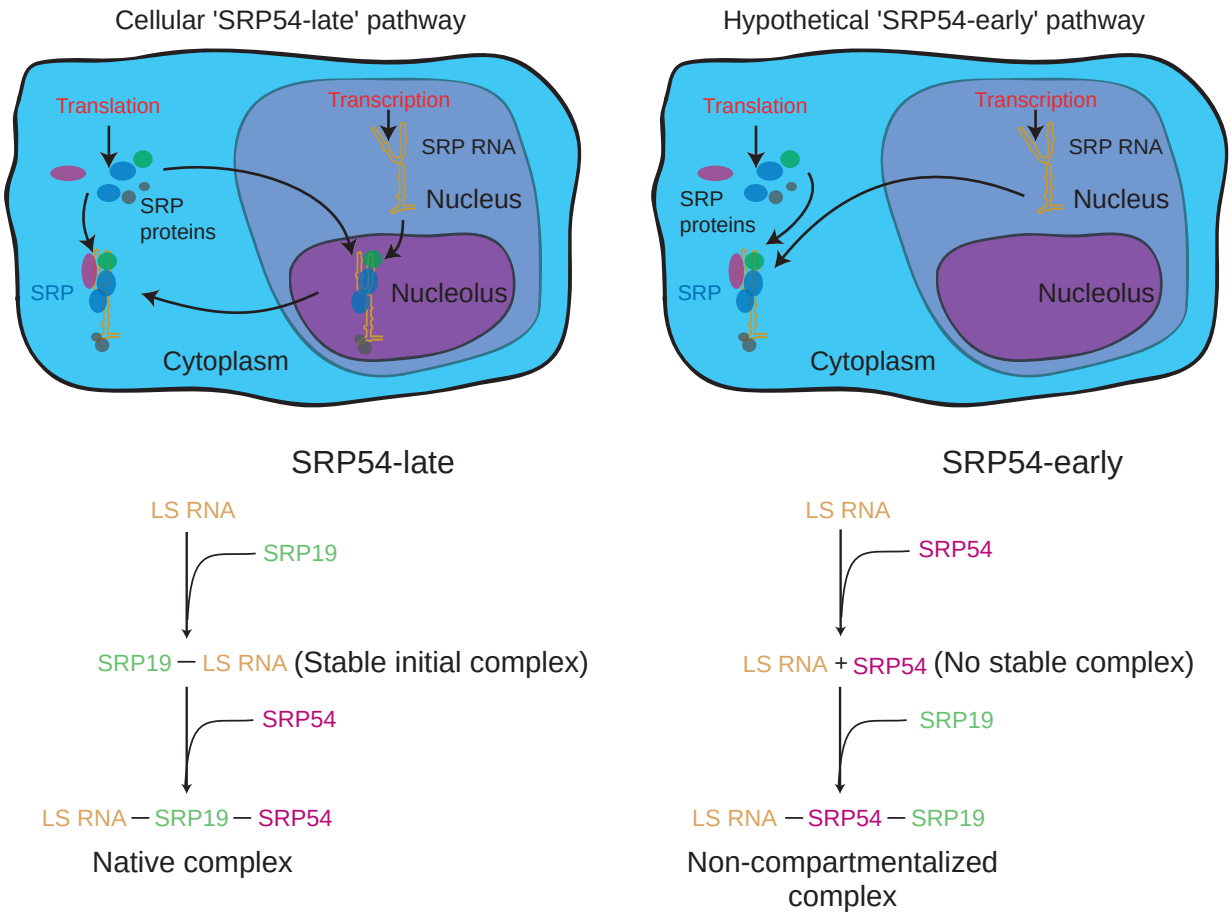

Figure 2.6. Schemes for *in vitro* SRP54-late and SRP54-early (non-compartmentalized) assemblies of the SRP54-SRP19-RNA ternary complex.

direct occlusion of the RNA backbone and protein-induced conformational changes in the RNA (*10, 28, 29*). Importantly, because changes in individual band intensities can be normalized to the many nucleotides whose reactivity does not change, even small changes in local environment are robustly scored by the phosphorothioate footprinting approach (*29*).

Cleavage intensities were quantified for entire sequencing gel lanes and representative data for experiments performed with RNAs containing phosphorothioate-substituted guanosine residues are shown in Figures 2.7A,B. In both panels, blue traces indicate cleavage intensities observed for the free LS RNA.

When phosphorothioate footprinting was performed on the SRP19-RNA complex, many nucleotides became protected from cleavage, as expected (SRP19 protection is summarized as green boxes in Figure 2.7A). Data obtained by evaluating LS RNAs containing each of the four phosphorothioate-substituted nucleotides are summarized in Figure 2.7C and are superimposed as a green backbone on a crystallographic structure for this complex (Figure 2.7D). SRP19-induced protection from iodine-mediated cleavage occurs exactly at the protein-RNA interface, in RNA regions that lie in close contact in the binary complex, and in structures that undergo a conformational change upon protein binding (Figure 2.7D).

Next, structural changes upon SRP54 binding to a pre-formed SRP19-RNA complex were evaluated (purple trace in Figure 2.7A). Nucleotides showing specific protection upon addition of SRP54 are emphasized with purple boxes and are summarized in the context of a secondary structure for the LS RNA in Figure 2.7C. Positions that show new or enhanced protection from iodine-mediated cleavage are largely localized at the SRP54 binding site and at neighboring regions in helix 6, as visualized in the context of the three-dimensional

structure for this ternary complex (Figure 2.7E). The excellent correlation between the footprinting experiments and the three-dimensional structures for these complexes (Figures 2.7D,E) indicates that phosphorothioate footprinting accurately reports protein binding sites and protein-induced conformational changes in the SRP RNA.

2.4.4 SRP ternary complexes formed via the SRP54-late versus SRP54-early pathways are distinct

Next, the structural consequences if the SRP19-SRP54-RNA complex assembles via the SRP54-early pathway were evaluated (right panel, 2.6). Importantly, the final solution compositions were the same for complexes formed via either pathway but differed only in the order of addition of SRP19 and SRP54.

For many positions, the observed protection was identical for complexes formed via either pathway (for example, see positions 187-188 and 197-198 in Figures 2.7A,B). In strong contrast, at many other positions, protection from iodine-mediated cleavage was significantly reduced for complexes formed by adding SRP54 prior to SRP19 (emphasized with filled spheres in Figures 2.7B,C). Superposition of these weaker and missing protections on the three-dimensional structure of the SRP19-SRP54-RNA ternary complex indicates that structural changes occur in RNA regions close to both SRP19 and SRP54 binding sites (black backbone, Figure 2.7F).

These phosphorothioate footprinting experiments thus demonstrate that structurally distinct complexes form depending on whether SRP54 is present or absent as SRP19 assembles with the RNA.

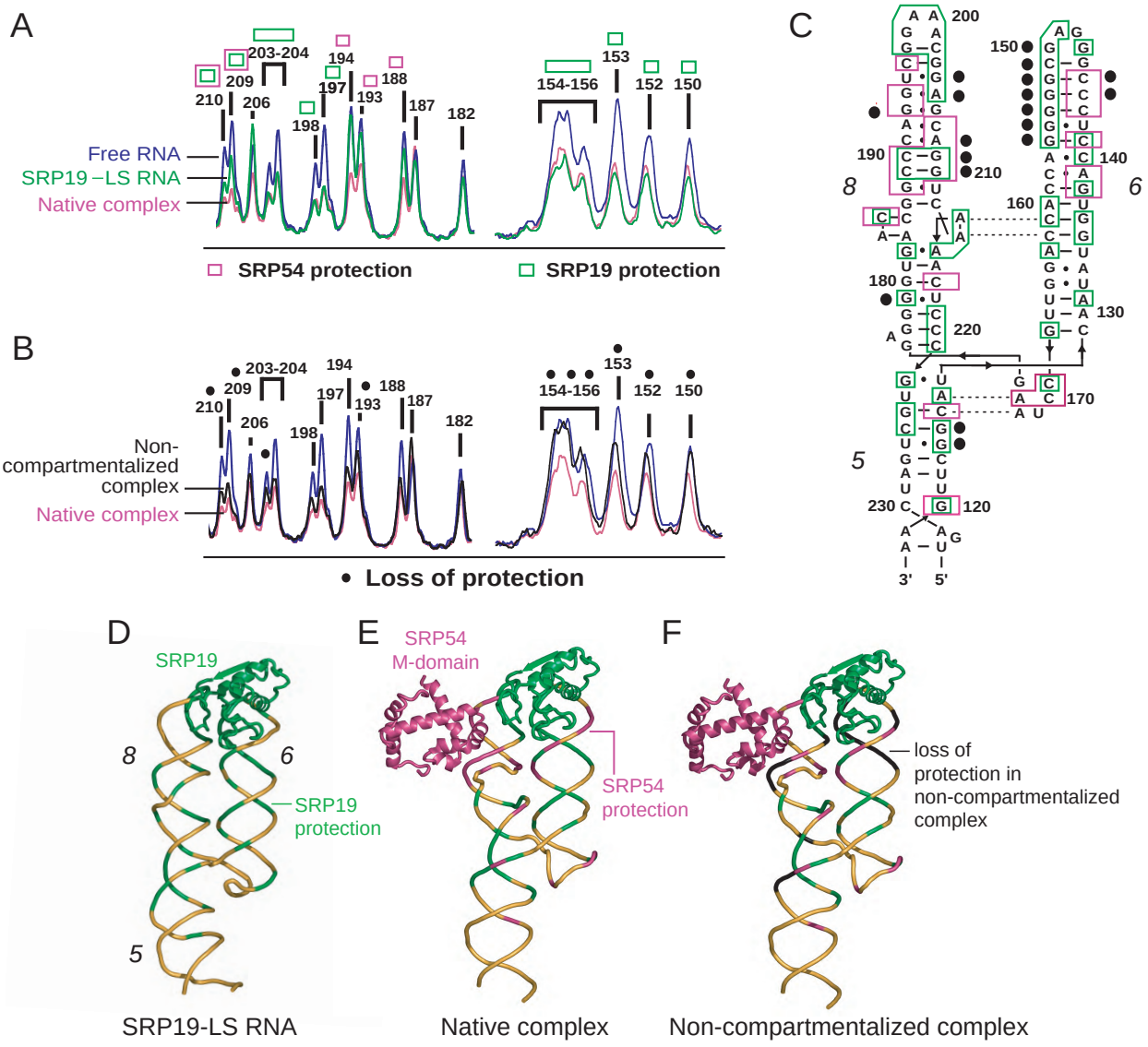

Figure 2.7. Distinct structures for SRP19-SRP54-LS RNA ternary complexes as a function of order of assembly. (A) Representative iodine mediated cleavage intensities using phosphorothioate-substituted guanosines for the free LS RNA (blue), SRP19-LS RNA complex (green) and the native SRP19-SRP54-LS RNA (purple) complex. Positions that become protected upon SRP19 or SRP54 binding are emphasized with green and purple boxes, respectively. (B) Phosphorothioate footprints illustrating structural differences in the native (purple) and non-compartmentalized (black) ternary complexes. Sites where protection is reduced in the non-compartmentalized complex relative to the native complex are emphasized with black spheres. (C) Superposition of SRP19- and SRP54-induced protection (green and purple boxes, respectively) on the secondary structure of the LS RNA. Missing or reduced protections in the non-compartmentalized complex are indicated with black spheres. (D, E, F) SRP19- and SRP54-induced footprints superimposed on three-dimensional structures for the SRP19-LS RNA binary *(11)* and the SRP19-SRP54-LS RNA ternary *(12)* complexes, respectively.

2.4.5 SRP19-RNA interactions mapped by site-directed cleavage

The phosphorothioate footprinting experiments provide definitive evidence that the structures of SRP complexes formed via the SRP54-late and SRP54-early pathways are different. Site-directed hydroxyl radical cleavage was used to obtain detailed views of the structural differences in these two ternary complexes.

In a complex with the SRP RNA, the SRP19 protein spans two structural elements (*12*). SRP19 contains a core domain comprised of a three-stranded β-sheet packed against two α-helices. The second structural element is comprised of two irregular loops that extend from the SRP19 core (Figure 2.8). Direct contacts with the SRP RNA involve multiple interactions mediated by the two irregular loops, plus contacts mediated by residues extending from the first β-strand and the first α-helix in the core (β1 and α1 in Figure 2.8, respectively). Therefore interactions between the RNA and SRP19 were monitored by performing site-directed cleavage experiments using the Fe(II)-BABE reagent tethered at both SRP19 core and loop regions (Figure 2.8).

Four cysteine residues in the native SRP19 sequence were mutated to create a ΔCys parent construct. Unique solvent accessible cysteine residues were then individually introduced into each of the two RNA binding loops (at positions 31 and 72) and into the SRP19 core (at positions 93 and 106) (colored spheres in Figure 2.8). RNA binding affinities for each SRP19 variant were within 3-8 fold of that for the wild type protein. Conjugation with Fe(II)-BABE had no additional effect on binding for any of the SRP19 variants. The conjugation of Fe(II)-BABE with SRP19 was visualized in SDS-PAGE (Figure 2.9). The conjugated protein moved slower than free SRP19.

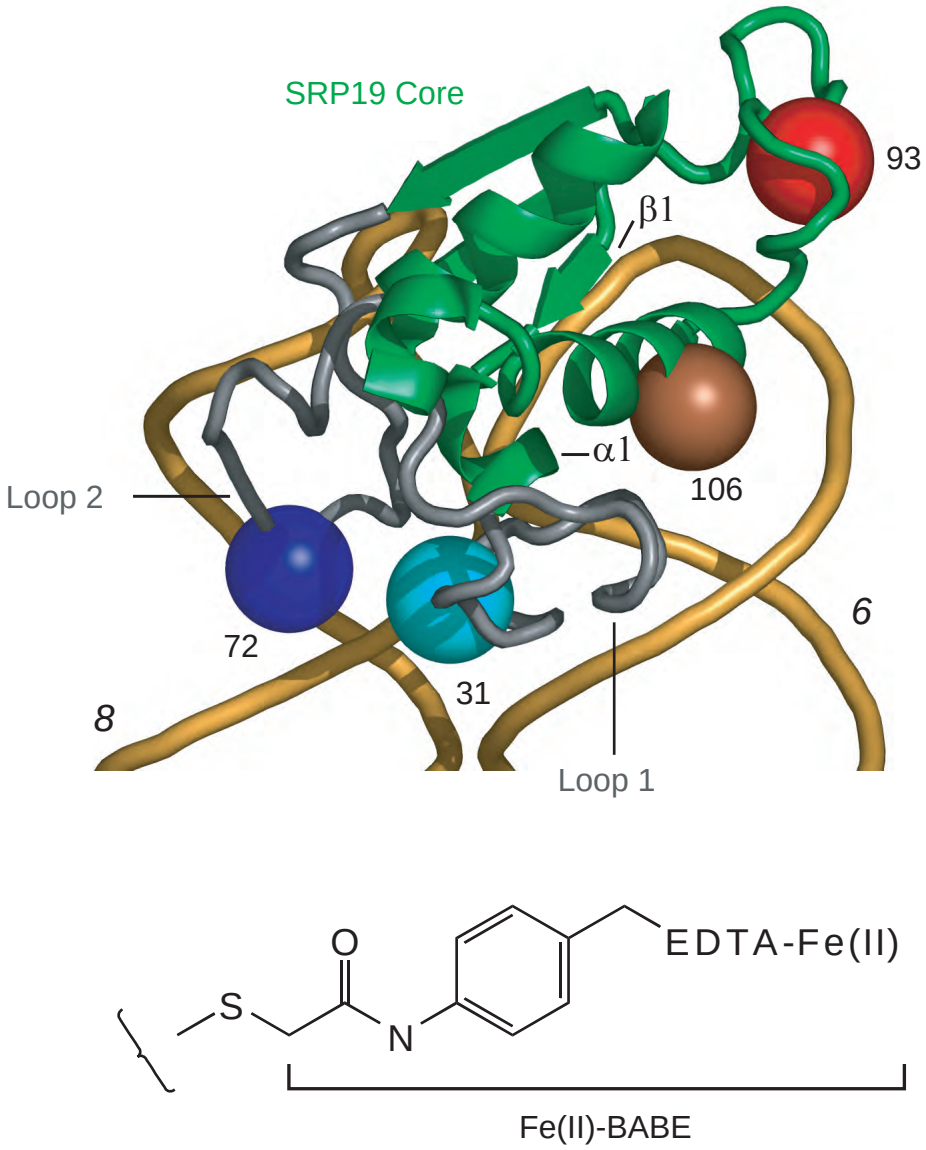

Figure 2.8. SRP19 structure and the sites of Fe(II)-BABE derivatization. The SRP19 core is green, and the RNA binding-loops are gray. The sites of unique cysteine residues used for site-specific conjugation with Fe(II)-BABE reagent are shown as spheres.

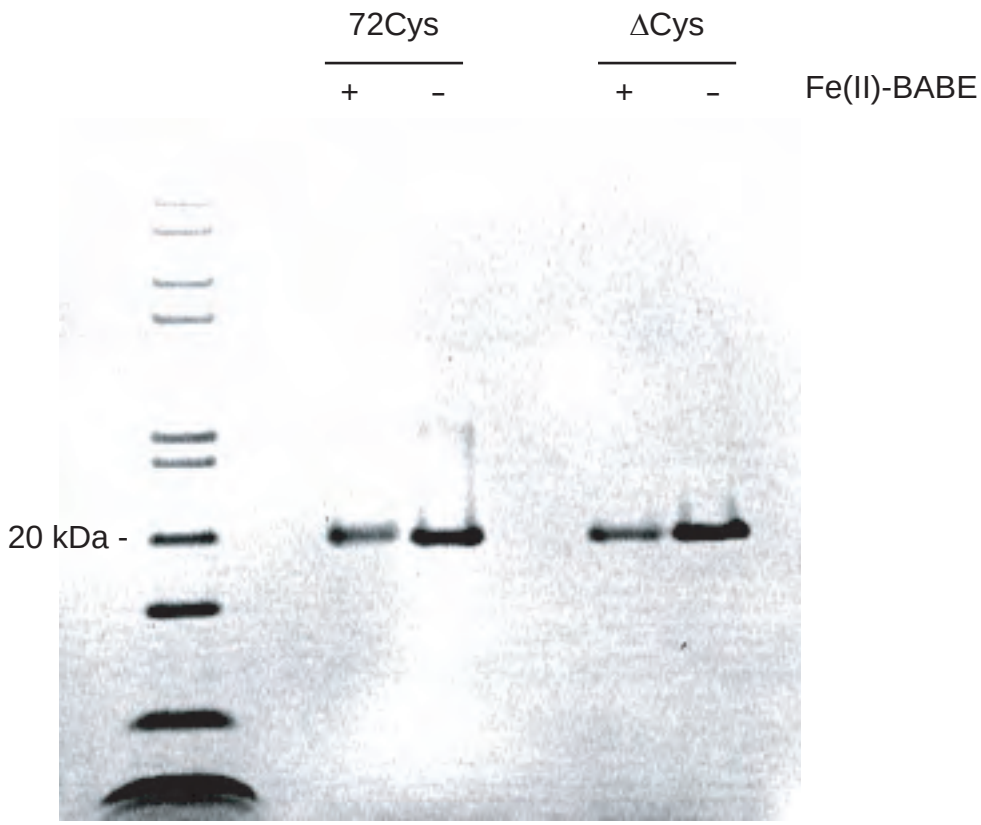

Figure 2.9. SDS PAGE of Fe(II)-BABE derivatized SRP19. Fe(II)-BABE-tethered 72Cys-SRP19 moves slightly slower than underivatized protein or Fe(II)-BABE treated ΔCys-SRP19 protein.

Site-directed cleavage experiments were initially performed for simple binary complexes containing the LS RNA and each of the four SRP19 proteins. Upon addition of reagents, the tethered Fe(II)-BABE group produced hydroxyl radicals that cleaved nearby regions of the RNA backbone. Specific cleavages were identified relative to mock reactions performed using the ΔCys parent construct (Figure 2.10, gray histograms). SRP19 variants derivatized at either of the two RNA binding loops (positions 31 and 72) and at the core (positions 93 and 106) yield distinctive and non-overlapping cleavage patterns at the SRP RNA backbone that are exactly consistent with the structure of this complex (see structures on right hand side of Figure 2.10). Thus, site-directed cleavage experiments accurately report native RNA-protein interactions mediated by both the RNA-binding loops and core domain of SRP19.

2.4.6 RNA-binding loops fold differently in the non-compartmentalized complex

Next, the structural consequences of forming the SRP19-SRP54-LS RNA ternary complex by each of the two assembly pathways were evaluated. When site-directed hydroxyl radical cleavage experiments were performed on the native ternary complex (formed via SRP54-late pathway), the pattern of cleavage was largely unchanged for all four SRP19 constructs (compare green and purple histograms, Figure 2.10).

When identical hydroxyl cleavage experiments were performed on the non-compartmentalized complex (formed via SRP54-early pathway), cleavage intensities using SRP19 derivatized in the core (positions 93 and 106) were essentially identical to those observed for the native complex (see black histograms for 93Cys and 106Cys SRP19 variants; lower panels, Figure 2.10). In strong contrast, when the structure of the non-compartmentalized complex was monitored using SRP19 proteins derivatized with Fe(II)-

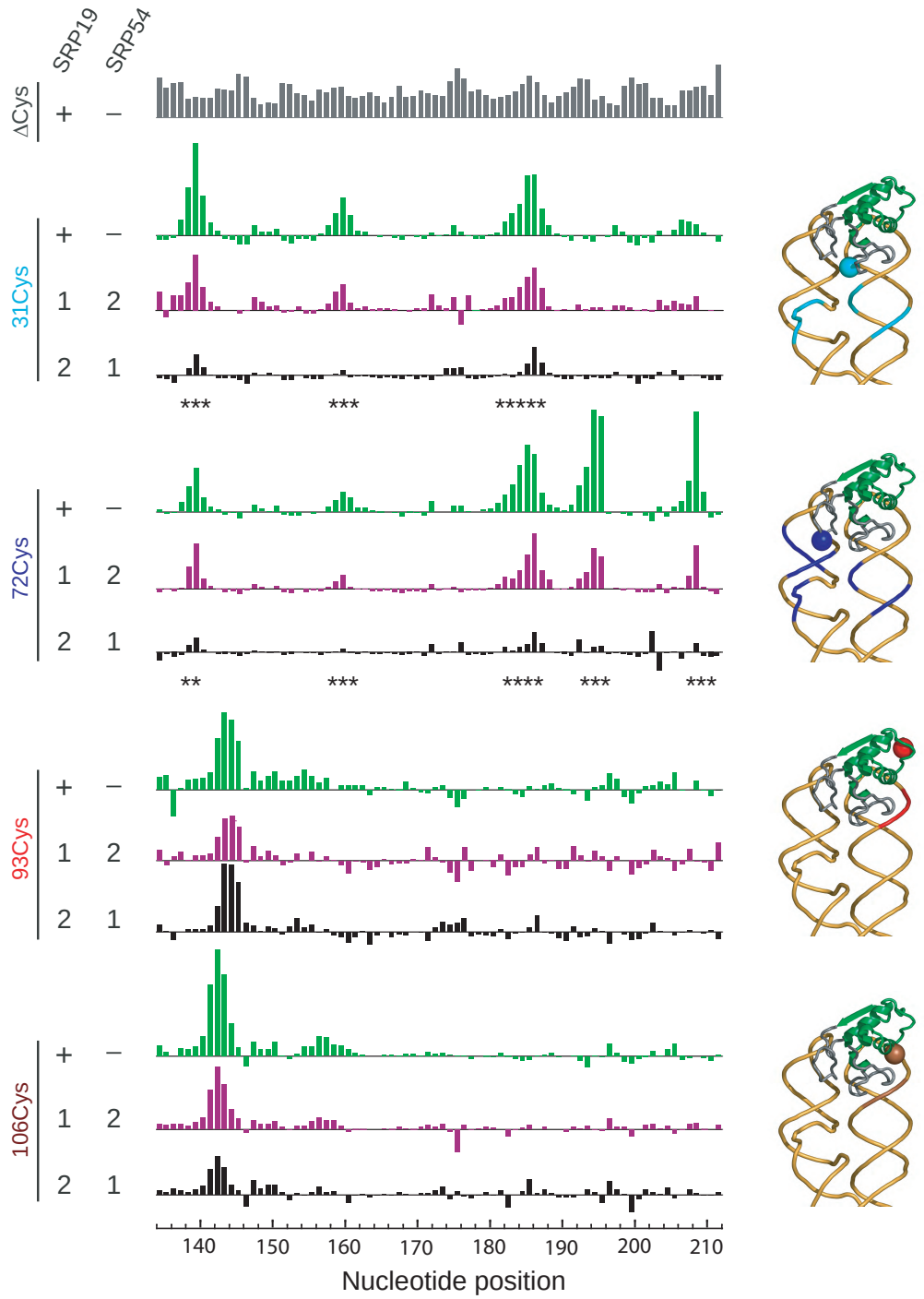

Figure 2.10. Structures of SRP19 in the native and non-compartmentalized complexes are different. Site-specific cleavage histograms for each SRP19 variant are shown for the binary SRP19-RNA (green), native (purple) and non-compartmentalized (black) complexes. Missing cleavages in the non-compartmentalized complex are marked by asterisks. Right-hand panels illustrate site-directed cleavage information for the binary SRP19-RNA complexes superimposed on its three-dimensional structure *(11)*.

BABE at loop 1 or loop 2, specific RNA cleavages were either missing or significantly reduced in intensity (see black histograms for 31Cys and 72Cys, respectively; upper panels, Figure 2.10). These results indicate that the SRP19 core domain interacts similarly with the LS RNA in both native and non-compartmentalized complexes while SRP19 loops 1 and 2 fail to form native interactions with the RNA when the ternary complex is formed via the SRP54-early pathway.

2.4.7 The non-compartmentalized complex is stable

The kinetic stability of the non-compartmentalized complex was evaluated by monitoring recovery of the 31Cys and 72Cys cleavages as a function of time. Site-directed cleavage intensities observed for the complex formed via the SRP54-early pathway were compared to those observed in the native complex. For the 31Cys protein, cleavage intensities at positions 138-140 and 159-161 recover slowly over a period of 1 h (Figure 2.11A). The rate constant for achieving a native-like cleavage pattern is 0.013 min^{-1}, corresponding to a half-life of 54 min (Figure 2.11B). In contrast, the cleavage pattern of the 72Cys protein shows no detectable recovery to the native conformation over 1 h (Figures 2.11C,D). These results demonstrate that the non-compartmentalized complex is extremely stable and that the two RNA-binding loops rearrange to a native-like conformation at different rates; recovery of loop 2 is much slower than loop 1.

2.5 Discussion

To date, essentially all models for assembly of multi-component ribonucleoproteins, including the ribosome, tacitly assume that binding by any given protein component either facilitates further RNP assembly or has no effect on continued assembly. Above experiments

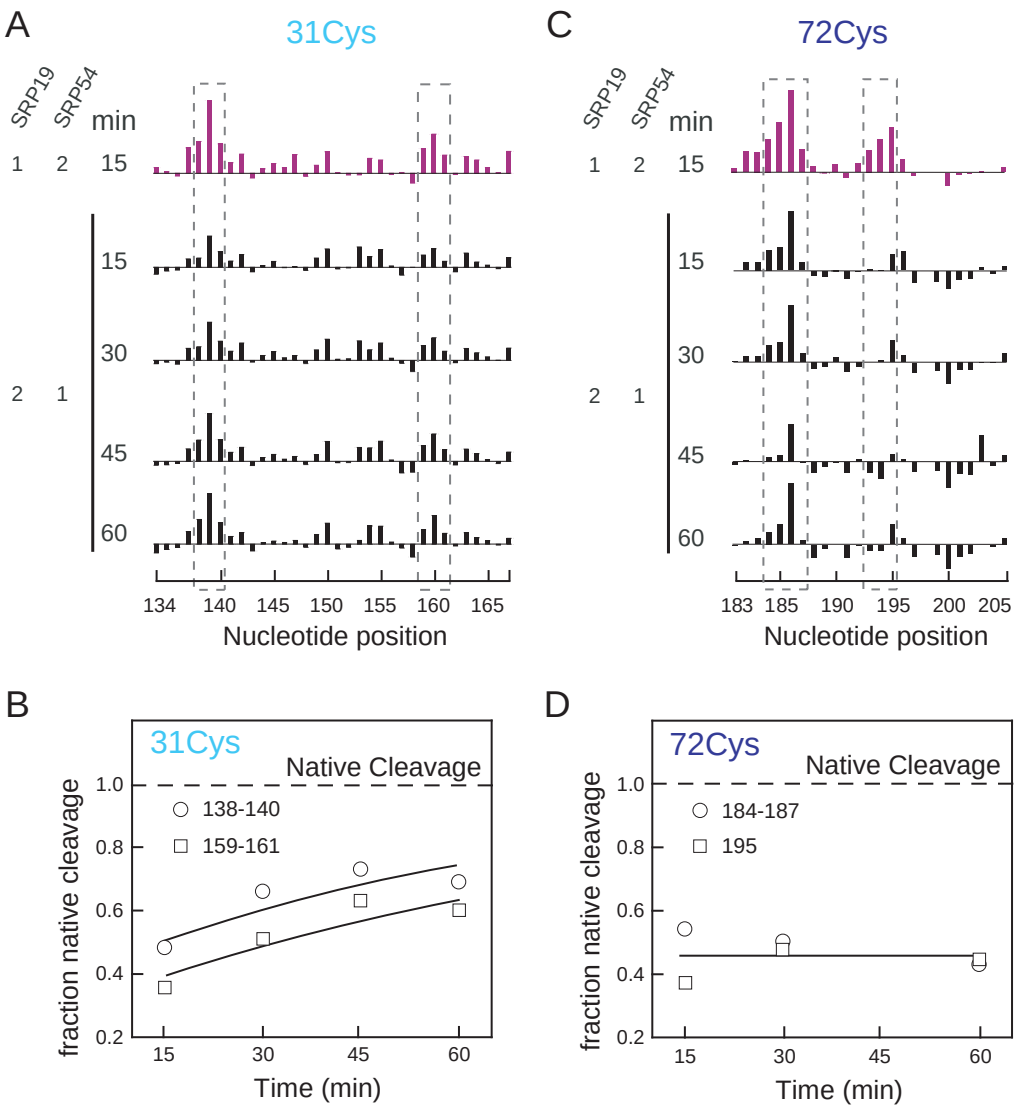

Figure 2.11. Kinetic stability of the non-compartmentalized complex. (A, C) Site directed hydroxyl radical cleavage. SRP19 and SRP54 were added in the orders shown. Site-directed cleavage from position 31 or 72 was initiated at varying times after initial complex formation. RNA sites where cleavage is selectively lost in the non-compartmentalized ternary complex are emphasized with dashed boxes. (B, D) Recovery of native cleavage patterns as a function of time. Data for 31Cys were fit to a single exponential, whereas no detectable recovery was observed for the 72Cys protein after 1 h.

reveal an unanticipated and additional dimension to RNP biogenesis, namely that an untimely interaction can disrupt formation of the native RNP. It has been shown that SRP54 is able to interfere with native assembly of SRP19 with the SRP RNA *in vitro*, a situation which is presumably avoided *in vivo* by differential nuclear and cytoplasmic compartmentalization.

2.5.1 Structure of the non-compartmentalized complex

Using nucleotide resolution data detailed in previous section and previously published crystallographic data for the SRP19-RNA (*11*) and SRP19-SRP54-RNA (*12*) complexes, a structural model for the non-compartmentalized complex was built. In the native ternary complex, SRP19, SRP54 and the SRP RNA each contact both of the other two components (circled, Figure 2.12A). Contacts between SRP19 and the RNA in the native complex are mediated by two loops that extend from the core of the protein plus additional interactions involving the first β-strand and first α-helix in the core (Figure 2.8). SRP19 is a natively unfolded protein and these RNA-binding loops, especially, are only likely to fold to their native conformations when bound to RNA.

When the Fe(II)-BABE reagent was attached at positions 93 or 106 in the SRP19 core, hydroxyl radical RNA cleavages were similar in both native and non-compartmentalized complexes. In strong contrast, when the cleavage agent was attached at the RNA binding loops (positions 31 and 72), RNA cleavages were either greatly reduced or missing altogether in the non-compartmentalized complex. These results indicate that in the non-compartmentalized complex, the SRP19 core is positioned on the RNA in a manner similar to that in the native complex; whereas, loop 1 and 2 misfold and fail to form native contacts with the RNA (Figure 2.12B). This structural interpretation is supported by iodine-

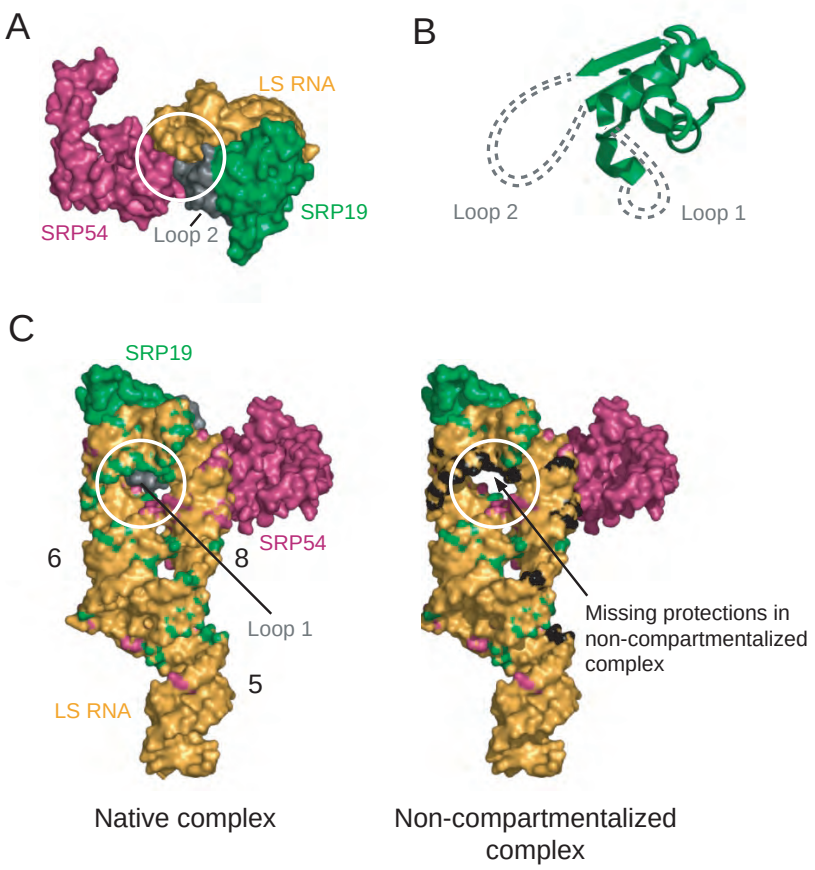

Figure 2.12. Structures for native and non-compartmentalized SRP complexes. (A) Intimate contacts among SRP19, SRP54, and LS RNA in the native ternary complex. Loop 2 in SRP19 (in gray) is sandwiched between SRP54 and the RNA (white circle). (B) Schematic structure for SRP19 in the non-compartmentalized complex. (C) RNA sites that interact with SRP19 loop 1 in the native complex coincide with positions at which protection from iodine-mediated cleavage is lost in the non-compartmentalized complex (black surface).

mediated phosphorothioate footprinting experiments. In the native complex, loop 1 fills a hole in the RNA fold and results in phosphorothioate footprinting protection on the RNA face opposite to where SRP19 binds (see circle in Figure 2.12C). In the non-compartmentalized complex, loop 1 misfolds and backbone groups at the circumference of the internal hole in the RNA show enhanced reactivities relative to the native complex (black surface residues, Figure 2.12C). Residues that interact with loop 2 also show enhanced phosphorothioate reactivities in the non-compartmentalized complex at positions 204-205 in helix 6 of the RNA (see Figure 2.7F).

2.5.2 Mechanisms for SRP54-late and SRP54-early assembly

Two additional pieces of information allow proposing mechanisms for SRP54-late versus SRP54-early assembly of the SRP19-SRP54-RNA ternary complex. First, inspection of the protein-RNA interfaces in the native ternary complex (Figure 2.12A) suggests that SRP54 abuts the other two components and can, in principle, bind approximately as a rigid unit to a partially formed SRP19-RNA complex. In contrast, binding by SRP19 requires that loop 2 be inserted under the existing SRP54-RNA interface. If this 'folding under' step were sterically disfavored, a non-native complex would result in which loop 2 in SRP19 is misfolded. Loop 1 would also presumably misfold because folding of loop 1 and loop 2 appear to be linked.

Second, binding by SRP19 to the RNA involves formation of at least two intermediate complexes, termed the Encounter and Stable complexes, that form with fast kinetics (*10*). Subsequently, the intermediate complexes fold slowly to form the native complex:

$$\text{RNA + SRP19} \xrightarrow{\text{fast}} \text{Encounter/Stable} \xrightarrow{\text{slow}} \text{SRP19–LS RNA}$$

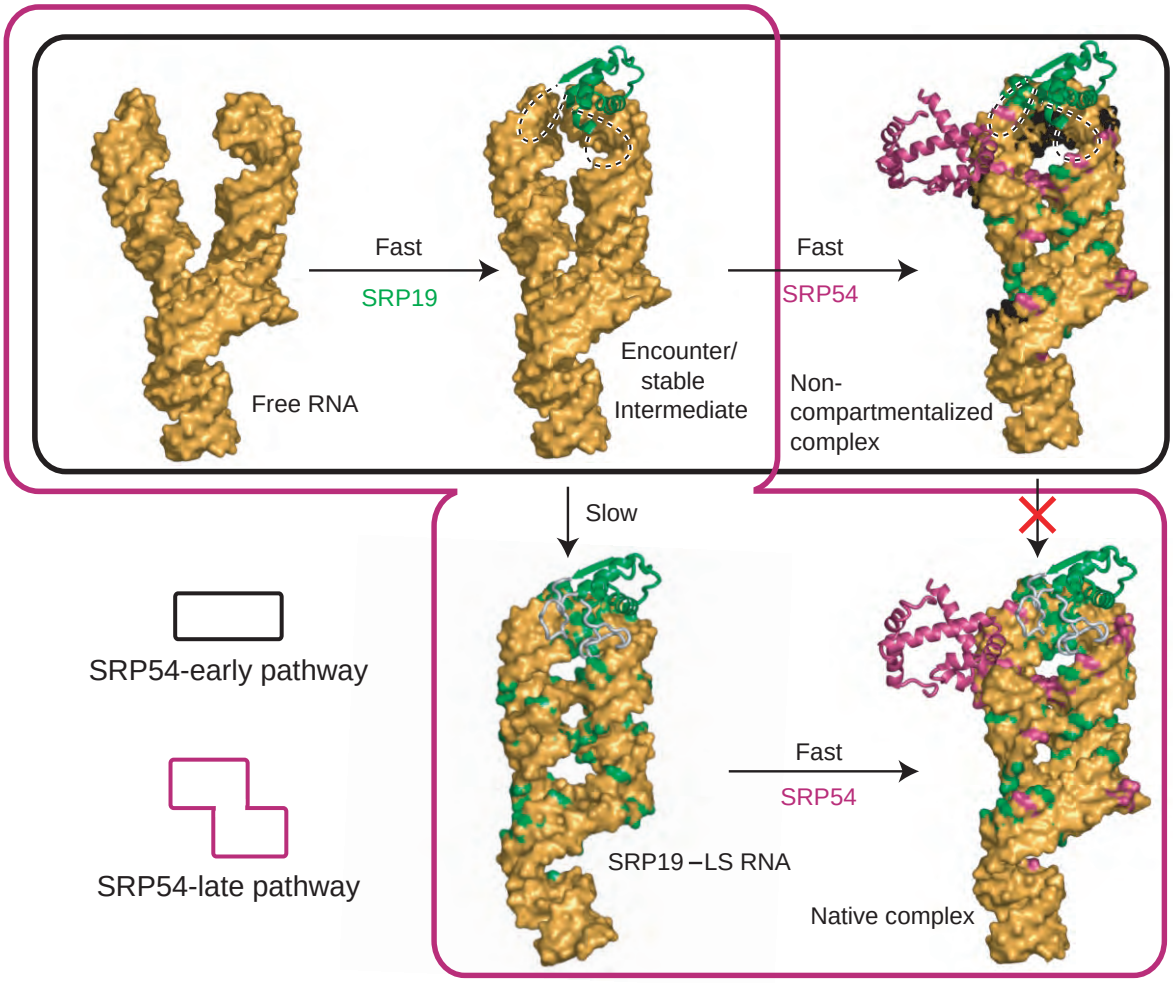

Figure 2.13. Assembly of the SRP19-SRP54-LS RNA ternary complex via an intermediate state involving partially folded SRP19. SRP54-late and SRP54-early pathways are emphasized in purple and black boxes, respectively. The RNA surface is in yellow; positions protected by SRP19 or SRP54 are in green and purple, respectively. Missing protections in the non-compartmentalized complex are in black. The red X indicates that the non-compartmentalized complex converts to the native complex very slowly.

In this proposed mechanism for assembly of the SRP19-SRP54-RNA ternary complex, the free RNA is initially in a relatively open conformation as supported by the absence of a stable hydroxyl radical footprint (see free RNA, Figure 2.13) (*10*). SRP19 binds rapidly to the free RNA to form the Encounter/Stable intermediate. In the intermediate complex, the SRP19 core interacts in a near-native way with the RNA; whereas, loop 1 and 2 do not form native interactions with the RNA (see intermediate complex, Figure 2.13). In the intermediate complex, sufficient global reorganization of the RNA has occurred to permit stable binding by SRP54. Formation of this intermediate complex is the same for assembly via either SRP54-late or SRP54-early pathways.

If SRP54 is not present at this stage, previous work shows that the SRP19-RNA complex resolves slowly to a native bimolecular complex (lower pathway, Figure 2.13). Once the stage requiring compartmentalized assembly is completed, SRP54 can bind to the SRP19-RNA complex to form the native ternary complex. Native ternary complex formation involves additional conformational changes in the RNA (purple regions in the native complex; Figure 2.13).

In contrast, if SRP54 is present during the phase when the Encounter/Stable intermediate forms, SRP54 binds rapidly to the pre-organized RNA to form the non-compartmentalized complex. The non-compartmentalized complex is characterized by some of the same SRP54-induced changes that occur in the native ternary complex. However, early binding by SRP54 inhibits some SRP19 folding events that take place during slow conversion of the intermediate SRP19-RNA complex into the native SRP19-RNA complex. As a result, RNA-binding loops 1 and 2 remain misfolded in the non-compartmentalized

complex (see dashed protein loops and black RNA backbone in non-compartmentalized complex, Figure 2.13).

2.5.3 Role of compartmentalization to sequester immature RNPs during assembly

These results show that SRP54 can disrupt native SRP19-RNA assembly, implying that SRP54 must be sequestered, as apparently occurs *in vivo*, for proper assembly of the SRP to occur. Given the profound effect of compartmentalization on assembly of this relatively simple three-component system, cellular compartmentalization may broadly direct native assembly of other multi-component RNPs.

2.6 References

1. Doudna, J. A., and Batey, R. T. (2004) Structural insights into the signal recognition particle. *Annu. Rev. Biochem. 73*, 539-557.

2. Egea, P. F., Stroud, R. M., and Walter, P. (2005) Targeting proteins to membranes: structure of the signal recognition particle. *Curr. Opin. Struct. Biol. 15*, 213-220.

3. Shan, S., and Walter, P. (2005) Co-translational protein targeting by the signal recognition particle. *FEBS Letters 579*, 921-926.

4. Pool, M. R. (2005) Signal recognition particles in chloroplasts, bacteria, yeast and mammals. *Mol. Membr. Biol. 22*, 3-15.

5. Stroud, R. M., and Walter, P. (1999) Signal sequence recognition and protein targeting. *Curr. Opin. Struct. Biol. 9*, 754-759.

6. Halic, M., Becker, T., Pool, M. R., Spahn, C. M. T., Grassucci, R. A., Frank, J., and Beckmann, R. (2004) Structure of the signal recognition particle interacting with the elongation-arrested ribosome. *Nature 427*, 808-814.

7. Focia, P. J., Shepotinovskaya, I. V., Seidler, J. A., and Freymann, D. M. (2004) Heterodimeric GTPase core of the SRP targeting complex. *Science 303*, 373-377.

8. Siegel, V., and Walter, P. (1988) Each of the activities of signal recognition particle (SRP) is contained within a distinct domain: Analysis of biochemical mutants of SRP. *Cell 52*, 39-49.

9. Diener, J. L., and Wilson, C. (2000) Role of SRP19 in assembly of the *Archaeoglobus fulgidus* signal recognition particle. *Biochemistry 39*, 12862-12874.

10. Rose, M. A., and Weeks, K. M. (2001) Visualizing induced fit in early assembly of the human signal recognition particle. *Nat. Struct. Biol. 8*, 515-520.

11. Oubridge, C., Kuglstatter, A., Jovine, L., and Nagai, K. (2002) Crystal Structure of SRP19 in complex with the S domain of SRP RNA and its implication for the assembly of the signal recognition particle. *Mol. Cell 9*, 1251-1261.

12. Kuglstatter, A., Oubridge, C., and Nagai, K. (2002) Induced structural changes of 7SL RNA during the assembly of human signal recognition particle. *Nat. Struct. Biol. 9*, 740-744.

13. Hainzl, T., Huang, S., and Sauer-Eriksson, A. E. (2005) Structural insights into SRP RNA: an induced fit mechanism for SRP assembly. *RNA 11*, 1043-1150.

14. Hann, B. C., and Walter, P. (1991) The signal recognition particle in *S. cerevisiae*. *Cell 67*, 131-144.

15. Brown, J. D., Hann, B. C., Medzihradszky, K. F., Niwa, M., Burlingame, A. L., and Walter, P. (1994) Subunits of the Saccharomyces cerevisiae signal recognition particle required for its functional expression. *EMBO J. 13,* 4390-4000.

16. Herskovits, A. A., Bochkareva, E. S., and Bibi, E. (2000) New prospects in studying the bacterial signal recognition particle pathway. *Mol. Microbiol. 38,* 927-939.

17. Ciufo, L. F., and Brown, J. D. (2000) Nuclear export of yeast signal recognition particle lacking Srp54p by the Xpo1p/Crm1p NES-dependent pathway. *Curr. Biol. 10,* 1256-1264.

18. Grosshans, H., Deinert, K., Hurt, E., and Simos, G. (2001) Biogenesis of the signal recognition particle (SRP) involves import of SRP proteins into the nucleolus, assembly with the SRP-RNA, and Xpo1p-mediated export. *J. Cell Biol. 153,* 745-761.

19. Jacobson, M. R., and Pederson, T. (1998) Localization of signal recognition particle RNA in the nucleolus of mammalian cells. *Proc. Natl. Acad. Sci. USA 95,* 7981-7986.

20. Politz, J. C., Yarovoi, S., Kilroy, S. M., Gowda, K., Zwieb, C., and Pederson, T. (2000) Signal recognition particle components in the nucleolus. *Proc. Natl. Acad. Sci. USA 97,* 55-60.

21. Alavian, C. N., Politz, J. C. R., Lewandowski, L. B., Powers, C. M., and Pederson, T. (2004) Nuclear export of signal recognition particle RNA in mammalian cells. *Biochem. Biophys. Res. Commun. 313,* 351-355.

22. Walter, P., and Blobel, G. (1983) Disassembly and reconstitution of signal recognition particle. *Cell 34,* 525-533.

23. Gowda, K., Black, S. D., Moeller, I., Sakakibara, Y., Liu, M.-C., and Zwieb, C. (1998) Protein SRP54 of human signal recognition particle: Cloning, expression, and comparative analysis of functional sites. *Gene 207,* 197-207.

24. Zwieb, C. (1991) Interaction of protein SRP19 with signal recognition particle RNA lacking individual RNA-helices. *Nucl. Acids Res. 19,* 2955-2960.

25. Das, R., Laederach, A., Pearlman, S. M., Herschlag, D., and Altman, R. B. (2005) Semi-automated footprinting analysis software for high-throughput quantification of nucleic acid footprinting experiments. *RNA 11,* 344-354.

26. Henry, K. A., Zwieb, C., and Fried, H. M. (1997) Purification and biochemical characterization of the 19-kDa signal recognition particle RNA-binding protein expressed as a hexahistidine-tagged polypeptide in *Escherichia coli*. *Protein Exp. Pur. 9,* 15026-15033.

27. Dean, K. A., von Ahsen, O., Gorlich, D., and Fried, H. M. (2001) Signal recognition particle protein 19 is imported into nucleus by importin 8 (RanBP8) and transportin. *J. Cell Sci. 114*, 3479-3485.

28. Webb, A. E., Rose, M. A., Westhof, E., and Weeks, K. M. (2001) Protein-dependent transition states for ribonucleoprotein assembly. *J. Mol. Biol. 309*, 1087-1100.

29. Garcia, I., and Weeks, K. M. (2004) Structural basis for the self-chaperoning function of an RNA collapsed state. *Biochemistry 43*, 15179-15186.

Chapter 3

A Three-fold RNA-Protein Interface in the Signal Recognition Particle Gates Native Complex Assembly

3.1 Introduction

Assembly of most ribonucleoprotein (RNP) complexes is accompanied by significant conformational changes in both protein and RNA components (*1, 2*). In some cases, these conformational changes may occur in a progressive fashion such that early interactions in assembly lead to further conformational rearrangements that uniformly facilitate later steps. Several structurally linked steps in assembly of the 30*S* ribosomal subunit appear to proceed in this manner (*3, 4*). However, in view of the multiplicity of RNA-protein and protein-protein interactions that can potentially occur during assembly of multi-component RNPs, the extent to which incorrect or premature interactions among components might interfere with native complex formation remains to be assessed. The idea that some RNA (*5, 6*) and protein (*7, 8*) molecules readily adopt stable, but misfolded, states is now well established. In Chapter 2 a striking example of robust misassembly in the mammalian signal recognition particle has been identified. This discovery extends the concept of kinetically trapped, non-native conformational states to multi-component RNP complexes. In this chapter the kinetic mechanism for this misassembly is analyzed.

Mammalian SRP19 is unstructured in its unbound state and assembles with the SRP RNA via formation of multiple obligatory intermediate complexes (*9*). Assembly of the SRP19-RNA complex is an example of mutually-induced fit because both SRP19 and the SRP RNA undergo significant conformational rearrangements during assembly. A native ternary complex forms *in vitro* when SRP54 binds to the stable and preformed SRP19-SRP RNA complex (see Figure 2.13 in Chapter 2) and is the same as the complex visualized in crystallographic studies (*10*). This ‘SRP54-late’ *in vitro* assembly pathway mimics the two-step, or compartmentalized, *in vivo* assembly pathway (*11-14*).

In contrast, if SRP19 and SRP54 are allowed simultaneous access to the SRP RNA *in vitro*, these three components interact robustly to form a distinct, non-native, complex (see Figure 2.13). In this complex, two RNA binding loops in SRP19 remain misfolded (black dashed lines in the non-compartmentalized complex, Figure 2.13). Here it is shown that, beginning with identical sets of protein and RNA components, the 'non-compartmentalized' structure arises from the surprising ability of SRP54 to bind an SRP19-RNA assembly intermediate; the resulting cleft-like interface that forms between SRP54 and the SRP RNA (Figure 2.12A) is sufficiently narrow that it disfavors insertion of an RNA-binding loop from SRP19 that normally occurs in the native complex.

3.2 Materials and methods

3.2.1 Preparation of SRP RNA and SRP54

Native and A149U mutant RNAs spanning nts 101-255 of the human SRP RNA (LS RNA) were transcribed as described in Chapter 2. The 5'-truncated native and A149U mutant LS RNAs were transcribed from PCR-generated templates. All RNAs were refolded by heating to 95 °C (1 min), snap cooling at 0 °C, incubating at 60 °C (10 min) in RNA refolding buffer [300 mM potassium acetate (pH 7.6), 5 mM $MgCl_2$, 20 mM Hepes (pH 7.6), 0.01% (v/v) Triton], followed by slow cooling to room temperature (~40 min). The Alexa 555-labeled LS RNA was generated by co-folding of the appropriate 5'-truncated RNA and a fluorescently labeled DNA oligonucleotide (Trilink) (see Figure 2B). SRP54 was expressed and purified as described in Chapter 2.

3.2.2 BODIPY-FL and Alexa 488 labeled SRP19 variants

Single cysteine (E31C, W72C, L93C or L106C) SRP19 variant proteins were expressed in *E. coli* strain BL21-CodonPlus(DE3)-RIL (Stratagene) and purified as described in chapter 2, except that the final dialysis buffer was pH 7.2 and contained 2 mM TCEP as the reducing agent. SRP19-fluorophore conjugates were generated by treating each protein (~20 μM) with a 50-100 fold molar excess of a BODIPY-FL or Alexa 488 fluorophore maleimide derivative (22 °C, 2 h; Molecular probes). Unreacted fluorophore was removed by incubating the protein with an Ni^{2+}-NTA slurry (Invitrogen) and washing extensively with protein dilution buffer (PDB) [300 mM NaCl, 50 mM sodium phosphate (pH, 8.0), 10 mM 2-mercaptoethanol]. Fluorophore-labeled proteins were eluted in PDB containing 200 mM imidazole, subjected to dialysis to remove imidazole, and stored in PDB supplemented with 50% (v/v) glycerol at –20 °C. The extent of derivatization was calculated from the UV absorbance at 280 nm (protein) and 500 nm (fluorophore). For all Alexa labeled SRP19 the extent of derivatization were about 100% and for BODIPY-FL fluorophore tethered to SRP19 positions 72 and 106 the extent of derivatization were about 30%. Equilibrium dissociation constants for all SRP19-fluorophore derivatives were determined by filter partitioning (*9*) using internally labeled [^{32}P]-LS RNA (0.01 nM) or the Alexa 555 fluorophore RNA-DNA hybrid. Dissociation constants were within 3-fold of that for the native SRP19-LS RNA complex for all fluorophore-containing complexes (native SRP19, 5 nM; ΔCysSRP19, 4 nM; Alexa 488-31CysSRP19, 11 nM; Alexa 488-72CysSRP19, 1 nM; Alexa 488-93CysSRP19, 3 nM; Alexa 488-106CysSRP19, 11 nM, BODIPY-FL-72CysSRP19, 4 nM; BODIPY-FL-106CysSRP19, 19 nM).

3.2.3 Monitoring the SRP assembly pathway using FRET and single fluorophore experiments

Fluorescent measurements were performed in a Varian/Cary Eclipse Spectrofluorometer. Final reaction mixtures (22 °C, 500 µl) contained RNA refolding buffer supplemented with 1/5 vol PDB. Calibration between different measurements, when required, was performed using an inert Alexa 647 reference fluorophore. Formation of the Encounter complex between SRP19 and the SRP RNA was monitored via fluorescence resonance energy transfer (FRET) between 20 nM Alexa 488-labeled 31Cys or 72Cys SRP19 variants and 25 nM Alexa 555-labeled LS RNA. Conformational changes in SRP19 upon RNA binding were monitored using single-fluorophore experiments using 5 or 10 nM protein labeled with Alexa 488 or BODIPY-FL and varying concentrations of the LS RNA. Fluorescence intensity change over time was fit to a single exponential equation for pseudo first order kinetics. Second order rate constants were calculated from the slope of the line obtained by plotting the observed rate versus RNA concentration. SRP54 binding to the preformed SRP19-RNA complex was monitored using 20 nM fluorescently labeled SRP19-RNA complex and the change in fluorescence intensity as a function of time was fit to a second order rate equation : Observed fluorescence = $A[(\exp(kc_1t)-(\exp(kc_2t))(c_1c_2)/(c_1\exp(kc_1t)-c_2(\exp(kc_2t)] + b$, where k is the second-order rate constant, c_1 and c_2 are the initial concentrations of SRP54 and the SRP19-RNA complex, A is the amplitude of the fluorescence change and b is the initial fluorescence of the pre-formed SRP19-RNA complex. For experiments comparing native versus non-compartmentalized assembly, protein concentrations are given in Figures 3.8 B,C and the RNA concentration was twice that of the proteins.

3.3 Results

3.3.1 Strategy for monitoring assembly of SRP19 with the SRP RNA

Free SRP19 is a natively unstructured protein. Upon binding to the SRP RNA, SRP19 spans three structural motifs, a small globular core domain and two RNA binding loops that extend out from the core (Figure 3.1A) (*10, 15*). Assembly-induced conformational changes in each motif were monitored by attaching an environmentally sensitive fluorophore at four sites in SRP19. Each of the four positions is solvent accessible in both the SRP19-SRP RNA binary and the SRP19-SRP54-SRP RNA ternary complexes (*10, 15*). Fluorophores were placed individually in each of the two RNA binding loops (positions 31 and 72) and in the core domain (positions 93 and 106) (Figure 3.1A). Figure 3.1B is the SDS-PAGE of free and Alexa 488 derivatized SRP19 variants. The derivatized SRP19 variants moved slightly slower that free proteins in the gel. Control experiments showed that RNA binding affinities for each fluorophore-derivatized SRP19 were within 3-fold of unlabeled wild type SRP19 protein (see Materials and methods). Additionally, previous site-directed cleavage experiments performed with Fe(II)-BABE molecule attached to each of these four SRP19 structural sites showed that derivatization at these SRP19 positions has no perceptible effect on the structure of the SRP19-RNA complex.

Conformational changes specific to each position were monitored by either of two approaches. RNA-protein assembly monitored using fluorescence resonance energy transfer (FRET). Energy transfer occurred between a donor Alexa 488 fluorophore tethered to SRP19 and an acceptor Alexa 555 fluorophore tethered to the large subunit of the SRP RNA (LS RNA) via a hybridized DNA oligo (Alexa 555-LS RNA) (Figure 3.2A). Control experiments

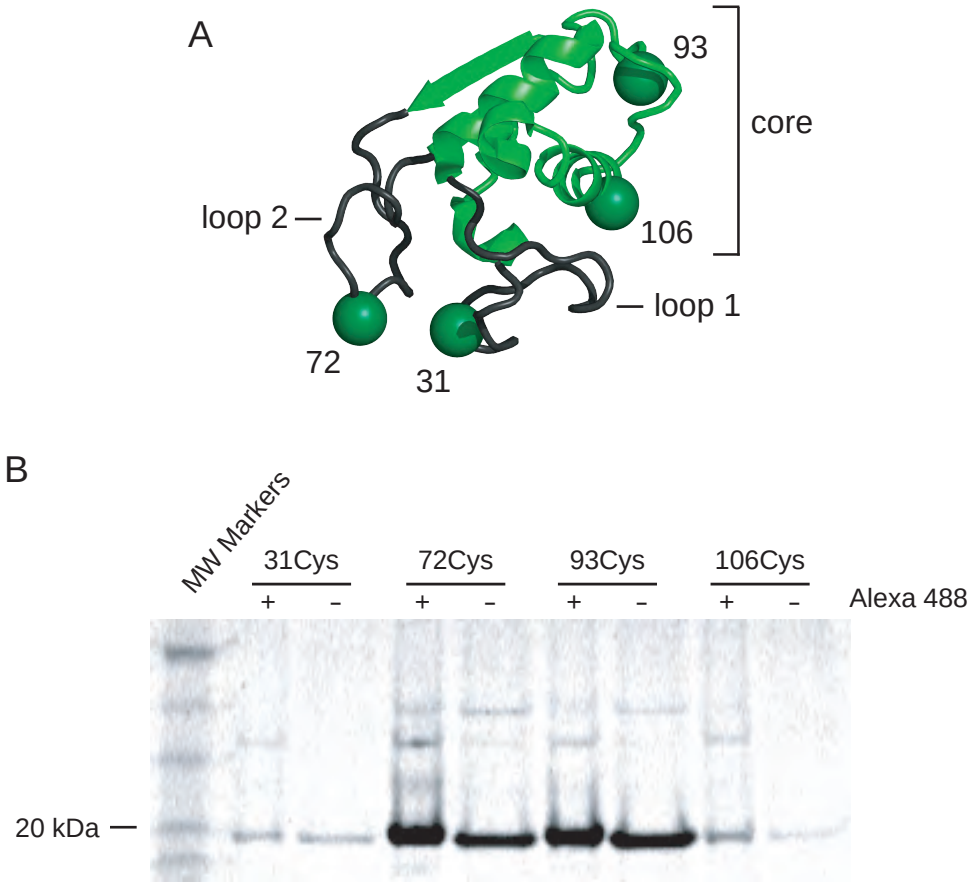

Figure 3.1. Site-specific labeling of SRP19 by environmentally sensitive Alexa 488 or BODIPY-FL fluorophore. (A) SRP19 structural motifs when bound to the SRP RNA. SRP core is green and the two RNA binding loops are gray. Sites of fluorophore attachment are shown as spheres. (B) SDS-PAGE of free and Alexa 488-derivatized SRP19 variants.

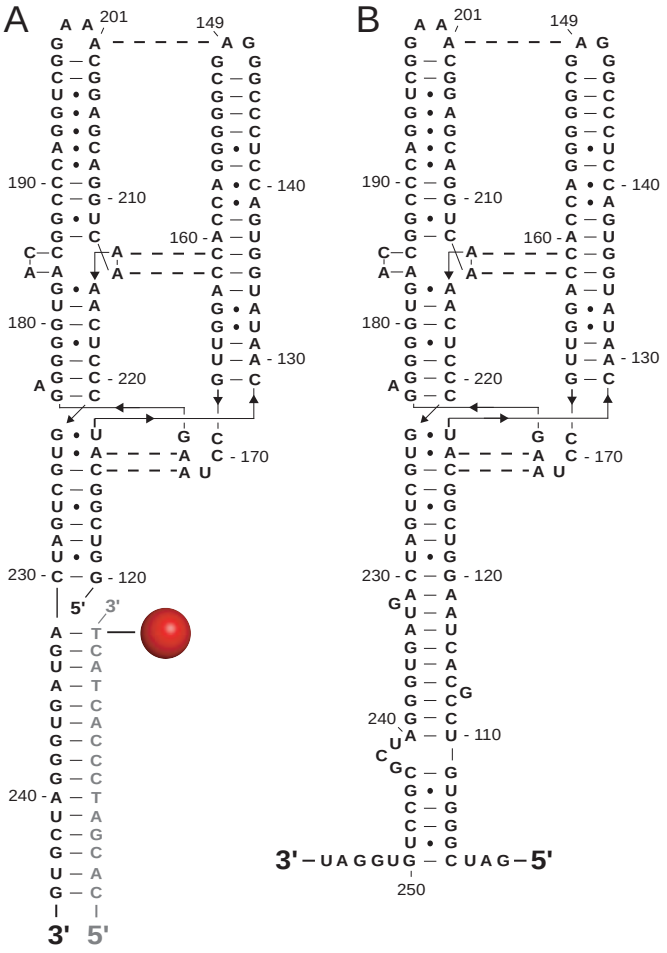

Figure 3.2. The large subunit SRP RNA (LS RNA). (A) Alexa 555 (red sphere) derivatized RNA:DNA hybrid construct. RNA and DNA are shown in black and gray, respectively. (B) LS RNA.

showed that SRP19 binding to the Alexa 555-LS RNA is indistinguishable to that of the underivatized LS RNA. In the second approach, SRP19 assembly with the SRP RNA was monitored directly in single fluorophore experiments using the environmentally sensitive fluorophores Alexa 488 or BODIPY-FL tethered to one of the four SRP19 labeling sites. Assembly of SRP54 with the SRP19-RNA complex could also be monitored as the effect that SRP54 binding has on the environmentally sensitive SRP19-tethered fluorophores.

3.3.2 FRET based analysis of SRP assembly

Assembly of the SRP19-RNA binary and the SRP19-SRP54-RNA ternary complexes were initially monitored as illustrated in Figure 3.3A. In this experiment Alexa 488 was both the FRET donor and also an environmentally sensitive fluorophore. Thus, RNA binding and subsequent conformational changes in SRP19 were detected both as the initial change in the resonance energy transfer efficiency to the RNA-tethered Alexa 555 acceptor fluorophore and as the local change in donor fluorophore environment (Figure 3.3A).

When SRP19, labeled at position 31, was added to the Alexa 555-LS RNA, a clear burst phase was observed in which the donor emission intensity was partially quenched followed by a well-resolved slow phase during which the emission intensity decreased further (phases 1 and 2 in the green trace in Figure 3.3B). This change in fluorescence was specific to SRP19-RNA interactions because the emission of a free reference fluorophore (Alexa 647) present in the solution remained unchanged over the course of the experiment (gray trace in Figure 3.3B). Similar overall behavior was observed when assembly was monitored using SRP19 labeled at position 72. Fluorescence emission initially decreased in a rapid burst phase followed by a well-resolved slow phase in which the fluorescence emission

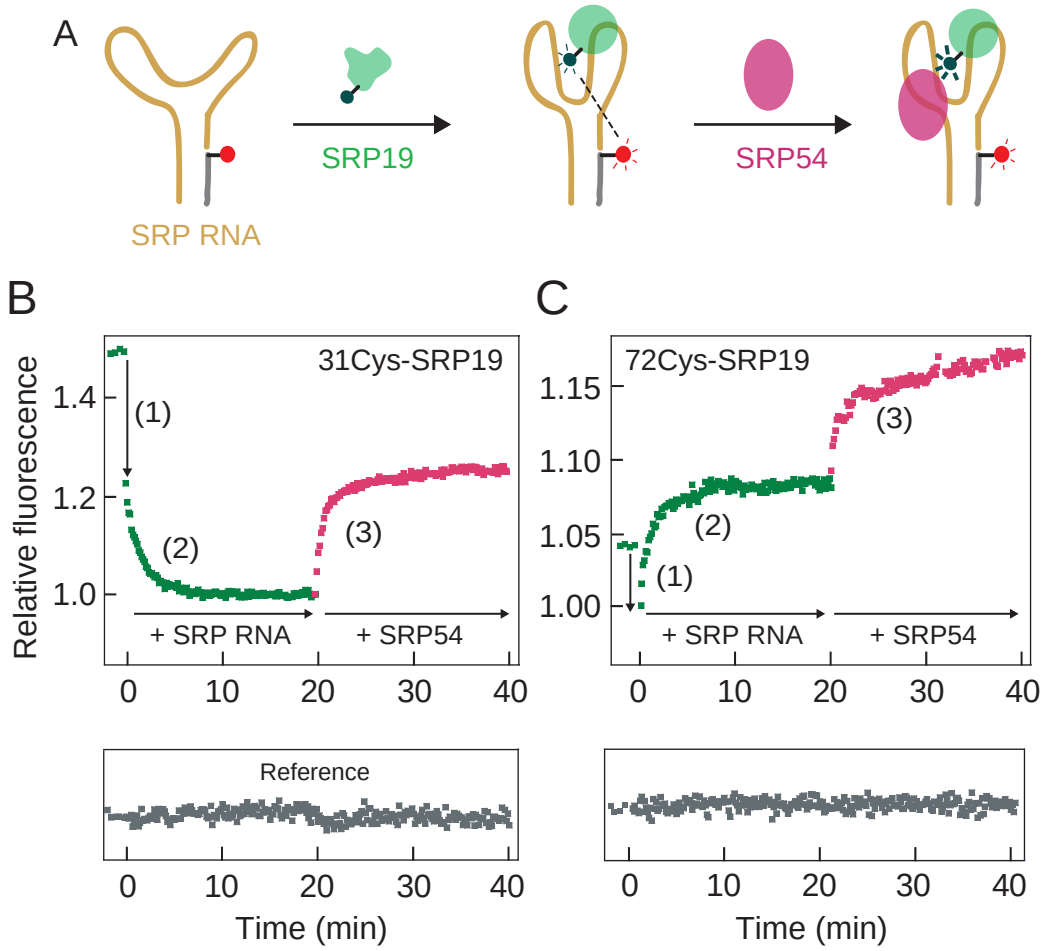

Figure 3.3. FRET-based analysis of SRP assembly. (A) Scheme for monitoring SRP assembly using Alexa 488-derivatized SRP19 (green) and the Alexa 555-LS RNA (yellow and gray). SRP54 (purple) binding is detected by its affect on the SRP19-RNA complex. (B, C) Three distinct assembly steps detected during native SRP19-SRP54-SRP RNA ternary complex formation. (1) A rapid burst phase quenching of fluorescence during initial SRP19-RNA assembly (green). (2) Well-resolved increase or decrease in fluorescence emission intensity as the SRP19-RNA complex matures to the native structure (green). (3) Increase in fluorescence intensity due to SRP54 binding to the preformed SRP19-RNA complex (purple). Free Alexa 647 reference fluorophore is gray.

intensity increased (green trace, Figure 3.3C.). These data indicate that both RNA-binding loops in SRP19 assemble with the LS RNA in at least two well-resolved steps.

Assembly of SRP54 with the preformed SRP19-RNA complex was monitored as the effect that SRP54 binding has on emission of the fluorophore attached to SRP19 (Figure 3.3A). Addition of SRP54 to a SRP19-RNA complex, labeled at either SRP19 position 31 or 72, yielded a clear increase in fluorescence emission intensity due to the perturbation of the local fluorophore environment upon SRP54 binding (purple traces in Figures 3.3B and C).

3.3.3 Burst phase of SRP19-RNA assembly corresponds to Encounter complex formation

To assign the binding event that corresponds to the rapid burst phase change in fluorescence for SRP19, labeled at either position 31 or 72, assembly was carried out using an A149U mutant RNA. Nucleotides A149 and A201 form a non-canonical base pair that links helices 6 and 8 in the SRP RNA (Figure 3.4A) (*10, 15*). SRP19 forms a labile Encounter complex with the A149U mutant RNA but cannot assemble beyond this step to form the native SRP19-RNA complex (*9*).

SRP19 binding to the A149U mutant RNA proceeded via a rapid burst phase change in fluorescence whose magnitude was comparable to that observed for the native sequence RNA (Figure 3.4B,C). In contrast, neither of the fluorescently labeled SRP19 proteins showed the second, slow, phase characteristic of assembly with the native sequence RNA (compare open and solid symbols in Figure 3.4B,C). It was thus inferred that the burst phase corresponds to rapid formation of an Encounter complex between SRP19 and the SRP RNA; whereas, the second, slower phase (visualized in Figures 3.3B,C) corresponds to slow

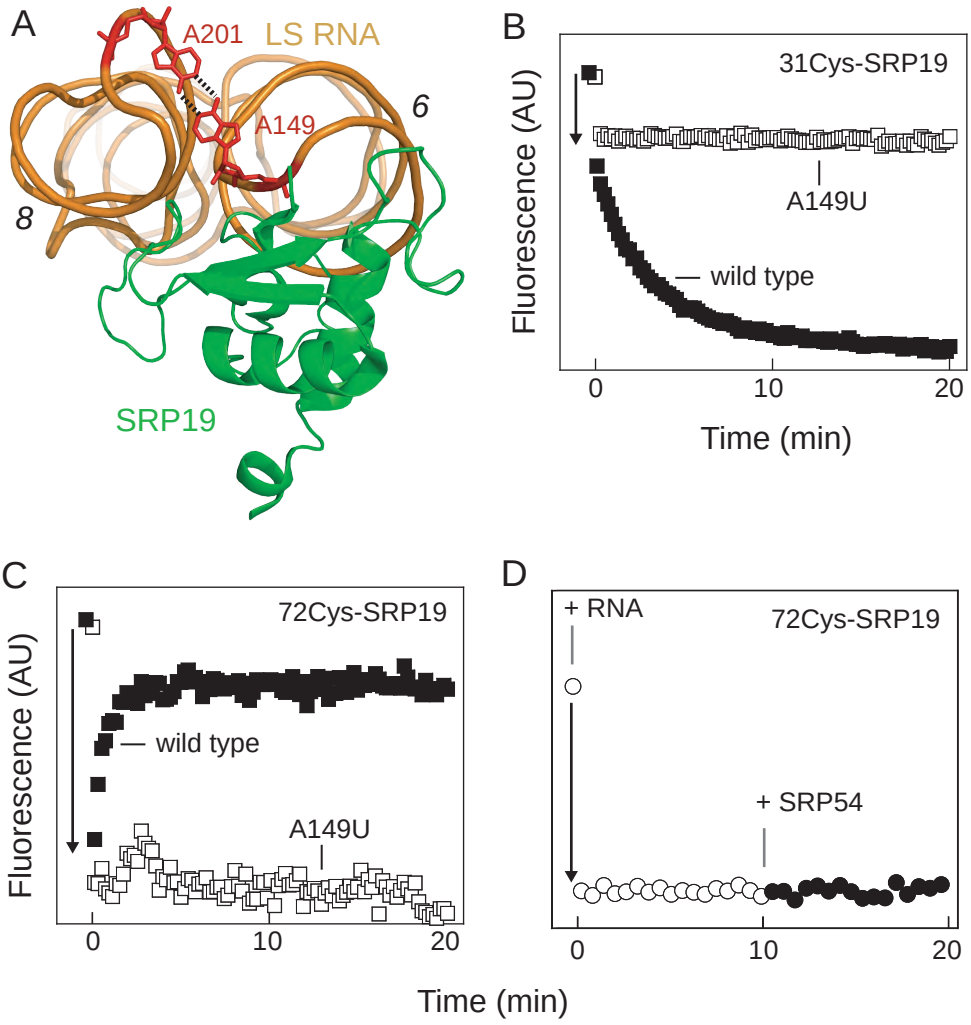

Figure 3.4. Burst phase assembly step corresponds to Encounter complex formation between SRP19 and the RNA. (A) The non-canonical base paring between A149 and A201 in the RNA. (B,C) SRP19-RNA assembly was monitored for the native sequence RNA or an A149U mutant that cannot form native RNA-RNA interactions (solid and open symbols, respectively). Arrows indicate burst phases observed with both RNAs. (D) Addition of SRP54 has no effect on the Encounter complex formed between SRP19 and the A149U RNA.

conformational rearrangements in the nascent SRP19-RNA complex that ultimately requires formation of the native RNA tertiary interaction between nucleotides A149 and A201.

Next, interaction between SRP54 and the SRP19-RNA Encounter complex was monitored. A stalled SRP19-RNA Encounter complex intermediate was first formed using the A149U mutant RNA and SRP19 derivatized at position 72. As expected, the burst phase fluorescence change upon formation of the initial SRP19-RNA complex was observed (open circles, Figure 3.4D). When SRP54 was added to this complex, no additional fluorescence change occurred (solid symbols, Figure 3.4D). These results contrast strongly with the ability of SRP54 to induce conformational changes in the native RNA-SRP19 complex (Figure 3.3C). It is thus inferred that SRP54 does not bind the Encounter complex intermediate.

3.3.4 SRP19 loop and core structures bind the SRP RNA via distinct mechanisms

SRP19 is comprised of distinct core and extended loop motifs (Figure 3.1A). Local conformational changes specific to the two RNA binding loops (positions 31 and 72) and to the SRP19 core domain (positions 93 and 106) were monitored using single fluorophore experiments (Figure 3.5A). RNA binding caused an increase in fluorescence emission efficiency for SRP19 proteins labeled with Alexa 488 at positions 72, 93 and 106 and a decrease for the protein labeled with Alexa 488 at position 31 (Figure 3.5B).

Strikingly different time-resolved behavior was observed depending on where the fluorophore was tethered to SRP19. When the fluorophore was linked to either of the RNA-binding loops in SRP19, the observed change in fluorescence intensity was 10-fold faster than when attached to the SRP19 core (compare open and solid symbols, Figure 3.5B).

Local assembly at each SRP19 motif was characterized by following the rate of change in fluorescence intensity as a function of RNA concentration. For all four Alexa 488-

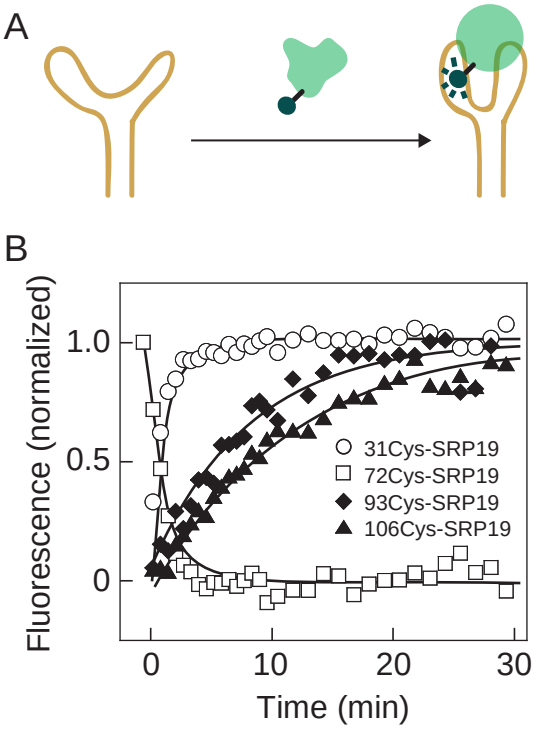

Figure 3.5. Conformational rearrangements at distinct SRP19 structural motifs during RNP assembly. (A) Scheme for monitoring SRP19-RNA assembly using single fluorophore experiments. (B) Fluorescence-detected assembly at the RNA-binding loops (open symbols) proceeds significantly faster than assembly of the SRP19 core domain (solid symbols).

labeled SRP19 proteins, rates increased with RNA concentration (Figure 3.6). SRP19 derivatized at positions 31, 93 and 106 showed good linear behavior in rate versus RNA concentration plots: the slopes of these lines yield the second-order rate constants for complex formation (squares, Figures 3.6A,C,D).

In contrast, SRP19 derivatized at position 72 exhibited a distinctive behavior. At RNA concentrations below 100 nM, the observed rate increased with increasing RNA concentration, as expected for a single rate-limiting binding step (squares, Figure 3.6B). However, at RNA concentrations above 100 nM, the apparent rate of complex formation became independent of concentration and leveled off at 0.9 min^{-1} (solid line, Figure 3.6B).

These distinctive kinetic behaviors are independent of the nature of the reporter fluorophore. The SRP19 variants labeled at positions 72 and 106 were also monitored using the BODIPY-FL fluorophore, which is chemically and sterically dissimilar to Alexa 488. The distinctive slow and fast time-resolved behaviors were identical as detected by either fluorophore (compare circles and squares, Figures 3.6B,D).

These experiments illustrate two distinctive features for assembly of the SRP19-RNA complex. First, second order rate constants vary by an order of magnitude and fall into two classes. SRP19 derivatized at either of the two RNA binding loops (positions 31 and 72) have similar second-order rate constants (2-8 $\times 10^6$ $M^{-1}min^{-1}$). SRP19 variants derivatized in the core (positions 93 and 106) also have similar rate constants (3-5 $\times 10^5$ $M^{-1}min^{-1}$) that are an order of magnitude slower than those observed at the RNA-binding loops. Second, the SRP19 variant derivatized at position 72 has a distinctive biphasic kinetic behavior such that a concentration-independent process with rate constant 0.9 min^{-1} limits assembly in the vicinity of RNA binding loop 2.

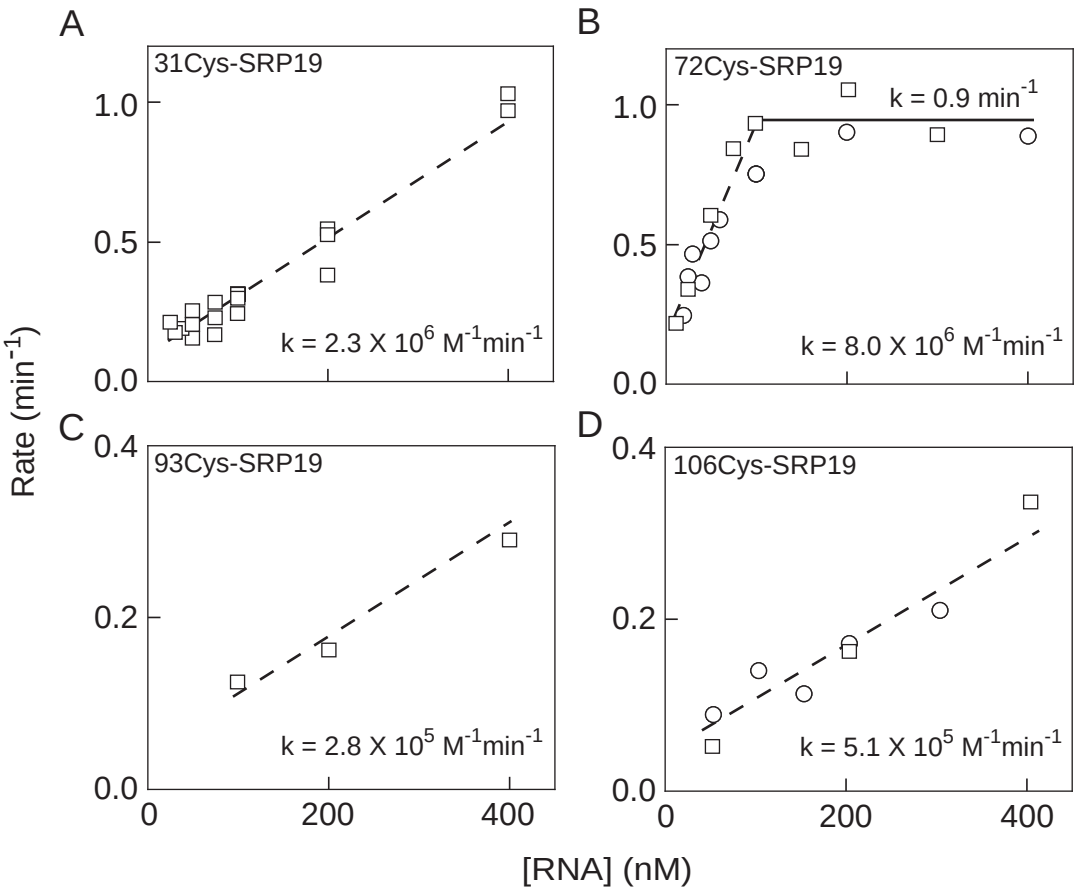

Figure 3.6. SRP19 structural motifs assemble with the RNA via distinct mechanisms. (A-D) Rate of change in fluorescence intensity as a function of RNA concentration for SRP19 variants. Slopes (dashed lines) yield second order rate constants for assembly as detected in distinctive SRP19 loop and core structural motifs. Most experiments were performed with Alexa 488-labeled SRP19 (squares). For the 72Cys and 106Cys variants, assembly was also monitored using the BODIBY-FL fluorophore (circles).

These experiments support a complex three-step mechanism for assembly of SRP19 with the SRP RNA. Free RNA and protein rapidly interact to form the Encounter complex. Encounter complex formation is observed directly as the fast phase (1) in FRET-based assembly experiments (Figure 3.3). This step is followed by two kinetically separable concentration-*dependent* conformational changes to form a stable intermediate complex. In these steps, the RNA binding loops in SRP19 undergo RNA induced conformational change more rapidly than does the core domain (Figure 3.5). Finally, regions near loop 2 participate in an additional concentration-*independent* structural rearrangement step that converts the stable complex into the native SRP19-RNA complex (Figure 3.6B).

3.3.5 Assembly of SRP54 with the preformed SRP19-RNA complex

Assembly of SRP54 with the preformed SRP19-LS RNA complex was monitored by the effect that SRP54 binding had on an environmentally sensitive fluorophore attached to SRP19. These experiments were similar to those described in Figure 3.3A, except that only SRP19 was fluorescently labeled. For SRP19 variants derivatized at either position 31 or 72, fluorescence emission intensity increased upon SRP54 binding (Figure 3.7A,B). Notably, SRP54 binds to the preformed SRP19-RNA complex with a K_d = 12 nM (Figure 2.5). Here, SRP54 concentrations ranging from 15-200 nM were used. Thus, at low SRP54 concentration formation of the SRP ternary complex was not at its saturation limit and increased with concentration of SRP54. This phenomenon was reflected as variations in the magnitude of change in fluorescence intensity for different SRP54 concentrations. The rate of increase in fluorescence was monitored as a function of SRP54 concentration (Figures 3.7A,B) and fit to a second order rate equation. Over a broad range of SRP54 concentrations, second order rate constants were identical, at 1.1×10^7 M^{-1} min^{-1} (Figures 3.7C,D),

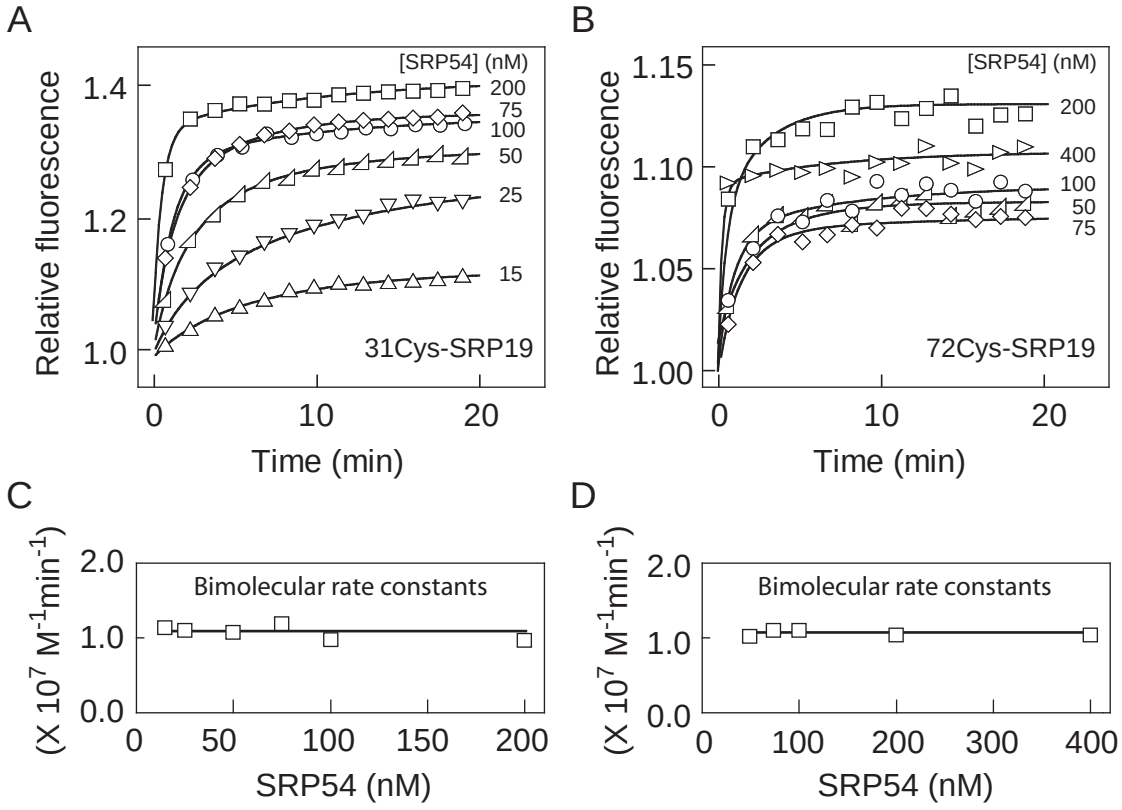

Figure 3.7. One step assembly of SRP54 to the pre-formed SRP19-RNA complex. (A,B) The second order rate constant k_3 for SRP54 binding to the preformed SRP19-RNA complex was obtained by fitting change in fluorescence intensity over time to a second order rate equation: observed fluorescence = $A[(\exp(k_3c_1t)-(\exp(k_3c_2t))(c_1c_2)/(c_1\exp(k_3c_1t)-c_2(\exp(k_3c_2t)] + b$; c_1 and c_2 are the initial concentrations of SRP54 and the SRP19-RNA complex, respectively; A and b are the magnitude of the fluorescence change and the initial fluorescence of the pre-formed SRP19-RNA complex, respectively. (C,D) All SRP54 concentrations yielded identical second order rate constants.

independent on the site of derivatization in SRP19. SRP54 thus binds in a single kinetically significant step.

3.3.6 Concentration dependence of non-compartmentalized ternary complex formation

As described above, if SRP19 and SRP54 assemble with the RNA simultaneously, these three components interact to form the non-compartmentalized complex whose structure is significantly different from the native complex (Figure 2.13). Single fluorophore experiments were used to characterize the kinetic step that gates whether SRP54 assembles to form the native or non-compartmentalized complex (Figure 3.8A,D).

Formation of the native complex was followed by sequential addition of SRP19 and SRP54 (green and purple traces, Figures 3.8B,C). This is the SRP54-late pathway. As monitored using the 31Cys-SRP19 protein, fluorescence emission intensity decreased as free SRP19 bound to the RNA. The rate of binding increased as the protein concentration was increased from 50 to 200 nM (green traces in Figure 3.8B). Fluorescence intensity then increased upon subsequent addition of SRP54. The rate of SRP54 binding also increased with protein concentration, as expected (purple traces in Figure 3.8B). These data are consistent with the SRP19 and SRP54 binding experiments outlined in Figures 3.6A and 3.7A, respectively.

Assembly of the (non-native) non-compartmentalized ternary complex was then monitored by adding SRP54 prior to adding SRP19. This is the SRP54-early pathway (black traces in Figure 3.8B). These experiments were performed under the identical component concentrations used to monitor native complex formation. Thus, the experiments represented by the green and purple versus black traces (Figures 3.8A,B) differed only in the order in

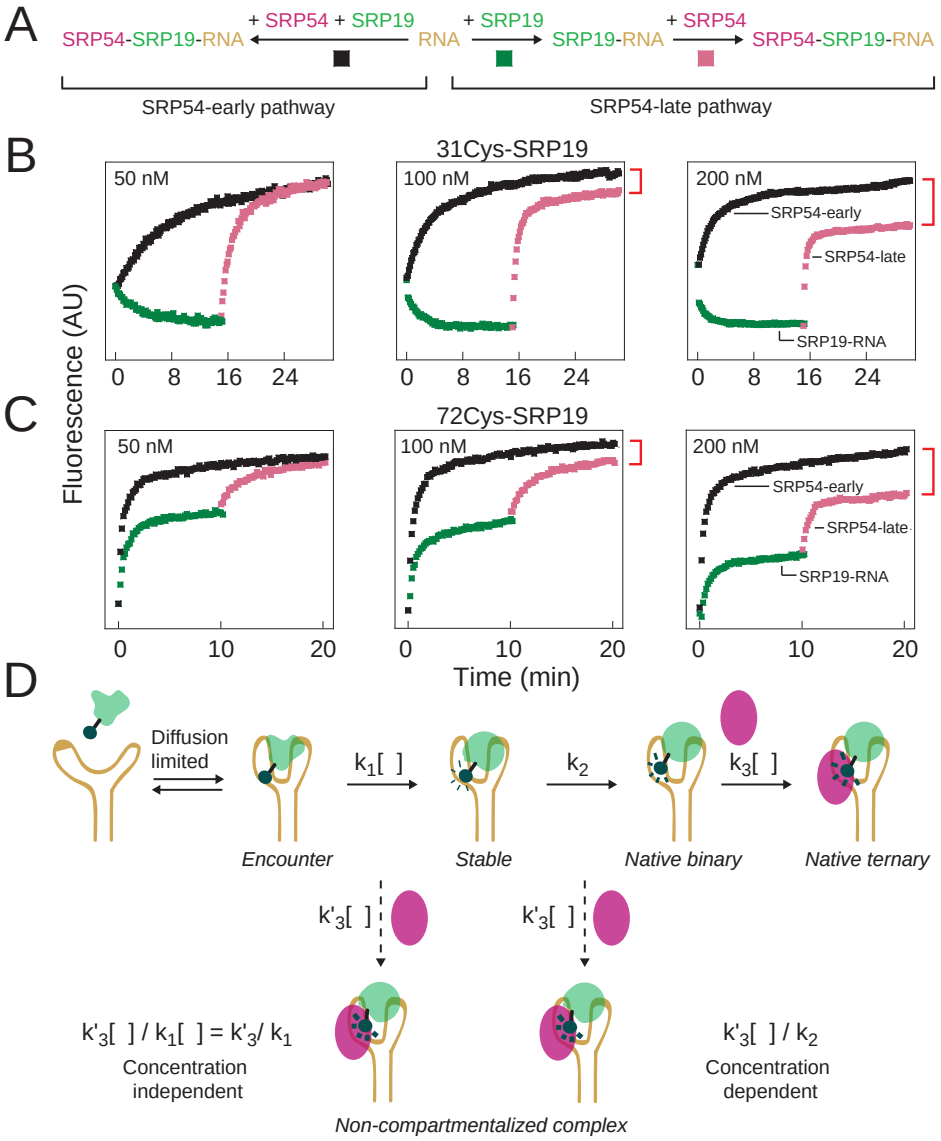

Figure 3.8. The extent of non-compartmentalized complex formation is concentration dependent. (A) Scheme for monitoring native vs. non-compartmentalized assembly using single fluorophore experiments. Native assembly (the SRP54-late pathway) involves ordered binding by SRP19 (green traces) and SRP54 (purple traces). For non-compartmentalized assembly (the SRP54-early pathway), both proteins assemble simultaneously (black traces). (B,C) Visualization of native and non-compartmentalized ternary complex formation using single fluorophore experiments. Ratios of SRP19, SRP54 and RNA components were held constant at 1:1:2 in all experiments; protein concentrations are given for each panel. Non-compartmentalized complex formation is reported directly as the intensity difference between purple (native) and black (non-compartmentalized) traces. (D) Expected concentration dependence for SRP54 binding post-Encounter versus post-Stable complex formation. k_1 is a compound rate constant reflecting formation of the Stable complex via the kinetically linked Encounter complex. Dashed arrows show putative, concentration-dependent ($k'_3[\ ]$), steps for SRP54-mediated misassembly.

which SRP components interact but not in the identity or amounts of SRP19, SRP54 or SRP RNA.

Strikingly, when assembly was monitored for component concentrations of 200 nM, complexes formed via the SRP54-early pathway had significantly higher fluorescence than complexes formed via the SRP54-late pathway (compare the endpoints for purple and black traces in Figure 3.8B). This difference in fluorescence intensity directly reports formation of the non-compartmentalized complex via the SRP54-early pathway. A similar, but smaller, difference in fluorescence was observed at 100 nM protein concentrations; whereas, the difference disappeared when component concentrations were reduced to 50 nM (Figure 3.8B).

Next, comparable experiments with the 72-Cys SRP19 variant were performed. As expected, the rate of SRP19-RNA complex formation was concentration-independent (green traces, Figure 3.8C) because the conformational rearrangement involving loop 2 binding plateaus at 0.9 min^{-1} (recall Figure 3.6B). The rate of SRP54 binding increased with increasing SRP54 concentration, consistent with simple one-step assembly with the preformed SRP19-RNA complex (purple traces, Figure 3.8C). Similar to assembly as monitored at position 31, the fluorescence of the final 72Cys-complex was again strongly concentration dependent and the difference in fluorescence intensity in the final complexes was larger at 200 nM components than at 100 or 50 nM concentrations (compare purple and black traces in Figure 3.8C).

In summary, as monitored at either of two locations within SRP19, there exists a kinetic competition such that misassembly is specifically favored at high component

concentrations. As outlined under the Discussion, this concentration-dependent behavior provides strong evidence regarding the physical step that gates misassembly.

3.4 Discussion

3.4.1 Assembly of the SRP19-RNA complex via distinct folding stages for the loop and core domains

Physical model for the alternating interactions that lead to the native SRP19-RNA complex derived from experiments described above is shown in the first four panels of Figure 3.9. Both SRP19 and the SRP RNA are in non-native conformations prior to forming a specific ribonucleoprotein complex. The SRP RNA contains significant base pairing interactions; whereas, free SRP19 exists in an unstructured coil conformation.

SRP19 and the RNA initially interact in a rapid, approximately diffusion-limited, step to form an Encounter complex. This step occurs with similar, very rapid, kinetics for both the native sequence SRP RNA and a mutant (A149U) RNA that is incapable of maturing to the native complex (Figure 3.4B,C). Encounter complex largely reflects a fast forming heterogeneous electrostatic interaction between the RNA and SRP19.

Further assembly from the Encounter complex involves a series of complex SRP19 folding steps to form the Stable intermediate (Figure 3.9). SRP19 loops 1 and 2 undergo, RNA-induced, second order conformational changes with rate constants that are an order of magnitude faster than folding of the SRP19 core domain (Figures 3.5B and 3.6). Folding of both the core and loop motifs are concentration-dependent (below 100 nM) even though they follow formation of the Encounter complex. This observation suggests that the Encounter complex establishes a rapid pre-equilibrium with the free RNA and SRP19.

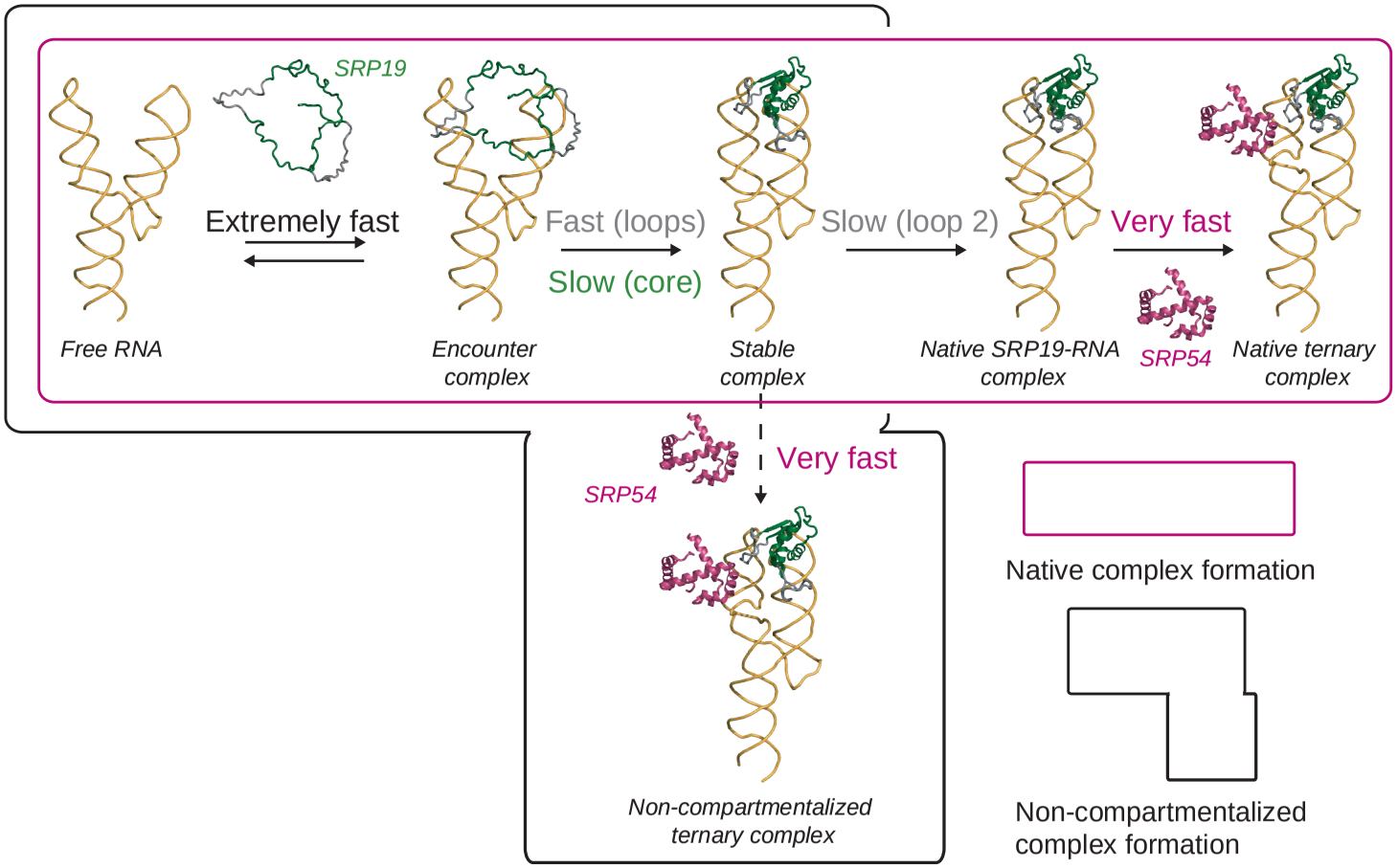

Figure 3.9. Mechanisms for native and non-compartmentalized SRP assembly. Native and non-compartmentalized complexes are gated at the Stable complex intermediate.

An additional SRP19 folding step is revealed by the concentration-independent folding behavior of loop 2. Below 100 nM, folding at loop 2 shows the same simple concentration-dependent behavior as loop 1 (Figures 3.6A,B); whereas, at higher concentrations, the rate of the conformational change associated with loop 2 plateaus at 0.9 min^{-1}. Thus, a *first order* conformational rearrangement in the still-immature RNA-protein complex limits overall assembly at SRP19 loop 2 (Figure 3.9). Completion of the first order rearrangement of loop 2 yields the Native SRP19-RNA complex.

3.4.2 The three-fold protein-RNA interface involving SRP19 loop 2 gates native assembly of the SRP ternary complex

SRP54 does not bind stably to the free SRP RNA (*16, 17*). Therefore, SRP54-mediated misassembly via the SRP54-early pathway must involve SRP54 binding to an intermediate SRP19-RNA complex. The two candidate classes of intermediate complexes could be either (i) after formation of the Encounter complex or (ii) after formation of the Stable intermediate complex: prior to maturation of the loop 2-RNA interaction (illustrated by dashed arrows in Figure 3.8D).

Two independent experiments support a model in which SRP54 binds after formation of the Stable complex. First, direct binding experiments show that SRP54 does not modulate the fluorescence of the complex formed between SRP19 and the A149U RNA, which is trapped at the Encounter complex stage (Figure 3.4D). Second, formation of the non-compartmentalized complex is strongly dependent on the total concentration of SRP protein and RNA components (Figures 3.8B,C). This is exactly the concentration dependence expected if SRP54-mediated misassembly occurs *after* Stable complex formation but not if SRP54 binds after Encounter complex formation (summarized in Figure 3.8D). The

governing kinetic competition involves both concentration–independent (k_2) and –dependent ($k'_3[\ ]$) steps such that the fraction of non-compartmentalized complex formed ($k'_3[\ ]/k_2$) increases at higher SRP54 concentrations, if SRP54 binds after the Stable complex forms.

Folding of Loop 2, which occurs after formation of the Stable SRP19-RNA intermediate, has exactly the correct slow concentration-independent behavior required to gate native versus non-compartmentalized assembly. SRP19 loop 2 is packed in a cleft-like interface formed by SRP54 and helix 6 of the RNA (Figure 2.12 A) (*10*). Thus, loop 2 both exhibits an intrinsically slow local folding behavior and also lies in a highly constrained three-fold interface in the native particle. These observations support a model in which formation of the non-compartmentalized complex involves rapid RNA binding by SRP54 to a nearly native SRP19-RNA interface but in which folding of loop 2 is still incomplete (Figure 3.9). Early binding by SRP54 then results in a conformation in which loop 2 lies outside the correct three-fold interface and further insertion of this loop into its native interaction cleft is kinetically unfavorable.

3.4.3 SRP54-RNA interaction alters the SRP19 folding energy landscape

SRP19 has an almost identical structure in both the SRP19-RNA19 binary and native SRP19-SRP54-RNA20 ternary complexes. SRP54 thus has no role in the native folding of SRP19. In contrast, SRP54-induced misfolding of SRP19 indicates that interactions between SRP54 and the RNA alter the folding energy landscape for SRP19. In the absence of SRP54, SRP19 folds to reach its global energy minimum in a landscape whose most important features include formation of the Encounter and Native complexes and a single major intermediate, the Stable complex (Figure 3.10A). SRP54 binding to the preformed SRP19-

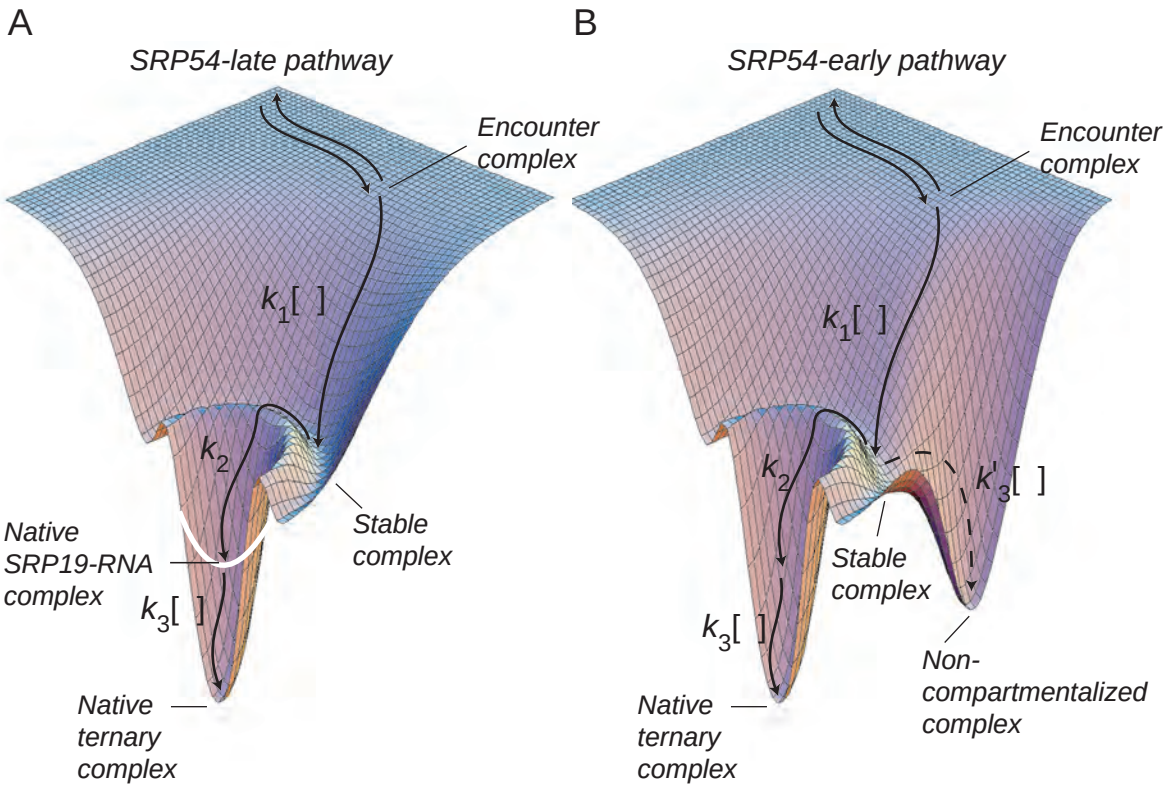

Figure 3.10. Folding energy landscapes for SRP19 during SRP ternary complex formation via SRP54-late (A) and SRP54-early (B) pathways. Landscapes were constructed by plotting linear combination of multiple three-dimensional Gaussian distributions in *Mathematica* (Wolfarm).

RNA complex does not significantly alter the SRP19-RNA complex but further stabilizes it, creating a deeper well in the landscape (Figure 3.10A).

The untimely presence of SRP54 alters the folding landscape for SRP19 to create a second, deep, low energy minimum corresponding to the non-compartmentalized complex (Figure 3.10B). Non-compartmentalized complex formation is concentration dependent indicating that the alternative pathway is kinetically driven and leads to a local rather than a new global minimum relative to the native ternary complex.

3.4.4 Broad implications for multi-component RNP assembly reactions

A simple three-component RNP, derived from the mammalian signal recognition particle, has the ability to form a stable alternative, non-native complex. The native and non-compartmentalized complexes differ only in the order by which the three components assemble. Telomerase p65-TERT-RNA ternary complex has recently been found to form similar order-of-interaction driven misassembled complex (*18*). The structural requirements for this order-of-interaction driven misassembly are very modest. Alternative complex formation requires only that the three components communicate structurally and that a portion of one binary interface be modulated by a third component. In the SRP example, structural communication involves a direct three-fold interface, but indirect interactions would suffice, as well.

Evidence that RNP assembly requires spatial or temporal regulation is currently circumstantial, but suggestive. Like the SRP, several other cellular RNPs have multi-site assembly phases involving transit through nucleolar and Cajal body compartments (*19, 20*). Examples in which spatial control potentially facilitates RNP assembly include snRNPs, spliceosomal RNPs and telomerase. A second strategy for regulated RNP assembly would be

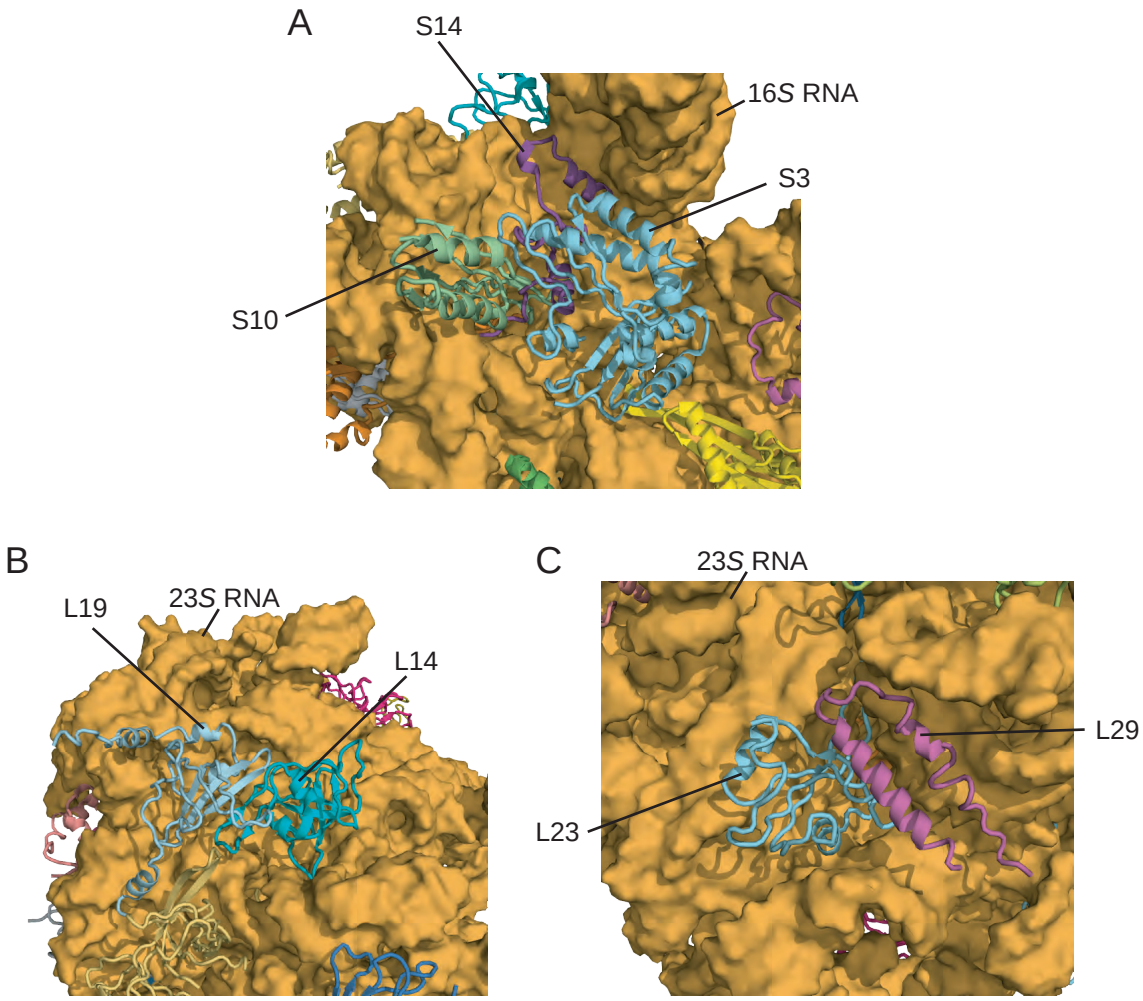

Figure 3.11. Structural specificity in the bacterial ribosomal subunits that likely require preferred temporal assembly phases. Structural models are based on recently published crystal structure of the bacterial ribosome *(20)*. (A) S3, S10, S14 proteins and 16*S* RNA in the small subunit. (B,C) L19, L14 and 23*S* RNA, and L23, L29 and 23*S* RNA in the large subunit, respectively.

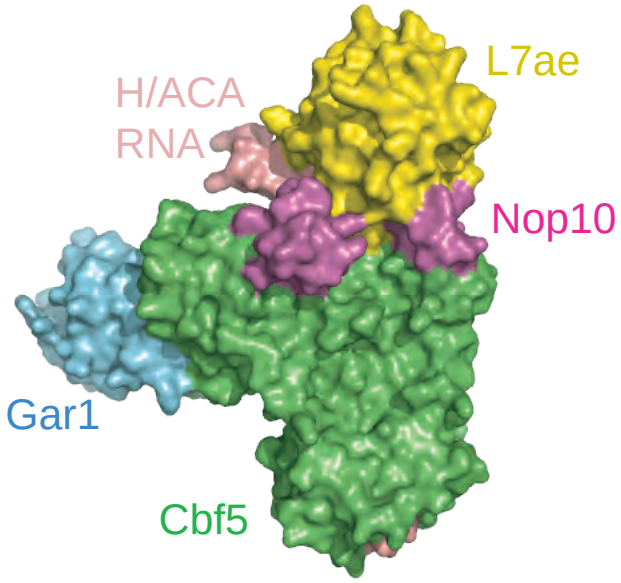

Figure 3.12. Structural specificity in the *archaeal* H/ACA Box RNP that likely requires preferred temporal assembly phases *(23)*.

to impart structural specificity through preferred temporal assembly phases. In the small subunit of the bacterial ribosome (*21*), three proteins, S3, S10 and S14, and the 3'-domain of 16*S* RNA form an intimate four-fold interface that appears to physically require that proteins S10 and S14 assemble with the RNA prior to protein S3 (Figure 3.11A). Consistent with this structural view, S10 assembles with 16*S* RNA more rapidly than does S3 (*22, 23*). In contrast, S3 and S14 bind at comparable rates (*23*). One can speculate that premature RNA binding by S3 has the potential to lead to RNP misassembly at this protein-RNA interface by interfering with correct S14-RNA assembly. Multi-fold interfaces exist with the potential to misassemble in the large subunit of the bacterial ribosome (*21*), including those formed by L14, L19 and 23*S* RNA and by L23, L29 and 23*S* RNA (Figures 3.11B and C, respectively), and in the archaeal H/ACA complex formed by L7ae, Cbf5, Nop10, Gar1 and the H/ACA RNA (Figure 3.12) (*24*).

Given that multi-fold interfaces are common in RNP complexes, it can be proposed that avoiding formation of stable, but misassembled, complexes is of fundamental importance for the structural biogenesis of many RNPs. Mechanisms for regulating assembly, including preferred early and late assembly phases and cellular compartmentalization, may play critical regulatory roles in preventing order-of-interaction driven misassembly for many multi-component RNPs in the cell.

3.5 References

1. Weeks, K. M. (1997) Protein-facilitated RNA folding. *Curr. Opin. Struct. Biol. 7,* 336-342.

2. Williamson, J. R. (2000) Induced fit in RNA-protein recognition. *Nat. Struct. Biol. 10*, 834-837.

3. Agalarov, S. C., Prasad, G. S., Funke, P. M., Stout, C. D., and Williamson, J. R. (2000) Structure of the S15, S6, S18-rRNA complex: Assembly of the 30S ribosome central domain. *Science 288*, 107-112.

4. Agalarov, S. C., and Williamson, J. R. (2000) A hierarchy of RNA subdomains in assembly of the central domain of the 30 S ribosomal subunit. *RNA 6*, 402-408.

5. Herschlag, D. (1995) RNA chaperones and the RNA folding problem. *J. Biol. Chem. 270*, 20871-20874.

6. Schroeder, R., Barta, A., and Semrad, K. (2004) Strategies for RNA folding and assembly. *Nat. Rev. Mol. Cell Biol. 5*, 908-919.

7. Dill, K. A., and Chan, H. S. (1997) From Levinthal to pathways to funnels. *Nat. Struct. Biol. 4*, 10-19.

8. Dobson, C. M. (2003) Protein folding and misfolding. *Nature 426*, 884-890.

9. Rose, M. A., and Weeks, K. M. (2001) Visualizing induced fit in early assembly of the human signal recognition particle. *Nat. Struct. Biol. 8*, 515-520.

10. Kuglstatter, A., Oubridge, C., and Nagai, K. (2002) Induced structural changes of 7SL RNA during the assembly of human signal recognition particle. *Nat. Struct. Biol. 9*, 740-744.

11. Jacobson, M. R., and Pederson, T. (1998) Localization of signal recognition particle RNA in the nucleolus of mammalian cells. *Proc. Natl. Acad. Sci. USA 95*, 7981-7986.

12. Politz, J. C., Yarovoi, S., Kilroy, S. M., Gowda, K., Zwieb, C., and Pederson, T. (2000) Signal recognition particle components in the nucleolus. *Proc. Natl. Acad. Sci. USA 97*, 55-60.

13. Ciufo, L. F., and Brown, J. D. (2000) Nuclear export of yeast signal recognition particle lacking Srp54p by the Xpo1p/Crm1p NES-dependent pathway. *Curr. Biol. 10*, 1256-1264.

14. Alavian, C. N., Politz, J. C. R., Lewandowski, L. B., Powers, C. M., and Pederson, T. (2004) Nuclear export of signal recognition particle RNA in mammalian cells. *Biochem. Biophys. Res. Commun. 313*, 351-355.

15. Oubridge, C., Kuglstatter, A., Jovine, L., and Nagai, K. (2002) Crystal Structure of SRP19 in complex with the S domain of SRP RNA and its implication for the assembly of the signal recognition particle. *Mol. Cell 9,* 1251-1261.

16. Romisch, K., Webb, J., Herz, J., Prehn, S., Frank, R., Vingron, M., and Dobberstein, B. (1989) Homology of 54K protein of signal-recognition particle, docking protein and two *E. coli* proteins with putative GTP-binding domains. *Nature 340*, 478-482.

17. Gowda, K., Chittenden, K., and Zwieb, C. (1997) Binding site of the M-domain of human protein SRP54 determined by systematic site-directed mutagenesis of signal recognition particle RNA. *Nucl. Acids Res. 25,* 388-394.

18. Stone, M. D., Mihalusova, M., O/'Connor, C. M., Prathapam, R., Collins, K., and Zhuang, X. (2007) Stepwise protein-mediated RNA folding directs assembly of telomerase ribonucleoprotein. *Nature* -, -.

19. Gerbi, S. A., Borovjagin, A. V., and Lange, T. S. (2003) The nucleolus: a site of ribonucleoprotein maturation. *Curr. Opin. Cell Biol. 15*, 318-325.

20. Matera, A. G., and Shpargel, K. B. (2006) Pumping RNA: nuclear bodybuilding along the RNP pipeline. *Curr. Opin. Cell Biol. 18,* 317-324.

21. Selmer, M., Dunham, C. M., Murphy, F. V. t., Weixlbaumer, A., Petry, S., Kelley, A. C., Weir, J. R., and Ramakrishnan, V. (2006) Structure of the 70S ribosome complexed with mRNA and tRNA. *Science 313*, 1935-42.

22. Held, W. A., Ballou, B., Mizushima, S., and Nomura, M. (1974) Assembly mapping of 30S ribosomal proteins from *Escherichia coli*. *J. Biol. Chem. 249,* 3103-3111.

23. Talkington, M. W., Siuzdak, G., and Williamson, J. R. (2005) An assembly landscape for the 30S ribosomal subunit. *Nature 438,* 628-632.

24. Li, L., and Ye, K. (2006) Crystal structure of an H/ACA box ribonucleoprotein particle. *Nature 443*, 302-307.

Chapter 4

Anti-cooperative Communication Between SRP19 and SRP68/72 in Assembly of the Signal Recognition Particle

4.1 Introduction

Among the six proteins in the mammalian signal recognition particle, SRP68 and SRP72 are the least well characterized. In high ionic strength media, both proteins are dissociated from the SRP as a stable heterodimer that can re-bind the SRP RNA independently of other SRP proteins (*1*, *2*). As individual proteins, one study concluded that SRP72 does not bind to the SRP RNA on its own but its assembly into SRP requires prebinding by SRP68 to the SRP RNA (*3*); whereas, a second study reported that SRP72 binds directly to the RNA (*4*). This study confirms that SRP72 has a strong but non-specific ability to bind the RNA. The SRP68/72 heterodimer is thought to act as a anchor between the S-domain and a hinge in the SRP RNA, allowing movement of the two SRP domains that may coordinate signal peptide recognition by the S-domain with elongation arrest activity by the *Alu* domain (*5*). Previous biochemical (*6*) and a recent cryo-electron microscopy (*5*) studies have suggested that SRP68/72 bind at the three-way junction involving RNA helices 5, 6 and 8 and at a conserved asymmetric loop at the end of the LS RNA. However, no nucleotide-resolution structural data specifying their precise binding sites are currently available for SRP68/SRP72.

This study shows that SRP68 binds at the three-way junction of helices 5, 6 and 8 on the opposite side of the RNA relative to where SRP19 binds. Despite these opposing interaction sites, SRP68 stabilizes an RNA conformation that is very similar to that induced by SRP19. Surprisingly, it has been found that this mutual stabilization of the parallel helical orientation is idiosyncratic such that prior RNA binding by SRP68/72 slows the binding by SRP19. Similarly, prebinding by SRP19 reduces the affinity of SRP68/72 for the SRP RNA.

Although SRP68 and SRP19 do not directly contact each other in the SRP, their

mutually anti-cooperative assembly may originate from structural tension caused by similar, but slightly out-of-phase RNA conformations induced by SRP19 and SRP68/72 binding.

4.2 Materials and methods

4.2.1 Expression and purification of recombinant SRP proteins

Cloning and expression of recombinant SRP68 and SRP72 were performed in collaboration with Prof. Howard M. Fried. C-terminally His_6-tagged SRP68 (the clone was a gift from Bernhard Dobberstein, University of Heidelberg) and N-terminally His_6-S-tagged SRP72 were expressed from cDNAs cloned into plasmids pET42b and pET30a (Novagen), respectively. Expression of SRP68 was induced with 0.8 mM IPTG for 5 h at 25 °C in *E. coli* strain BL21(DE3)STAR (Invitrogen) grown in Luria broth. SRP72 was expressed in BL21(DE3) (Novagen). Cells were pre-grown to saturation at 37 °C in 1.6% tryptone, 1% yeast extract, 0.5% NaCI, (2YT) containing 1% glucose. Pre-grown cells were diluted with three volumes of 2YT and incubated for 1 h at 37 °C whereupon an equal volume of ice-cold 2YT containing 4% ethanol was added with shaking at 17° C for 30 min, followed by protein induction by addition of IPTG (1.0 mM) for 5 h at 17° C. For both SRP68 and SRP72, cells were sonicated in 50 mM Tris-HCl (pH 7.5), 1.0 M LiCl, 5 mM 2-mercaptoethanol and 20 mM imidazole. Following centrifugation for 1 h at 225,000 × *g*, the lysate was applied to a Ni^{2+}-agarose column. Protein was eluted with 250 mM imidazole and dialyzed into 300 or 500 mM potassium acetate (pH 7.6), 25 mM HEPES-KOH (pH 7.5), 5 mM $MgCl_2$ and 5 mM 2-mercaptoethanol. SRP19 was expressed and purified as described (*7*). All protein concentrations were measured by UV absorption maxima 280 nm.

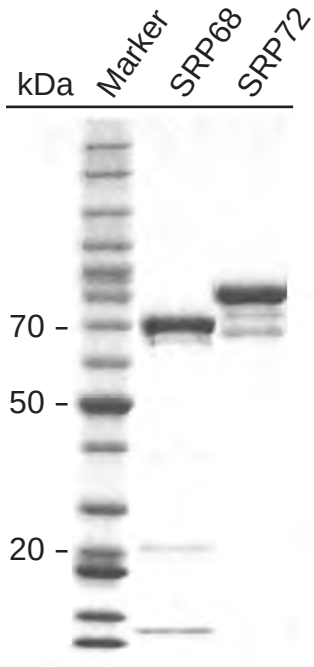

Figure 4.1. SDS-PAGE of recombinant SRP68 and SRP72.

4.2.2 Filter binding assays

Internally [^{32}-P]-labeled LS RNA was refolded by heating at 95 °C (1 min), snap-cooling at ice (1 min) and incubating at 60 °C (10 min) in the presence of RNA refolding buffer [300 or 500 mM potassium acetate (KOAc) (pH 7.6), 5 mM $MgCl_2$, 20 mM Hepes (pH 7.6), 0.01% (v/v) Triton], followed by slow cooling to room temperature (~ 40 min). Final concentration of the RNA was 0.1 nM. All protein binding reactions were performed at 25 °C in RNA refolding buffer supplemented with 1/5 volume of 300 mM NaCl, 50 mM sodium phosphate (pH 8.0), and 0.5 mg/mL BSA. For SRP68/72 binding with the SRP19-RNA complex (at 500 mM KOAc), 50 nM of SRP19 was added to the RNA 30 min prior to SRP68/72 addition. Samples were filtered rapidly through (top) nitrocellulose (Schleicher and Schuell) and (bottom) HyBond N^+ (Amersham) membranes, using a dot blot apparatus (Schleicher and Schuell) and quantified by phosphorimaging. Equilibrium dissociation constants (K_d) were obtained by fitting the 'fraction of RNA bound' to $K_d/(K_d + [protein])$.

4.2.3 Hydroxyl radical footprinting experiments

Footprinting experiments at high ionic strength condition were performed by Prof. Howard M. Fried. 50 nM of 5'-[^{32}P]-labeled refolded LS RNA was incubated with the appropriate SRP protein(s) in RNA refolding buffer. For low ionic strength (300 mM KOAc) experiments the final concentration of each SRP protein was 100 nM. For high ionic strength (500 mM KOAc) experiments SRP68 (800 nM), SRP72 (800 nM) or SRP68/72 (200, 400 and 800 nM) were used. Hydroxyl radical cleavage (25 °C, 1 h) was initiated by adding freshly prepared solutions (2 µl each) 50 mM DTT, 50 mM sodium ascorbate, 45 mM EDTA and 30 mM $[Fe(II)(NH_4)_2]SO_4$ to a 20 µl reaction. The reactions were quenched by adding 2 µl 2M thiourea, 2 µl 0.5 M EDTA and 20 µg proteinase K (37 °C, 30 min). RNA fragments

were resolved on 8-12% denaturing sequencing gels and quantified by phosphorimaging. Pymol (www.pymol.org) was used to visualize protein interaction sites in the context of an SRP19-RNA crystal structure (*8*).

4.2.4 SRP19-RNA assembly kinetics

Generation of SRP19 labeled with Alexa 488 at amino acid position 72 was performed as described in section 3.2.2. All experiments were performed at high ionic strength RNA refolding buffer supplemented with 1/5 vol of 300 mM NaCl, 50 mM sodium phosphate (pH 8.0) at 25 °C. Assembly of SRP19 with the free RNA or with the SRP68/72-RNA complexes were initiated by adding 100 µl refolded LS RNA (100 nM final) or preformed SRP68/72-RNA complex (100 nM final), respectively, to 400 µl Alexa 488-labeled SRP19 (25 nM final). Fluorescence emission from the Alexa 488 fluorophore was monitored as SRP19 assembles with the RNA (Varian/Cary Eclipse Spectrofluorometer) and the data was fitted to a pseudo first order equation to obtain the rate of association.

4.3 Results

4.3.1 Ionic strength dependent cooperative RNA binding by SRP68 and SRP72

Under high ionic strength condition (polycationic DE53 resin (*1*) or 2 M KCl (*2*)), SRP68 and SRP72 dissociate from the native SRP as a stable heterodimer. Although the heterodimer functionally reassembled with the SRP RNA, two previous reports reached different conclusions about the RNA binding properties of the individual SRP68 and SRP72 proteins (*3, 4*). Therefore, the *in vitro* RNA binding properties of SRP68 and SRP72 were reexamined using equilibrium filter partitioning experiments (*7*). Recombinant forms of canine SRP68 and SRP72 were overexpressed and purified (Figure 4.1). Previous *in vitro*

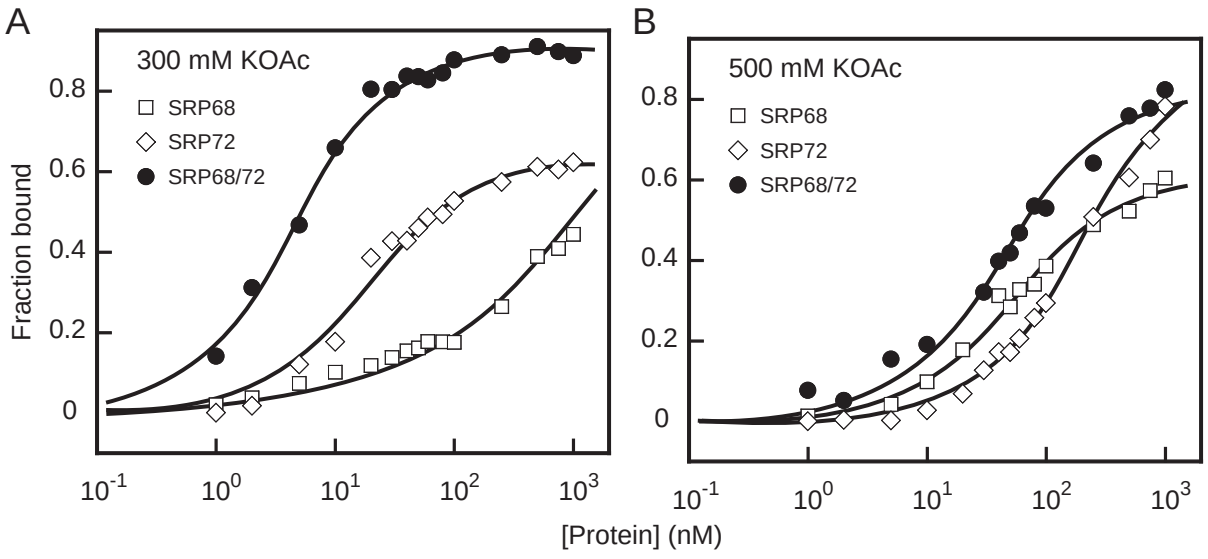

Figure 4.2. RNA binding by SRP68 and SRP72. (A,B) Fraction of bound RNA as a function of SRP protein concentration determined by filter partitioning. Equilibrium dissociation constants (Kd) at 300 mM KOAc SRP68 > 1 µM, SRP72 = 18 nM and SRP68/72 = 4 nM; at 500 mM KOAc SRP68 = 50 nM, SRP72 = 207 nM and SRP68/72 = 43 nM.

experiments with SRP components have been typically performed at either 300 mM (*4*, *9*) or 500 mM (*3*, *6*) potassium acetate (KOAc) concentrations. Here the protein-RNA complexes were studied under both conditions, using the LS RNA (Figure 2.2B). At 300 mM KOAc, SRP68 had a very low affinity for the RNA such that only about 50% of the RNA was bound at SRP68 concentration as high as 1 μM (Figure 4.2A). In contrast, SRP72 bound relatively tightly to the RNA characterized by dissociation constant (K_d) of 18 nM. SRP68 and SRP72 together bound the RNA with an affinity (K_d = 4 nM) that was at least 4-fold higher than that of SRP72 alone (compare SRP68/72 and SRP72 binding experiments in Figure 4.2A).

At the higher 500 mM KOAc concentration, the RNA binding properties of both SRP68 and SRP72 were significantly different from those observed at 300 mM (Figure 4.2B). At 500 mM KOAc, SRP68 bound to the RNA with significantly higher affinity (K_d = 50 nM) than at 300 mM salt. In contrast, SRP72 binding to the LS RNA was significantly weakened (K_d = 200 nM). When both proteins were present, the binding affinity (K_d = 42 nM) was very similar to that measured for SRP68 alone (compare SRP68/72 with SRP68 in Figure 4.2B).

These results indicate that RNA binding properties of both SRP68 and SRP72 are highly dependent on ionic strength of the solution, but in opposite ways; high ionic strength favors RNA binding by SRP68, whereas, low ionic strength favors that by SRP72. Also, at low ionic strength RNA binding by SRP68 and SRP72 is modestly cooperative but the cooperativity disappears with the increase in ionic strength.

4.2.2 SRP19 and SRP68 bind on opposite faces of the SRP RNA

Hydroxyl radical footprinting experiments were performed to identify SRP68 and SRP72 interaction sites on the SRP RNA. The hydroxyl radical reagent reacts with solvent

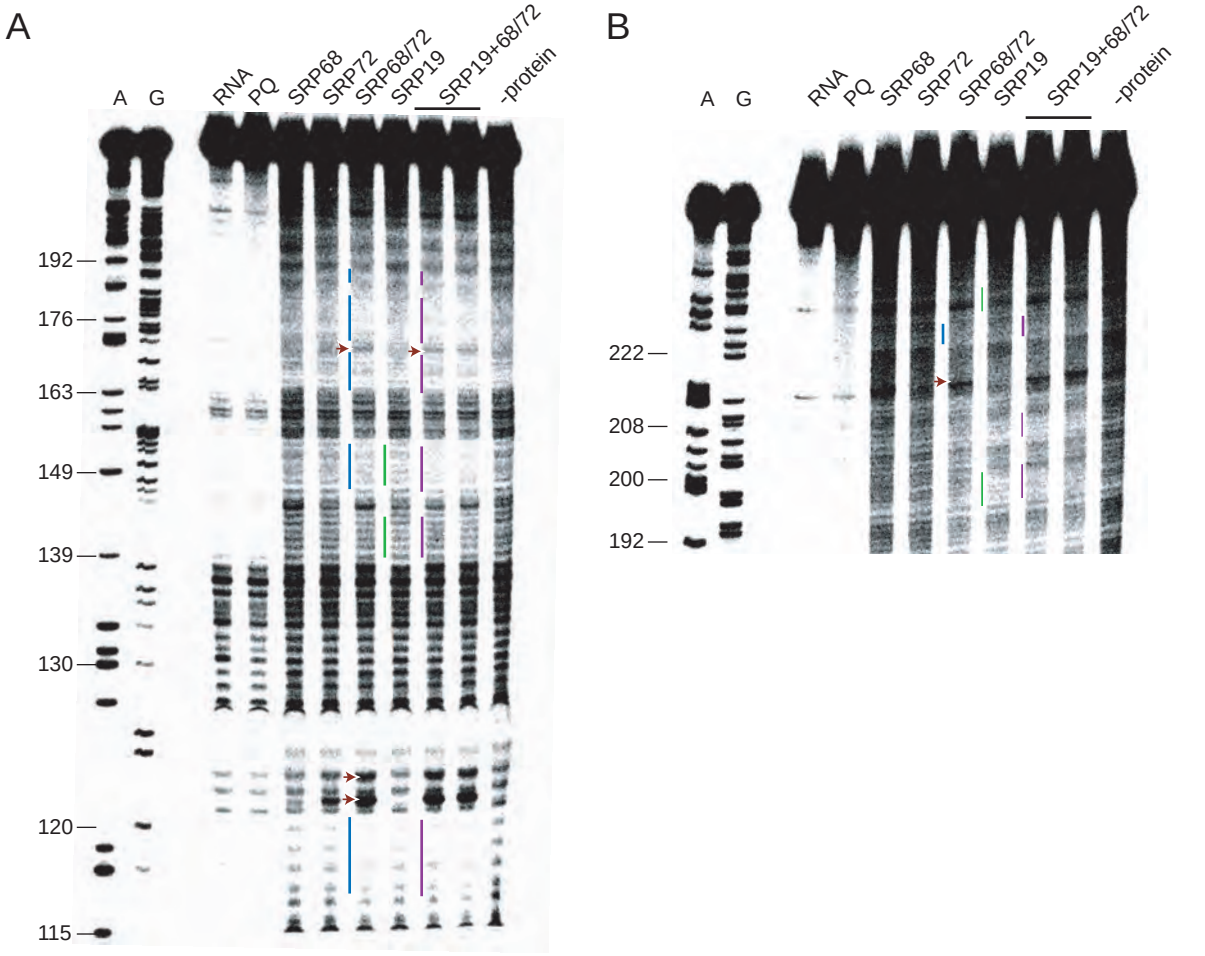

Figure 4.3. SRP68/72 and SRP19 interaction sites on the RNA at 300 mM KOAc. (A,B) Visualization of hydroxyl radical footprinting by denaturing gel electrophoresis. Nucleotides that are specifically protected from hydroxyl radical induced cleavage upon binding by SRP68/72, SRP19 and SRP68/72+SRP19 are emphasized with blue, green and purple lines, respectively. Nucleotides with enhanced reactivity upon SRP68/72 binding are indicated by red arrows.

accessible sites and induces cleavage in the RNA backbone that are not occluded by either RNA-RNA or RNA-protein interactions (*10, 11*).

First, hydroxyl radical footprinting experiments were carried out at the 300 mM KOAc concentration using diagnostic combinations of 100 nM SRP19, SRP68 and SRP72 (Figures 4.3A,B). Footprints specific to any SRP protein were identified by comparing RNA cleavages in the presence of the protein relative to those obtained in the absence of protein. Alone, neither SRP68 nor SRP72 yielded a significant footprint (compare SRP68 and SRP72 lanes with –protein lane in Figures 4.3A,B), even though SRP72, at least, binds with a high affinity to the LS RNA under this condition (Figure 4.2A). However, when both proteins were present together, a large number of nucleotides were protected from hydroxyl radical-mediated cleavage (compare SRP68/72 lane with –protein lane in Figures 4.3A,B; protected nucleotides are illustrated by blue lines). Protected positions are superimposed on the RNA secondary structure for the LS RNA (blue boxes in Figure 4.4). In addition to protected positions, four nucleotides exhibited enhanced reactivity upon SRP68/72 binding (U122, C123, A172 and A213; red arrows in Figures 4.3 and 4.4).

Next, experiments were performed to identify the nucleotides that became protected from hydroxyl radical mediated cleavage upon SRP19 binding. These protected nucleotides reside mainly near the apical loops of helices 6 and 8 in the RNA (green highlights, Figure 4.3 and 4.4). This protection pattern corresponds well with previous footprinting experiments (*7*) and with the high resolution structure of the SRP19-RNA complex (*8*). When footprinting experiments were performed in the presence of both SRP19 and SRP68/72, the protected nucleotides appeared to reflect a simple combination of those for the individual protein components (see SRP19 + SRP68/72 lanes in Figures 4.3A,B).

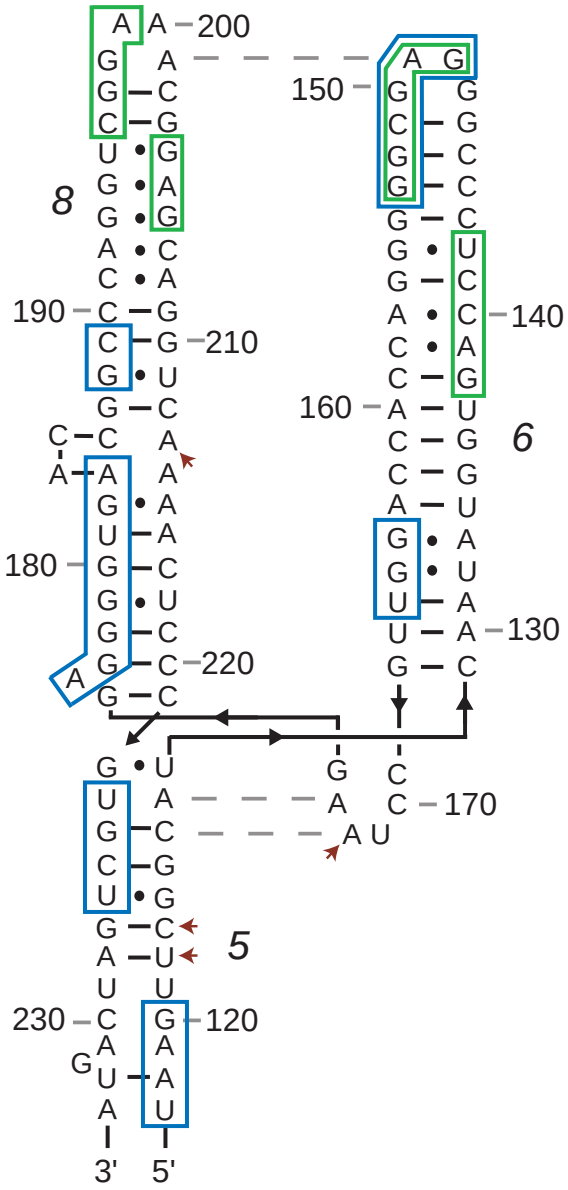

Figure 4.4. Superposition of hydroxyl radical footprints performed at 300 mM KOAc on the LS RNA secondary structure. Nucleotides protected upon binding by SRP68/72 and SRP19 are enclosed in blue and green boxes, respectively; red arrows indicate enhanced cleavages upon SRP68/72 binding.

Subsequently, hydroxyl radical footprinting experiments were performed by Prof. Howard M. Fried to evaluate RNA binding by SRP68 and SRP72 at 500 mM KOAc. At this ionic strength both SRP68 and SRP72 have moderate RNA binding affinity for the LS RNA (Figure 4.2B). Nevertheless, SRP72 alone produced almost no significant footprint on the RNA except at nucleotides 165-168 (Figure 4.5). In contrast, SRP68 alone produced a strong RNA footprint that was very similar to that observed for SRP68/72 at 300 mM KOAc (see SRP68 lane in Figure 4.5, protected nucleotides are illustrated by blue lines). Finally, addition of both proteins yielded a footprint that was almost identical to that produced by SRP68 alone (compare SRP68 and SRP68/72 lanes; Figure 4.5). The nucleotides protected upon SRP68 binding are superimposed on the RNA secondary structure in Figure 4.6.

Two conclusions can be drawn from the results of these hydroxyl radical footprinting experiments. First, neither SRP68 nor SRP72 produced a specific footprint at 300 mM KOAc. In the presence of SRP72, however, SRP68 yielded a specific footprint on the RNA (Figure 4.3A,B), suggesting a cooperativity in RNA binding between these two proteins. Notably, SRP68/72 bound the RNA four-fold more tightly than SRP72 alone (Figure 4.2A). Second, SRP68 interacts with the RNA at the three-way junction in the RNA involving helices 5, 6 and 8. The protected nucleotides were examined in the context of a three-dimensional structure of the RNA (Figure 4.7; SRP68/72 and SRP19 footprints are shown in blue and green, respectively) (*8*). At this region, the center of the protected nucleotide resides on a face of the RNA that is about 180º away from the SRP19 binding face on the RNA. However, RNA positions affected by SRP68/72 binding are quite broad and extended to the tip of helix 6 and the middle of the helix 5 (Figure 4.7).

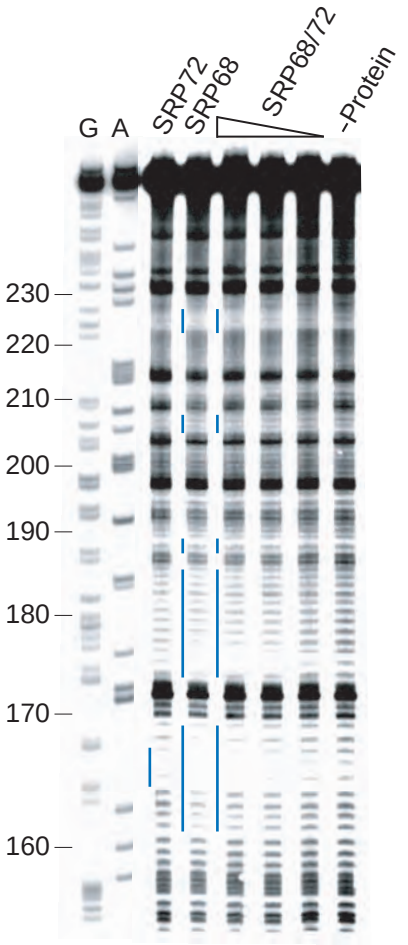

Figure 4.5. SRP68 interaction sites on the RNA at 500 mM KOAc. Nucleotides that are specifically protected from hydroxyl radical induced cleavages upon protein binding are emphasized by blue lines.

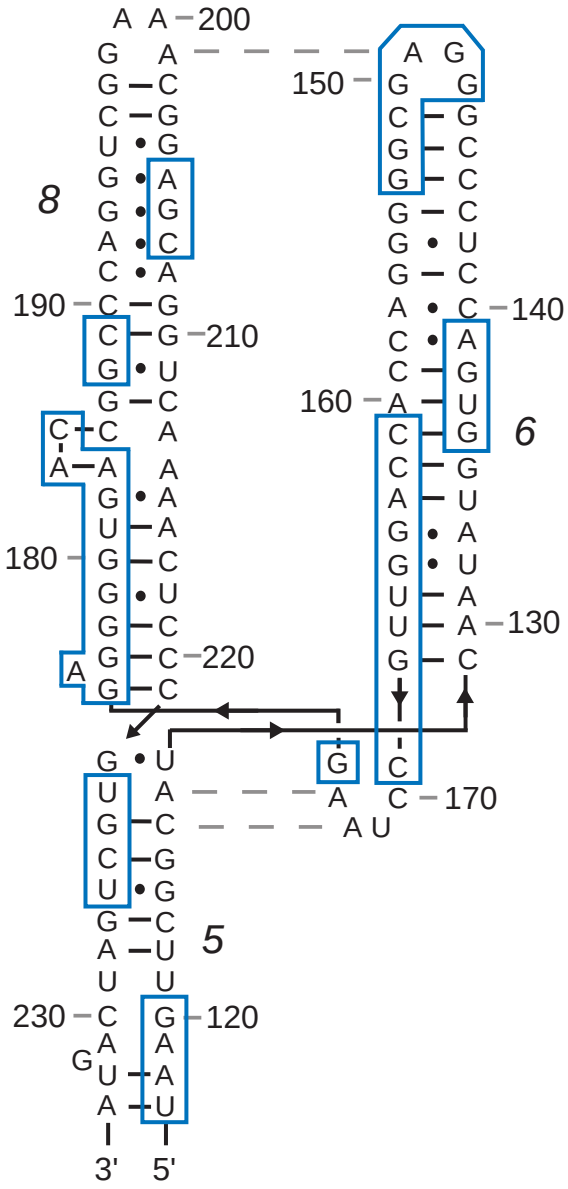

Figure 4.6. Superposition of hydroxyl radical footprints performed at 500 mM KOAc on the LS RNA secondary structure. Nucleotides protected upon binding by SRP68 are enclosed in blue and green boxes.

4.2.3 SRP19 and SRP68/72 bind the RNA anti-cooperatively

Although the primary interaction sites for SRP19 and SRP68/72 appear to lie on opposite faces of the LS RNA, both contact the same two RNA helices and also protect similar structure at the apex of helix 6 (Figures 4.4 and 4.7). Thus, it was sought to assess if SRP19 and SRP68/72 interact cooperatively with the RNA. SRP68/72 binding to the free RNA and to the preformed SRP19-RNA complex at 500 mM KOAc were monitored (Figure 4.8). To measure the mutual effect of SRP19 and SRP68/72 binding to the RNA, the advantage of differential filter retention efficiencies of the two complexes was taken into account. SRP19 binds the RNA with a K_d 2 nM (*7, 12*) and the final complex is characterized by a retention efficiency of ~40% under saturating conditions (*7*). The SRP68/72-RNA complex binds with a lower affinity but is retained by nitrocellulose with near 100% efficiency at saturating concentrations (Figure 4.2B). This difference in nitrocellulose retention efficiency allowed monitoring the effect of prebinding by SRP19 on subsequent RNA-binding by SRP68/72. In this experiment the SRP68/72-RNA complex had a K_d 32 nM. When SRP68/72 was titrated against the preformed SRP19-RNA complex, the dissociation constant increased by three-fold to 97 nM (compare open and solid symbols, Figure 4.8). This three-fold difference was reproducible over many independent experiments.

It was not possible to use filter-binding experiments to compare SRP19 binding to the free RNA and the preassembled SRP68/72-RNA complex because of the very high nitrocellulose retention efficiency of the SRP68/72-RNA complex. Instead, the effect of prior RNA binding by SRP68/72 on SRP19 was monitored in kinetic measurements (Figure 4.9). In this experiment, an environmentally sensitive Alexa 488 fluorophore was tethered at position 72 in SRP19 (as described in Chapter 3). The Alexa 488-tethered SRP19 had a RNA

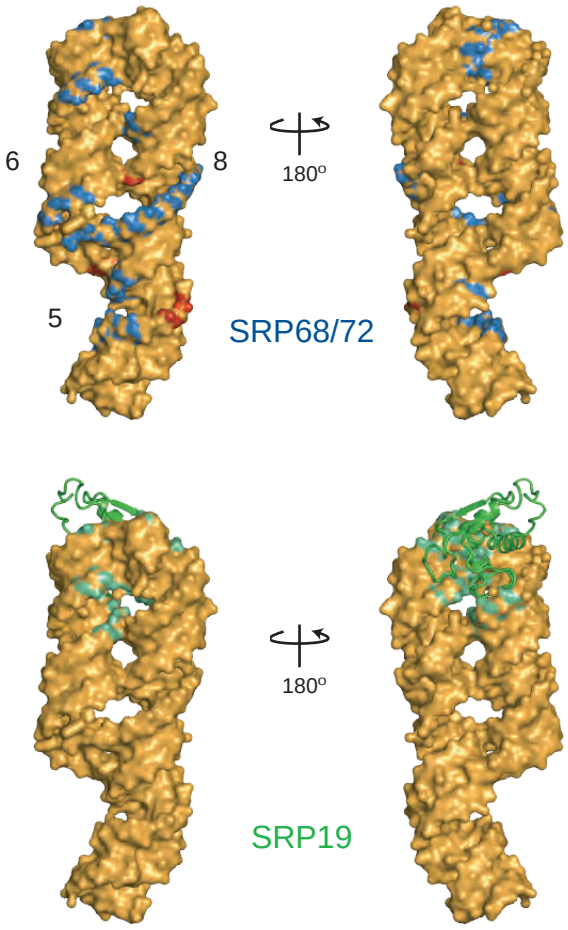

Figure 4.7. Visualization of SRP68/72 and SRP19 interaction sites on a three-dimensional model based on SRP19-RNA crystal structure *(8)*. Nucleotides protected upon SRP68/72 and SRP19 binding are colored in blue and green, respectively. Nucleotides with enhanced reactivities upon SRP68/72 binding are in red.

binding behavior essentially indistinguishable from the native protein. When the Alexa 488-labeled SRP19 binds to the LS RNA, the environment around the tethered fluorophore changes and yields an increase in fluorescence emission. Therefore, the change in fluorescence emission over time during the assembly of SRP19 with the RNA was monitored. SRP19 bound to the free RNA at a rate of 0.7 min^{-1} (closed symbols in Figure 4.9), which corresponds well with the previously reported value of 0.9 min^{-1}, measured at 300 mM salt condition (Figure 3.6). When a similar experiment was performed with the SRP68/72-RNA complex, the SRP19 binding rate decreased by just over three-fold to 0.22 min^{-1} (open symbols in Figure 4.9).

The above results indicate a modest mutually exclusive RNA binding behavior for SRP19 and SRP68/72. Binding by either protein disfavors subsequent RNA binding by the second protein component.

4.4 Discussion

4.4.1 Non-specific binding by SRP72 enhances the affinity of SRP68 for the RNA

In equilibrium filter partitioning experiments it was found that SRP72 has very high affinity for the SRP RNA at low ionic strength, while binding by SRP68 to the RNA is favored by higher ionic strength. (Figures 4.2A,B). However, despite having high affinity at 300 nM KOAc, SRP72 failed to yield any RNA footprint under this condition (Figures 4.3A,B). Together, these results suggest that binding by SRP72 to the RNA is mediated by non-specific electrostatic interactions. Notably, in a previously published RNA-challenge experiment, a C-terminal 14 kDa fragment derived from SRP72 bound to the LS RNA with only about a five-fold higher specificity compared to a completely unrelated RNA (*4*). It is

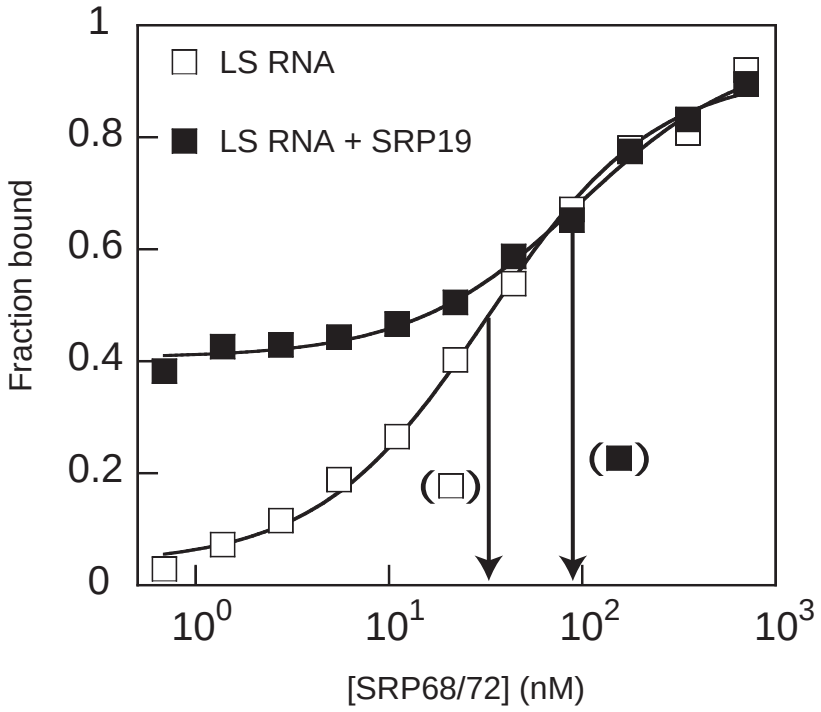

Figure 4.8. Anti-cooperative RNA binding by SRP68/72 and SRP19. RNA binding affinity of SRP68/72 for the free SRP RNA (open squares; K_d = 32 nM) and for the preformed SRP19-RNA complex (solid squares; K_d = 97 nM) as monitored by filter partitioning.

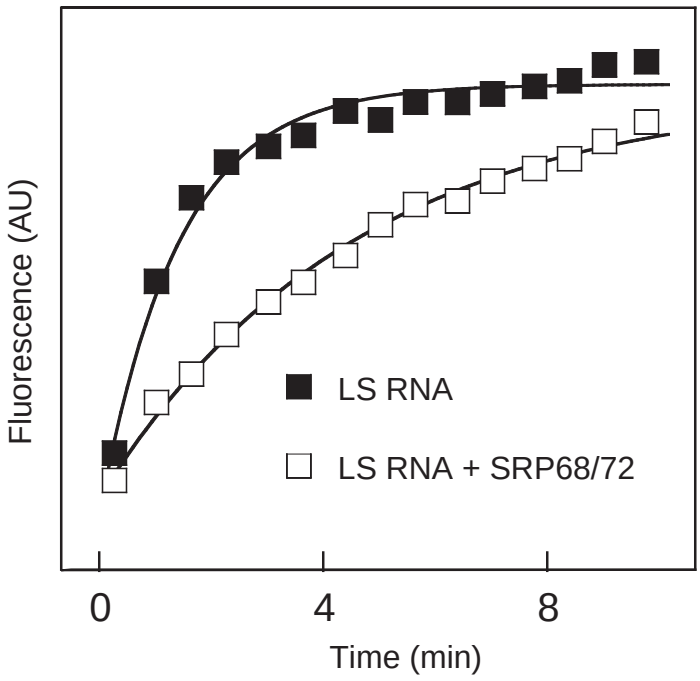

Figure 4.9. Prebinding by SRP68/72 slows down the RNA binding by SRP19. SRP19-RNA assembly kinetics was monitored by change in fluorescence emission efficiency of the environmentally sensitive Alexa 488 fluorophore tethered to position 72 in SRP19. Rates of SRP19 binding to the free RNA (solid squares; k_{on} = 0.7 min^{-1}) and to the preformed SRP68/72-RNA complex (open squares; k_{on} = 0.2 min^{-1}) differ by over three-fold.

thus likely that the 10 lysine residues situated in a 13-amino acid stretch at the C-terminal of SRP72 plays a key role in such electrostatic interaction.

Complying with its low affinity for the RNA at low ionic strength condition, SRP68 fails to yield any footprint under this condition (Figures 4.2A and 4.3A,B). However, in the presence of SRP72, SRP68 yields a very specific footprint on the RNA (Figures 4.3A,B). These results suggest that non-specific binding by SRP72 helps SRP68 interact with the RNA, perhaps via protein-protein interaction. At 300 mM KOAc, SRP68/72 has about a four-fold higher affinity for the RNA than SRP72 alone. This four-fold enhancement in RNA binding affinity comes from the SRP72-induced specific RNA binding by SRP68. Importantly, only a small fraction of non-specifically bound SRP72 would be available to induce specific RNA binding by SRP68. The observed cooperativity, thus, represents only a fraction of the actual cooperativity between these two proteins. At high ionic strength, electrostatic interaction between SRP72 and the RNA weakens, reflecting a higher K_d for SRP72 alone (compare SRP72 bindings in Figures 4.2A,B). Under this condition, no cooperativity is observed between SRP68 and SRP72; SRP68 and SRP68/72 have almost identical affinities for the RNA (Figure 4.2B).

4.4.2 SRP19 and SRP68/72 may structurally communicate via RNA conformational change

The free LS RNA has a flexible structure in which most of the individual base pairs are formed but helices 6 and 8 do not stably associate with each other (*7*). Binding by SRP19 induces a conformational change by bringing helices 6 and 8 closer and aligning them in parallel (*7, 8*). The footprinting results indicate that SRP19 and SRP68 bind to the same two helices in the RNA but on opposite faces (Figures 4.4 and 4.7). SRP19 binds to the apical

loop region of helices 6 and 8, whereas, SRP68 binds at the three-way junction formed by helices 5, 6 and 8 in the RNA. Binding by SRP68 to the RNA also yields a small footprint at the tip of helix 6. This footprint is probably a consequence of a conformational change in the RNA induced by SRP68 binding. Since SRP19 binding yields a similar footprint at this location, one can propose that both SRP68 and SRP19 induce a similar conformational change in the RNA. Thus, despite the fact that SRP68 and SRP19 bind two opposite faces of the RNA and do not directly interact with each other, there exists an indirect way for structural communication between these two proteins via RNA conformational changes.

4.4.3 A structural tension caused by two distinct RNA conformations induced by SRP19 and SRP68/72 binding is the origin of anti-cooperativity

Despite inducing similar conformational changes, SRP19 and SRP68/72 bind anti-cooperatively to the RNA (Figures 4.8 and 4.9). Equilibrium binding affinity of SRP68/72 to the free LS RNA and to the preformed SRP19-RNA complex were studied using filter partitioning at 500 mM KOAc (Figure 4.8). A high ionic strength condition was chosen to minimize the effect of non-specific RNA binding by SRP72. Prebinding by SRP19 reduced the affinity of SRP68/72 for the RNA by about three-fold (Figure 4.8). This effect represents only the lower limit of anti-cooperativity because of the residual non-specific RNA binding by SRP72 at this ionic strength condition. In a complementary experiment it was found that prebinding by SRP68/72 diminishes the rate of RNA binding by SRP19 by more than three-fold (Figure 4.9).

Such mutual anti-cooperative behavior may have two possible origins. First, conformational changes in the RNA induced by SRP68/72 and SRP19 are similar but not identical. In the footprinting experiment, performed at 300 mM KOAc, some nucleotides in

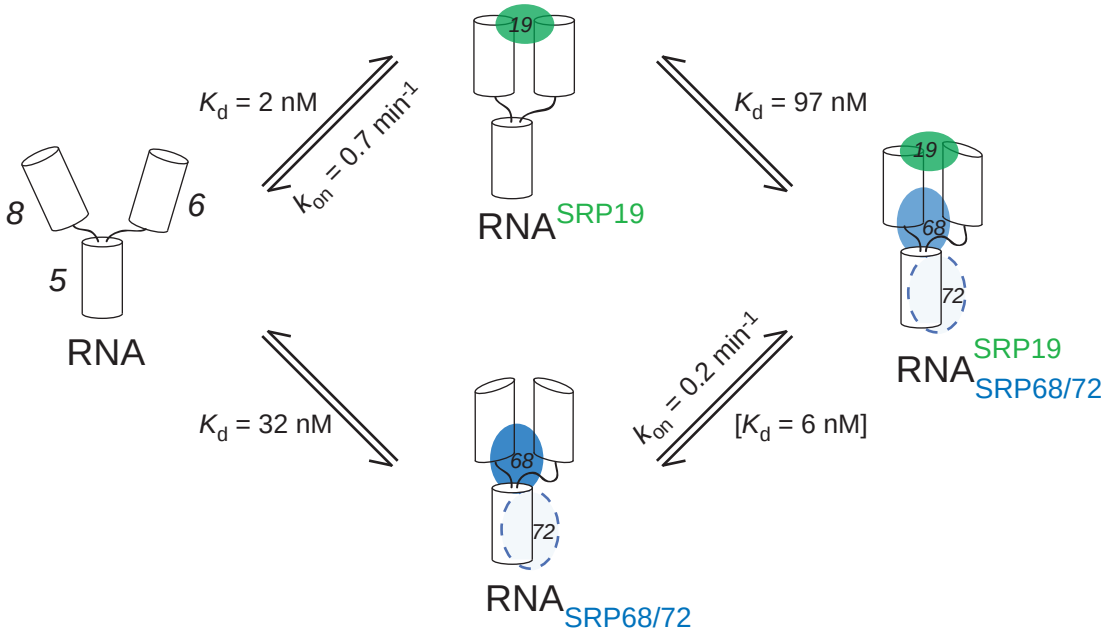

Figure 4.10. Structural tension model for anti-cooperative RNA binding by SRP19 and SRP68/72. Similar but subtly distinct RNA conformations stabilized by these two proteins disfavors the RNA binding by each other. The K_d for the SRP19-RNA complex was obtained from previously published result *(7)*; the dissociation constant for SRP19 from the SRP19-SRP68/72-RNA complex was calculated from other three K_d values.

the RNA yielded enhanced cleavage in the presence of SRP68/72 (Figures 4.4 and 4.7, red arrows/surface indicate hyperactive nucleotides upon SRP68/72 binding). This observation suggests that, upon binding by SRP68/72, the RNA becomes locked in a conformation in which those nucleotides are more solvent exposed. However, such hyperactivity was not observed for SRP19-RNA binary complex, suggesting binding by SRP68/72 and SRP19 induce slightly different RNA conformations. Thus, a small 'structural tension' between two similar but distinct RNA conformations favored by SRP19 and SRP68/72 binding may be the cause of anti-cooperativity. Figure 4.10 illustrates an SRP19-SRP68/72-RNA complex assembly model based on this hypothesis. Another likely origin for anti-cooperativity may lie in the fact that, flexible structures have often been found to promote initial association of two components – the *fly-casting* mechanism (*13*, *14*). Binding by either SRP19 or SRP68/72 reduces the conformational flexibility of the RNA that may disfavor initial interaction with the second protein component. Further experiments are necessary for determining specific contributions of each of these two effects in the mutual anti-cooperative behavior of SRP19 and SRP68/72 during SRP RNA binding.

4.5 References

1. Walter, P., and Blobel, G. (1983) Disassembly and reconstitution of signal recognition particle. *Cell 34*, 525-533.

2. Scoulica, E., Krause, E., Meese, K., and Dobberstein, B. (1987) Disassembly and domain structure of the proteins in the signal-recognition particle. *Eur. J. Biochem 163*, 519-528.

3. Lutcke, H., Prehn, S., Ashford, A. J., Remus, M., Frank, R., and Dobberstein, B. (1993) Assembly of the 68- and 72-kD proteins of signal recognition particle with 7S RNA. *J. Cell Biol. 121*, 977-985.

4. Iakhiaeva, E., Yin, J., and Zwieb, C. (2005) Identification of an RNA-binding domain in human SRP72. *J. Mol. Biol. 345*, 659-666.

5. Halic, M., Becker, T., Pool, M. R., Spahn, C. M. T., Grassucci, R. A., Frank, J., and Beckmann, R. (2004) Structure of the signal recognition particle interacting with the elongation-arrested ribosome. *Nature 427*, 808-814.

6. Siegel, V., and Walter, P. (1988) Binding sites of the 19-kDa and 68/72-kDa signal recognition particle (SRP) proteins on SRP RNA as determined by protein-RNA "footprinting". *Proc. Natl. Acad. Sci. USA 85*, 1801-1805.

7. Rose, M. A., and Weeks, K. M. (2001) Visualizing induced fit in early assembly of the human signal recognition particle. *Nat. Struct. Biol. 8*, 515-520.

8. Oubridge, C., Kuglstatter, A., Jovine, L., and Nagai, K. (2002) Crystal Structure of SRP19 in complex with the S domain of SRP RNA and its implication for the assembly of the signal recognition particle. *Mol. Cell 9*, 1251-1261.

9. Iakhiaeva, E., Bhuiyan, S. H., Yin, J., and Zwieb, C. (2006) Protein SRP68 of human signal recognition particle: Identification of the RNA and SRP72 binding domains. *Protein Sci. 15*, 1290-1302.

10. Latham, J. A., and Cech, T. R. (1989) Defining the inside and outside of a catalytic RNA molecule. *Science 245*, 276-282.

11. Brenowitz, M., Chance, M. R., Dhavan, G., and Takamoto, K. (2002) Probing the structural dynamics of nucleic acids by quantitative time-resolved and equilibrium hydroxyl radical 'footprinting'. *Curr. Opin. Struct. Biol. 12*, 648-653.

12. Henry, K. A., Zwieb, C., and Fried, H. M. (1997) Purification and biochemical characterization of the 19-kDa signal recognition particle RNA-binding protein expressed as a hexahistidine-tagged polypeptide in *Escherichia coli*. *Protein Exp. Pur. 9*, 15026-15033.

13. Shoemaker, B. A., Portman, J. J., and Wolynes, P. G. (2000) Speeding molecular recognition by using the folding funnel: The fly-casting mechanism. *Proc. Natl. Acad. Sci. USA 97*, 8868-8873.

14. Levy, Y., Onuchic, J. N., and Wolynes, P. G. (2007) Fly-casting in protein-DNA binding: Frustration between protein folding and electrostatics facilitates target recognition. *J. Am. Chem. Soc. 129*, 738-739.